

Streamline Upwind Petrov-Galerkin Angular Stabilization of the Linear Boltzmann Transport Equation with Magnetic Fields

by

Amanda Swan

A thesis submitted in partial fulfillment of the requirements for
the degree of

MASTER OF SCIENCE

in

Medical Physics

Department of Oncology

University of Alberta

© Amanda Swan, 2020

Abstract

Dose modelling is an important component of radiotherapy treatment planning, as clinicians prescribe a dose to a tumour while requiring certain adjacent organs to receive at or below a given tolerance dose. Mathematical models such as the linear Boltzmann transport equation, or LBTE, provide a method for calculating the dose received at each location within a patient for a given beam configuration. Solution of this model can be complicated, and deriving accurate and efficient numerical solution methods continues to be an active area of research. Stochastic solutions remain the “gold standard” in terms of accuracy, though many deterministic numerical solvers have been shown to achieve the same level of accuracy as Monte Carlo in a computationally efficient manner.

The development of the combination linear accelerator/magnetic resonance imaging system has created the need for a modified LBTE model that incorporates the Lorentz force and its influence on secondary electrons. Such a model was previously derived mathematically where a new angular advection term was introduced. Finding computationally efficient methods to stabilize the angular advection term so that numerical solutions are both accurate and efficient is a difficult problem. Previously, a numerical method was developed

capable of solving the modified LBTE, however the upwinding scheme used creates a magnetic field dependency in the spectral radius, thus reducing the convergence rate for increasing magnetic field strengths.

In this work, a linear streamline upwind Petrov-Galerkin (SUPG) method is applied in angle as a potential stabilization scheme. A spectral radius analysis shows that application of this method eliminates any magnetic field strength dependency in the convergence rate and the resulting system is unconditionally stable. Simulation results of the discretized system confirm these findings. Phantom simulations also confirm that the SUPG method stabilizes the angular advection term. However, while the method proved accurate in the 0.5 T parallel magnetic field case, advection dominated too strongly in the 1.5 T perpendicular magnetic field and the results were over-diffusive in low density media, negatively impacting the accuracy in these regions. A non-linear SUPG method was then derived and proposed as a possible remedy to the accuracy problems in low density media.

Acknowledgements

This work would not have been possible without the help of many people. First and foremost, I would like to thank my supervisor, Dr. Joel St-Aubin for his guidance and mentorship. He has offered many valuable academic insights that have helped make this project possible.

I would also like to acknowledge the entire Medical Physics department at the Cross Cancer Institute. During my program, the education I received during my courses was excellent, and this knowledge that I gained from all the physicists in the department helped me to complete my project. In particular, a special thanks to members of my supervisory committee, Dr. Gino Fallone and Dr. Brad Warkentin.

Two of the most important acknowledgements go to my fellow graduate students, Ray Yang and Dr. Oleksandr Zelyak. As our projects were greatly intertwined at times, I received a great deal of help both in gaining a more complete understanding of the problem, and in the implementation. I can not thank them enough for the time that they put in to help me complete my project.

A thank you to my funding sources, the Alberta Cancer Foundation, which supported this work in the form of the Antoine Noujaim Graduate Studentship and the William Hebert Young Cancer Research Graduate Studentship.

Finally, thank you to my husband Mark for the continued support and encouragement.

Contents

1	Introduction	1
1.1	Dose	2
1.1.1	Dose Calculation and Treatment Planning	3
1.1.2	Correction-based Methods	4
1.1.3	Model-based Methods	6
1.1.4	Principle-Based Methods	7
1.2	Linac-MR Systems	9
1.2.1	Dose Calculation	9
1.3	Thesis Outline	11
2	Theory	12
2.1	Advection-Diffusion Equations	13
2.1.1	Stabilization	14
2.2	Linear Boltzmann Transport Equation	16
2.2.1	Inclusion of Magnetic Field Term	21
2.3	Discretization of the Variables of the LBTE	22
2.3.1	Energy Discretization	22
2.3.2	Spatial and Angular Discretization	24
2.4	Stationary Iterative Schemes	29
2.4.1	Calculating the Spectral Radius	34
2.5	Stabilized Upwind Method	36

2.5.1	Spectral Radius Results	38
3	Streamline Upwind Petrov Galerkin Method	42
3.1	Background	42
3.1.1	Derivation from Artificial Diffusion	44
3.2	Derivation in Angle for LBTE with Magnetic Fields	46
3.3	Spectral Radius	52
3.3.1	Continuous	53
3.3.2	Discretized	58
3.4	Optimizing the SUPG parameter	59
3.4.1	Empirical Investigation	62
3.4.2	Hyperbolic Cotangent Formula	63
3.5	Simulation Results	66
3.5.1	Calculation Geometry	66
3.5.2	Homogeneous Phantoms	67
3.5.3	Heterogeneous Phantoms	75
4	Non-Linear SUPG Formulation	81
4.1	One-dimension in Space	82
4.2	Application to Angular Advection	84
4.3	Solving the Non-Linear System	89
5	Conclusions and Future Work	91

List of Tables

3.1 Discrete Spectral Radius Results	60
--	----

List of Figures

2.1	Advection-Diffusion Stability	15
2.2	Multigroup Energy Discretization	23
2.3	Spatial and Angular Discretization	25
2.4	Spectral Radius of Upwinding Scheme	41
3.1	Spectral Radius of SUPG Scheme	61
3.2	Determining δ	63
3.3	Determining δ	65
3.4	Simulation Phantoms	67
3.5	Simulation Results: Lung phantom, 0.5 T Parallel Field	69
3.6	Simulation Results: Water phantom, 0.5 T Parallel Field . . .	70
3.7	Simulation Results: Bone phantom, 0.5 T Parallel Field	71
3.8	Simulation Results: Lung phantom, 1.5 T Perpendicular Field	72
3.9	Simulation Results: Water phantom, 1.5 T Perpendicular Field	73
3.10	Simulation Results: Bone phantom, 1.5 T Perpendicular Field	74
3.11	Simulation Results: Water-bone-lung-water phantom, 0.5 T Parallel Field	77
3.12	Simulation Results: Water-bone-air-water phantom, 0.5 T Parallel Field	78
3.13	Simulation Results: Water-bone-lung-water phantom, 1.5 T Perpendicular Field	79

3.14 Simulation Results: Water-bone-air-water phantom, 1.5 T Per- pendicular Field	80
---	----

List of Abbreviations

List of commonly used abbreviations

AAA	A nalytical A nisotropic A lgorithm
BFP	B oltzmann- F okker P lanck
CSD	C ontinuous S lowing D own
CT	C omputed T omography
DGFEM	D iscontinuous G alerkin F inite E lement M ethod
ETAR	E quivalent T issue A ir R atio
FA	F ourier A nalysis
FEM	F inite E lement M ethod
HSF	H ead S catter F actor
ICF	I nhomogeneity C orrection F actor
ICRU	I nternational C ommission on R adiation U nits and M easurements
IMRT	I ntensity- M odulated R adiation T herapy
LBTE	L inear B oltzmann T ransport E quation
linac	L inear A ccelerator
MLC	M ulti- L eam C ollimator
MRI	M agnetic R esonance I maging
PDD	P ercentage D epth D ose
PDE	P artial D ifferential E quation
SUPG	S treamline U pwind P etrov- G alerkin
TAR	T issue A ir R atio
TMR	T issue M aximum R atio
VMAT	V olumetric A rc T herapy

Chapter 1

Introduction

External beam radiotherapy is a crucial step in the modern treatment of cancer, with the accuracy and predictability of radiation dose deposition of critical importance to clinicians. In radiotherapy, the aim is typically to induce cytotoxic effects in cancer cells while causing as little damage as possible to surrounding healthy tissue [1]. The first step in treatment planning is usually simulation, often using computed tomography or CT. This process generates a three-dimensional image of the tumour and surrounding tissues, effectively giving a three dimensional representation of the patient anatomy. Additionally, the CT voxel values can be related to electron density as required for dose calculations. The images are then used to configure radiation beams around a patient in order to achieve a high dose to the tumour and a suitably low dose to the surrounding tissues. While earlier treatments were restricted to simple beam shapes, advances in linear accelerator (linac) technology has allowed for conformal beam delivery using multi-leaf collimators (MLCs). MLCs allow for adaptive, dynamic beam shaping in real-time during treatment. In addition to the ability to treat tumours conformally, advances like intensity-modulated radiation therapy (IMRT) and volumetric arc therapy (VMAT) have led to more precise treatment plans that can better spare healthy tissues and organs

at risk.

The International Commission on Radiation Units and Measurement (ICRU) recommends that dose should be delivered within an accuracy of 5% [2]. A number of components contribute to this possible error, including but not limited to, daily patient setup, target contouring and the dose calculation tools used [2]. Each component contributes to the overall uncertainty, and improvements in each step of the treatment flow can improve overall treatment accuracy. As a result, dose modelling is an important area of research, with the primary goals being accuracy and computational speed. Dose models allow for radiation distributions to be quantified and predicted prior to treatment, so that if a particular dose is prescribed to a tumour along with upper dose limits on surrounding organs and normal tissues, a plan can be designed to meet these criteria. Having an accurate model gives a clinician confidence that a patient will receive the dose as predicted. In addition to the accuracy requirement, such models should be reasonably fast to execute so that treatment planning can be done in minutes.

1.1 Dose

The ability to quantify the dose distribution within a patient is an important component of the treatment flow. Absorbed dose refers to the energy absorbed per unit mass, and has SI units of Gray, or Gy, where $1 \text{ Gy} = 1 \text{ J/kg}$ [3]. This energy is deposited via a number of interactions, each having their own probability of occurrence based on parameters such as material density and particle energy. In this work, the primary focus is on photon irradiations generated from a therapeutic linear accelerator. Photons are indirectly ionizing and do not themselves deposit dose; however, photons that interact with matter generate directly ionizing particles in the form of secondary electrons

and positrons. These secondary charged particles then induce ionizations in the irradiated material as they lose energy and slow down [4]. As charged particles slow down, the energy deposition per unit path length, also called *stopping power*, increases, with most of the energy deposited near the end of the particle's trajectory [3]. Thus to fully model the process of dose deposition, photon flux and the relevant photon-electron interactions that generate the secondary electron flux must both be considered. It is then using this electron flux that absorbed dose may be calculated.

The primary photon-electron interactions of interest are the Compton effect, the photoelectric effect, and pair production. The relative contribution of each process depends on both the atomic number of the irradiated material and the incident energy of the interacting photon [5]. The probability of each interaction is quantified via its macroscopic cross-section, to be discussed further in Chapter 2. The total probability of interaction then is the sum of all individual interaction probabilities. It is through these macroscopic cross-sections that these physical processes can be incorporated into the dose modelling process [6].

1.1.1 Dose Calculation and Treatment Planning

All methods for calculating dose are based on the linear Boltzmann transport equation (LBTE), as they either attempt to solve it directly (such as deterministic methods) or indirectly (such as Monte Carlo techniques). The LBTE is an integrodifferential equation describing radiation transport and its solution corresponds to the radiation probability distribution parametrized by space, angle and energy. This distribution can then be translated to dose through the use of energy deposition cross-sections [6].

Dose calculation algorithms have been in use since the 1950's [7], and use a variety of techniques to solve or approximate the LBTE. The earliest methods

of dose-calculation were correction-based algorithms [8]. From here, the field progressed towards model-based algorithms [1, 3], before the development of the sophisticated principle-based algorithms [6, 9] that are in use today. The development of all of these methods was guided both by an increase in our understanding of radiation physics, and an improvement in computational power [7]. A more complete description of each type of method is given below.

1.1.2 Correction-based Methods

Correction-based techniques assume that a patient is water-equivalent, then use correction factors to obtain a more accurate representation of the dose to the patient. These factors are used by correcting the dose under certain reference conditions for different aspects of the treatment configuration one at a time [1]. For example, the tissue maximum ratio (TMR) may be used to determine the effect of depth in a phantom on the resultant dose, and the head scatter factor (HSF) accounts for scatter from the treatment machine head. An inverse square factor incorporates the effect of distances that differ from the reference distance, and modulation factors account for beam modulators such as wedges or MLCs [3, 10, 11]. The first step in correction-based methods then is the measurement of all relevant factors in a water phantom [8]. Once all reference values have been tabulated, an equivalent water dose can be obtained. It should be noted, however, that some factors do not need to be measured and can be determined through a simple calculation, such as the inverse square factor [1].

The equivalent water dose is then converted to a patient dose value through the use of an inhomogeneity correction factor (ICF) that accounts for the presence of materials of varying densities [8], and is equal to the ratio of the dose in the heterogeneous medium to the dose in water [12]. Obtaining an accurate dose in the presence of inhomogeneities is one of the most challenging

aspects of any dose calculation algorithm. For correction-based methods, a number of techniques for determining the ICF have been developed, beginning in the 1960s [12]. The most direct method is to simply use a ratio of the tissue air ratio (RTAR) values using the actual depth (d) to the calculation point and an adjusted depth (d'). The ICF is then given as the TAR at d' and the given field size, divided by the TAR at depth d and the given field size. The depth d' is computed as the equivalent depth in water equivalent material as determined by the relative electron densities [8, 12].

Other methods for calculating the ICF include the Batho power law, and the equivalent TAR, or ETAR [12]. The Batho power law was developed in the mid 1960s, and consists of raising the TAR values to some power that is determined by the density of inhomogeneities present [13, 14]. This method has been shown to be an improvement over the RTAR method for some cases, however it still only includes local energy deposition and has great limitations in cases of large field sizes or very dense inhomogeneities [12]. The ETAR [15, 16], or equivalent tissue-air ratio method was used widely in the 1980s and is still in limited use today [12]. This method uses full patient CT scans to compute effective values for both the field size and the depth, before again calculating a ratio of TARs.

Correction-based methods are useful in their simplicity, and are still sometimes used clinically as a second-check for treatment-planning software [7, 11]; however, these methods have some significant limitations that necessitated the development of more sophisticated methods of calculation. Correction-based algorithms assume ideal conditions of charged-particle equilibrium, and struggle in the presence of inhomogeneities that do not have a simple slab-like geometry, as correction-based methods do not effectively account for lateral scatter [7, 11]. These techniques will thus have poor accuracy in cases such as build-up regions and tissue interfaces.

1.1.3 Model-based Methods

Model-based methods are based on underlying physical principles, with certain approximations made to speed up calculation time [7]. As the primary photons interact in a medium, they undergo scattering events, generating secondary particles that themselves go on to deposit energy. This whole process can be represented computationally through the use of pre-calculated scatter kernels. The result of this is that non-local energy deposition can be somewhat accounted for, as electron transport is incorporated into these kernels. With correction-based methods, only local energy deposition is accounted for [12, 17]. Thus, model-based methods for dose calculation consider dose deposition as a two-step process: 1) Fluence modelling, and 2) Dose deposition. The primary photon fluence is thus calculated, followed by convolution-superposition with the scattering kernels [7].

To model photon fluence, typically a number of components are computed and summed to obtain the TERMA, or the total energy released to the medium per unit mass due only to primary photon interactions. For example, the TERMA may be divided into contributions direct from the target and from the flattening filter and upper linac components, as well as contributions from the collimators and any physical beam modulator used, such as a wedge [1]. Key to note about these various components is that the energy spectrum will vary, thus necessitating unique deposition kernels for each contributor to the total TERMA [1].

The next step uses scatter kernels to describe the process of spatial energy deposition. These can be computed in one, two and three dimensions, with three dimensional kernels giving the best accuracy but carrying the largest computational cost [12]. These scatter kernels are typically calculated via Monte Carlo simulations, which will be discussed in the next section. Water equivalent material is used for calculation of these distributions and inho-

homogeneous material is incorporated via density scaling [18]. Once both the TERMA and energy deposition kernels have been calculated, the two quantities are convolved to give the resultant dose distribution [12, 18]. Under the proper conditions, these calculations can be done in the Fourier domain to increase computational efficiency. These methods are referred to as fast Fourier transform techniques [18]. Convolution-Superposition methods are widely used in commercial treatment planning systems. For example, Varian’s Analytical Anisotropic Algorithm (AAA) [19] uses this method.

1.1.4 Principle-Based Methods

Principle-based methods are built up from the physics underlying the dose deposition process, which allows for a more accurate representation of inhomogeneities, as the effects are modelled directly. The two main examples of these types of algorithms are deterministic schemes that solve the LBTE directly using sophisticated numerical techniques [9], and Monte Carlo methods that indirectly solve the LBTE by simulating the behaviour of a very large number of particles and computing their aggregate behaviour [20, 21].

Monte Carlo methods are often referred to as the “gold standard” in terms of accuracy of radiotherapy dose calculations, particularly in cases with complex geometries [22, 23]. These Lagrangian calculations are done by simulating the trajectories of a large number of particles, mimicking the transport and energy deposition of the physical particles (i.e., photons or electrons) via their associated known probability distributions. An accurate Monte Carlo simulation begins with the modelling of the treatment unit and phantom geometry, as well as all the associated cross-section data [1]. These can then be used to model the resulting dose distribution.

When all aspects are modelled appropriately, Monte Carlo simulations are very accurate. However, their use is somewhat limited by the computational

burden required to simulate the vast number of particles necessary to obtain the desired reduction in statistical noise [22]. As such, Monte Carlo simulations have traditionally been primarily useful in a research setting as a method of validating other calculation methods [20, 22]. More recently, however, fast Monte Carlo codes have been used clinically in some capacities.

The other main principle-based method is to deterministically solve the LBTE via an Eulerian method [9, 22, 23, 24, 25], which will be the focus of this work. Deterministic methods involve discretization of space, angle and energy, where care must be taken to ensure stability due to the presence of advection. Space is made up of three-dimensions, angle of two-dimensions (polar and azimuthal components), and energy of one-dimension, resulting in a six-dimensional phase space [26]. Spatial discretization can be done via a finite element method (FEM), while angular discretization has traditionally been done via discrete ordinates. Energy discretization typically uses a multigroup method [6, 22, 27]. The result is a large system of equations that is then solved for the unknown fluence values. All of these ideas will be discussed in more detail in Chapter 2. Deterministic methods can be faster to calculate than a full unaccelerated Monte Carlo simulation, and don't suffer from the statistical noise present in the latter.

Existing deterministic methods have been developed and commercialized, and are used in standard linac treatment planning systems. Varian's Acuros XB is a deterministic Boltzmann solver capable of both speed and accuracy, even in inhomogeneous geometries. The accuracy is comparable to Monte Carlo techniques, with improved computational efficiency [28].

1.2 Linac-MR Systems

Tumour localization is one of the most challenging aspects of radiotherapy, as anatomical structures can move between imaging and treatment, or even undergo movement during treatment. These issues necessitate the use of margins that increase the treatment area to ensure the tumour receives the appropriate dose, thus resulting in higher normal tissue dose to the patient. A potential solution mitigating this problem has been developed that combines a standard linear accelerator (linac) with magnetic resonance imaging (MRI) to allow for real-time imaging during treatment [29, 30]. Three main MRI-guided linac designs currently exist, with significant variations in their specifications. The Alberta Linac-MR project at the University of Alberta developed one of the first linac-MR designs, the Aurora-RT, which combines a 0.5T superconducting bi-planar MRI and a 6 MV linac. A key component of this design is that the radiation beam runs parallel to the main magnetic field. This design has been shown to have less of an effect on the resulting dose than a perpendicular configuration [31]. The Australian Magnetic Resonance Imaging-Linac Program has also developed a linac-MR system with a parallel configuration [32]. The first commercial MR linac was developed by ViewRay, and originally featured a 0.35T MRI combined with three cobalt sources [33], and more recently uses a 6MV linac source [34]. The third design, the Elekta Unity MR-linac, combines a 1.5T superconducting MRI and a 7MV linac [35]. Both the ViewRay and the Elekta units feature a configuration in which the radiation beam runs perpendicular to the main magnetic field.

1.2.1 Dose Calculation

Combination linac-MR machines involve delivering a patient's radiation dose while they are immersed in a magnetic field, which has an effect on dose deposi-

tion due to the Lorentz force [24]. While the primary photons are unaffected, secondary charged particles produced via photon interactions experience a deflection which alters their paths. Depending on magnetic field strength and beam/magnetic field orientation, this effect can be clinically significant [36, 37, 38]. Thus, existing deterministic methods for dose calculation must be modified in order to be applied to the case of linac-MR systems. The LBTE is derived based on underlying physical principles of mass conservation. Streaming, scattering and sources are all accounted for, providing an accurate model in most circumstances. However, when radiation is delivered within a magnetic field, an accurate radiation transport model must account for the additional physical phenomenon caused by the Lorentz force. Even in cases of uncharged particle transport, a secondary charged particle flux is induced, as described above, which is then affected by the presence of the magnetic field. Thus, full characterization of radiation transport within a magnetic field must include an angular advection term [23, 24].

Such a model was derived and modelled by St-Aubin et al. [23, 24]. While the original LBTE features only a spatial advection term, the LBTE with magnetic field term includes both spatial and angular advection. It is a well known mathematical result that advection-dominated PDEs are challenging to solve numerically, with stabilization often required [39]. As a result, existing deterministic methods of solving the LBTE are not sufficient for the LBTE with magnetic fields, and additional angular stabilization is required. An existing scheme developed by Yang et al. [40] and St-Aubin et al. [23] will be introduced that provides stabilization in both space and angle, and that has been validated against Monte Carlo for accuracy. While this scheme satisfies both the stabilization and accuracy requirements, there are some factors that limit the attainable computational speed, to be discussed further in Chapter 2.

1.3 Thesis Outline

This thesis focuses on the development of a novel stabilization scheme for the angular advection component of the LBTE with magnetic field term. This investigation begins in Chapter 2 where the relevant background information is provided, beginning with a review of advection-diffusion equations and associated stability issues. The LBTE is then introduced and fully described, including the incorporation of the magnetic field term. The existing framework of Yang et al. [40] is then introduced, along with some of its limitations. In particular, the convergence properties are discussed including the spectral radius results of Zelyak et al. [26].

In Chapter 3, a novel method of angular stabilization is derived for the LBTE with magnetic fields using a streamline upwind Petrov-Galerkin (SUPG) scheme. Following derivation, the convergence behaviour is investigated by using both a continuous and discretized spectral radius calculation. The scheme is then implemented by modifying the existing framework of Yang et al. [40], and simulations are performed using both homogeneous and inhomogeneous phantoms. Accuracy is evaluated by direct comparison to the results obtained using the existing validated framework.

Chapter 4 describes the derivation of a modification of the SUPG method developed in Chapter 3. The scheme described in Chapter 3 is a linear SUPG method, while that derived in Chapter 4 adds a non-linear component. The linear SUPG method of Chapter 3 was found to be over-diffusive in the case of low-density media such as lung or air, and the non-linear SUPG method is derived and presented as a possible solution.

Finally, Chapter 5 concludes by reviewing the key contributions, results and conclusions of the work described throughout the first four chapters.

Chapter 2

Theory

The LBTE is a partial differential equation (PDE) that calculates dose deterministically based on physical principles such as conservation of mass. Both particle streaming (i.e., propagation) and scattering are present to varying degrees dependent on energy and material. In low-density materials, scatter is dominated by particle streaming and the LBTE is an advection-dominated equation. This means that particles travel predominantly with a fixed velocity, due to the relatively low amount of scatter that occurs at such low densities. Advection-dominated PDE's create numerical challenges and must be handled carefully in order to ensure stable and accurate solutions. In this chapter, some background on advection-diffusion equations is given, followed by a description of the LBTE, including the magnetic field term. The finite element implementation of the LBTE with magnetic fields is then given as per the work of Yang et al. [40], followed by a discussion of the limitations and computational constraints associated with using an upwinding method for stabilization.

2.1 Advection-Diffusion Equations

While the LBTE is not explicitly an advection-diffusion equation, the properties are similar. As such, we begin with a brief overview of advection-diffusion equations, as well as associated stability issues that can arise.

Advection-diffusion systems are used in the modelling of many physical phenomena, from heat transfer to concentration gradients, or in this case, radiation transport. A general advection-diffusion equation takes the form

$$\frac{\partial u}{\partial t} + \vec{c} \cdot \nabla u = D\Delta u, \quad (2.1)$$

where u represents the dependent variable, \vec{c} gives the advective velocity, D the diffusion coefficient, and $\Delta = \nabla \cdot \nabla$. The advective term serves to move the entire solution with the given velocity, while the diffusive term spreads and smoothes out the solution.

While the general form of the equation is given above, it is often appropriate to consider the time-independent steady-state case. In these cases, the time-derivative can be set to 0 and the resultant equation is considered in place of Equation 2.1:

$$\vec{c} \cdot \nabla u = D\Delta u. \quad (2.2)$$

The steady-state solution is considered in cases where one is not concerned with the transient behaviour of the solution. For example in the case for the LBTE, the resulting dose distribution or energy fluence is all that is required and transient behaviour of the solution is of little importance for clinical applications.

2.1.1 Stabilization

In cases where the system is highly advection dominated (i.e. where $|\vec{c}|$ is very large relative to D), obtaining a numerical solution is challenging. These types of systems are very susceptible to instabilities if care isn't taken with the solution technique. The following simple example, adapted from Fries and Matthies [39] highlights the instabilities that can arise. Consider a simple one-dimensional, steady-state, advection-diffusion equation:

$$c \frac{\partial u}{\partial x} - D \frac{\partial^2 u}{\partial x^2} = 0. \quad (2.3)$$

A characteristic dimensionless value called the Peclet number quantifies the amount of advection present in a system relative to the amount of diffusion, and is defined by $Pe = \frac{c\Delta x}{2D}$ [39], where Δx gives the grid size. The system is then unstable for $Pe > 1$, and can be stabilized by reducing the advection, increasing the diffusion, or decreasing the grid size [39].

A simple finite difference numerical solver can illustrate the introduction of numerical instabilities with increasing Peclet number. A central difference scheme is first used in both first and second derivatives:

$$\frac{\partial u}{\partial x} \approx \frac{u_{i+1} - u_{i-1}}{2\Delta x}, \quad (2.4)$$

$$\frac{\partial^2 u}{\partial x^2} \approx \frac{u_{i+1} - 2u_i + u_{i-1}}{(\Delta x)^2}. \quad (2.5)$$

The results of simulating Equation 2.3 using the central difference numerical schemes are shown in red in Figure 2.1 for increasing Peclet number, alongside the exact solution in black. Note that for $Pe > 1$, the result is unstable. In this case, the result can be stabilized by using an upwinding numerical

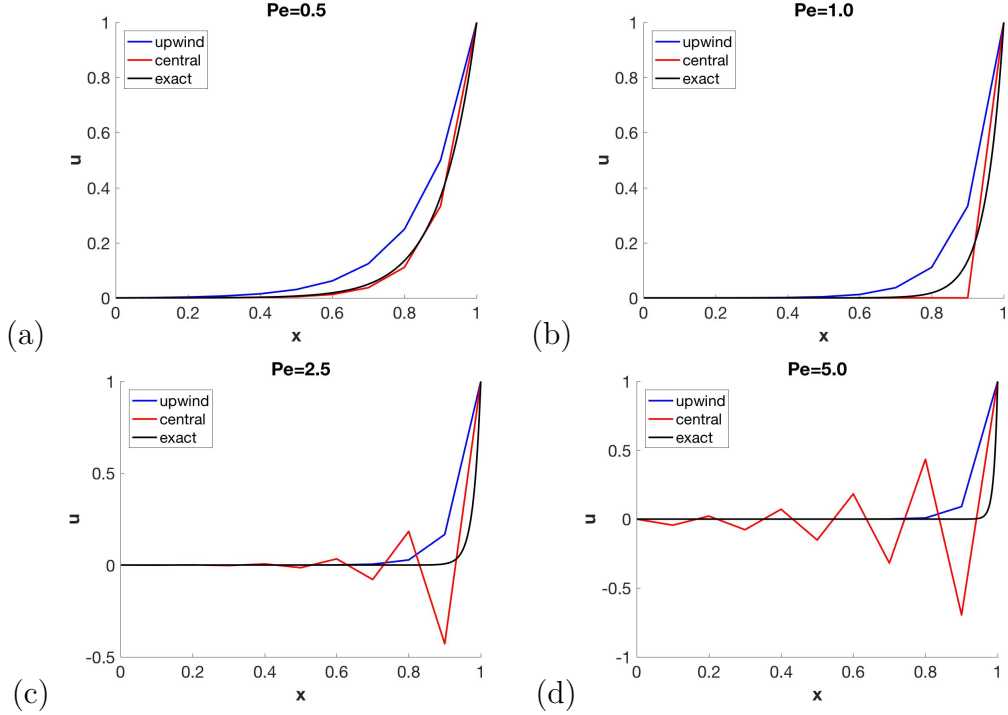


Figure 2.1: The results of simulating Equation 2.3 with a central difference scheme (red), and an upwinding scheme (blue), as well as the exact solution (black), for Peclet numbers of (a) $Pe=0.5$, (b) $Pe=1.0$, (c) $Pe=2.5$ and (d) $Pe=5.0$.

discretization for the advective term, i.e.,

$$\frac{\partial u}{\partial x} \approx \frac{u_i - u_{i-1}}{\Delta x}, \quad (2.6)$$

where c is assumed positive. These results are shown in Figure 2.1 in blue, and it is seen that while the solution is now stable, the accuracy is affected.

The system considered in the remainder of this document will employ a finite element scheme, but the important concept remains the same: advection-dominated systems introduce a high degree of numerical instability and thus stabilization of any advective terms is required. In the case of the LBTE with magnetic fields considered in the following sections, the system is highly advection-dominated in both space and angle, hence stabilization of both terms

is required.

2.2 Linear Boltzmann Transport Equation

As alluded to in the introduction, dose calculation amounts to solving or approximating the solution of the LBTE. The LBTE is an integro-partial differential equation modelling radiation transport in a medium. The full derivation is omitted here, however a brief outline of the framework and equation is provided. For a full derivation, see Lewis and Miller [6].

The LBTE as presented here models angular fluence and arises as a result of particle conservation. In the case where a large enough quantity of particles is present, then statistical uncertainty or fluctuations about the expected fluence value can be ignored. The LBTE deterministically models the expected fluence value, neglecting any perturbations under this assumption. The steady state LBTE is a time-independent equation, as dose-calculation is not concerned with transient behaviour, only steady-state fluence. The angular fluence (ψ) is first parameterized by space (\vec{r}), angle of propagation ($\vec{\Omega} = \vec{v}/v$) and energy E , for a total of six-dimensional phase space. Particle conservation is then considered on a macroscopic scale, with each term in the equation describing a way in which the angular fluence within an infinitesimal volume can change. The terms can be described as follows:

- **Term I:** Spatial streaming: The particles are moving through space with orientation $\vec{\Omega}$. This is modelled through a first order derivative term, and provides the spatial advection term.
- **Term II:** Removal: Particles scatter out of a given energy/angle as they interact with other particles in the medium. This process is described by the total cross-section, σ_T .

- **Term III:** Scattering in: Particles scatter into a given energy/angle from all other energies and angles. This kernel term takes the form of an integration over both energy and angle, and thus depends on the differential cross-section.
- **Term IV:** External source: Particles input into the system from some external source, such as a radioactive source.

The equation is then given by [6]

$$\underbrace{\vec{\Omega} \cdot \nabla \psi(\vec{r}, \vec{\Omega}, E)}_{\text{Term I}} + \underbrace{\sigma_T(\vec{r}, E) \psi(\vec{r}, \vec{\Omega}, E)}_{\text{Term II}} = \underbrace{Q(\vec{r}, \vec{\Omega}, E)}_{\text{Term III}} + \underbrace{S(\vec{r}, \vec{\Omega}, E)}_{\text{Term IV}} \quad (2.7)$$

The explicit form of the scattering term Q is generally written as Q^{xy} , meaning particles of type y created from particles of type x . For example, Q^{pp} would refer to photons generated as a result of photon scattering, while Q^{pe} corresponds to electrons generated as a result of photon scattering. This scattering term takes the form of an integral [24]:

$$Q^{xy} = \int_0^\infty dE' \int d\Omega' \sigma_s^{xy}(\vec{r}, E' \rightarrow E, \Omega \cdot \Omega') \psi_x(\vec{r}, \Omega', E'), \quad (2.8)$$

where σ_s gives the macroscopic differential scattering cross-section [22]. Assuming an isotropic scattering medium, the differential scattering does not depend on the individual angles Ω and Ω' , but only on the angle between them, via $\Omega \cdot \Omega'$. This property can be exploited, and the differential cross-section can be expanded in Legendre polynomials $P_\ell(\Omega \cdot \Omega')$ [6, 22]:

$$\sigma_s(\vec{r}, E' \rightarrow E, \vec{\Omega}' \cdot \vec{\Omega}) = \sum_{\ell=0}^{\infty} (2\ell + 1) \sigma_\ell(\vec{r}, E' \rightarrow E) P_\ell(\Omega' \cdot \Omega) \quad (2.9)$$

$$= \sum_{\ell=0}^{\infty} \sum_{m=-\ell}^{\ell} \sigma_\ell(\vec{r}, E' \rightarrow E) Y_{\ell m}^*(\vec{\Omega}') Y_{\ell m}(\vec{\Omega}), \quad (2.10)$$

where the $Y_{\ell m}$ are the spherical harmonic functions, and $\sigma_\ell(\vec{r}, E' \rightarrow E)$ are the expansion coefficients in the Legendre polynomials, found via [22]

$$\sigma_\ell = \frac{1}{2} \int_{-1}^1 d\mu_0 \sigma_s(\vec{r}, E' \rightarrow E, \mu_0) P_\ell(\mu_0) \quad (2.11)$$

with $\mu_0 = \vec{\Omega}' \cdot \vec{\Omega}$. The following property of Legendre polynomials was used

$$P_\ell = \frac{1}{2\ell + 1} \sum_{m=\ell}^{\ell} Y_{\ell m}^*(\vec{\Omega}') Y_{\ell m}(\vec{\Omega}). \quad (2.12)$$

Note that for practical applications, an upper limit L is imposed such that $0 \leq \ell \leq L$, effectively truncating the spherical harmonic moment expansion order. It is also customary to expand the angular flux from Equation 2.8 over angular flux moments

$$\psi(\vec{r}, \vec{\Omega}', E') = \sum_{\ell'=0}^{\infty} \sum_{m'=-\ell'}^{\ell'} \phi_{\ell' m'}(\vec{r}, E') Y_{\ell' m'}. \quad (2.13)$$

The spherical harmonic moments can be found via

$$\phi_{\ell' m'}(\vec{r}, E') = \int d\Omega' Y_{\ell' m'}(\vec{\Omega}') \psi(\vec{r}, \vec{\Omega}', E'). \quad (2.14)$$

Finally, substituting equations 2.10 and 2.13 into Equation 2.8 gives

$$\begin{aligned} & \int_{0^\infty} dE' \int d\Omega' \sigma_s(\vec{r}, E' \rightarrow E, \vec{\Omega}' \cdot \vec{\Omega}) \psi(\vec{r}, \vec{\Omega}', E') \quad (2.15) \\ &= \sum_{\ell}^{\infty} \sum_{m=-\ell}^{\ell} \int dE' \int d\Omega' \sigma_\ell(\vec{r}, E' \rightarrow E) Y_{\ell m}^* Y_{\ell m}(\vec{\Omega}) \sum_{\ell'=0}^{\infty} \sum_{m'=-\ell'}^{\ell'} \phi_{\ell' m'}(\vec{r}, E') Y_{\ell' m'}(\vec{\Omega}) \\ &= \sum_{\ell=0}^{\infty} \sum_{m=-\ell}^{\ell} \int dE' \sigma_\ell(\vec{r}, E' \rightarrow E) \phi_{\ell m}(\vec{r}, E') Y_{\ell m}(\vec{\Omega}), \end{aligned}$$

where the following property of spherical harmonics was used

$$\int d\Omega' Y_{\ell m}^*(\vec{\Omega}') Y_{\ell' m'}(\vec{\Omega}') = \delta_{\ell\ell'} \delta_{mm'}. \quad (2.16)$$

The LBTE describes the angular flux of a given particle type, for example, photons, electrons or positrons. In this thesis, two simplifying assumptions are made:

- (1): Positrons that are produced do not annihilate and no photons are produced, allowing them to be treated as electrons [24], and
- (2): Photons are not produced as a result of Bremsstrahlung [41].

In the radiotherapy energy range, both of these assumptions should contribute only a very small amount of error and should not reduce the accuracy of the results in a significant way [41]. Additionally, these assumptions greatly simplify the solution method.

When computing angular flux in a radiotherapy situation, it is the electron flux that deposits dose, hence, it is ultimately the electron equation that needs to be solved. However, generally, a radiotherapy source produces photons, and the secondary electrons are generated via photon scattering. As a result, a coupled system is required to fully characterize the system. Assumption (1) above allows for only two particle types to be considered, and assumption (2) allows for Q^{ep} to be neglected, or, the photons that would be generated via bremsstrahlung. Practically speaking, this means that the photon equation can be solved first, followed by the electron equation, without having to iteratively solve both equations simultaneously.

The above representation of the LBTE is valid for photons, however for electrons, the Boltzmann-Fokker-Planck equation must be used to account for additional physical properties. The Boltzmann-Fokker Planck equation, or BFP, consists of the original terms of the LBTE, a continuous slowing down

(CSD) term, plus Fokker-Planck terms. The full BFP including all of these terms is given by [22, 42]

$$\begin{aligned} & \vec{\Omega} \cdot \vec{\nabla} \psi(\vec{r}, E, \vec{\Omega}) + \sigma_T(\vec{r}, E) \psi(\vec{r}, E, \vec{\Omega}) \\ & - \frac{\alpha}{2} \left[\frac{\partial}{\partial \mu} (1 - \mu^2) \frac{\partial}{\partial \mu} \psi(\vec{r}, E, \vec{\Omega}) + \frac{1}{1 - \mu^2} \frac{\partial^2 \psi(\vec{r}, E, \vec{\Omega})}{\partial \phi^2} \right] \\ & - \frac{\partial}{\partial E} \left(\beta_r(\vec{r}, E) \psi(\vec{r}, E, \vec{\Omega}) \right) = Q(\vec{r}, E, \vec{\Omega}) + S(\vec{r}, E, \vec{\Omega}), \end{aligned} \quad (2.17)$$

where α is the momentum transfer coefficient, and β_r is the restricted mass stopping power. For ease of notation, let $\mu = \cos \theta$. In the case of external beam photon calculations, it can be reasonably assumed that $\alpha \approx 0$, leaving only the CSD term [22].

Therefore, the coupled system takes the form

$$\vec{\Omega} \cdot \nabla \psi_p + \sigma^p(\vec{r}, E) \psi_p(\vec{r}, \vec{\Omega}, E) = Q^{pp} + S_p, \quad (2.18)$$

$$\vec{\Omega} \cdot \nabla \psi_e + \sigma^e(\vec{r}, E) \psi_e - \frac{\partial}{\partial E} \left(\beta_r(\vec{r}, E) \psi_e(\vec{r}, E, \vec{\Omega}) \right) = Q^{ee} + Q^{pe} + S_e. \quad (2.19)$$

From this point, once the electron fluence is calculated, the dose can then be computed using the energy deposition cross-section $\sigma_{ED}(\vec{r}, E)$ via [42]

$$D(\vec{r}) = \int dE \int d\Omega \frac{\sigma_{ED}(\vec{r}, E)}{\rho} \psi_e(\vec{r}, E, \vec{\Omega}), \quad (2.20)$$

where $D(\vec{r})$ is the deposited dose, and ρ is the density of the material. Calculating the dose in the case of an MRI-guided linac, however, requires a modification to the electron LBTE given in Equation 2.19, which will be described in the following section.

2.2.1 Inclusion of Magnetic Field Term

As mentioned in the introduction, when irradiation occurs within a magnetic field, the physics of dose deposition are impacted. This effect was derived by St-Aubin et al. [23, 24] and incorporated into the original LBTE as shown in Equation 2.7. The resultant equation for a general charged particle is given by

$$\vec{\Omega} \cdot \nabla \psi(\vec{r}, \vec{\Omega}, E) + \underbrace{\frac{q}{|\vec{p}|} \vec{\tau}(\vec{B}, \vec{\Omega}) \cdot \nabla_{\Omega} \psi(\vec{r}, \vec{\Omega}, E)}_{\text{Angular Streaming}} + \sigma_T(\vec{r}, E) \psi(\vec{r}, \vec{\Omega}, E) - \frac{\partial}{\partial E} \left(\beta_r(\vec{r}, E) \psi(\vec{r}, \vec{\Omega}, E) \right) = Q(\vec{r}, \vec{\Omega}, E) + S(\vec{r}, \vec{\Omega}, E), \quad (2.21)$$

where q is the particle charge, \vec{p} is the particle momentum, \vec{B} is the magnetic field vector, and

$$\vec{\tau}(\vec{B}, \vec{\Omega}) = \frac{1}{\sqrt{1 - \cos^2 \theta}} \left[\left(\vec{\Omega} \times (\vec{\Omega} \times \vec{B}) \right)_z \hat{\phi} - \left(\vec{\Omega} \times \vec{B} \right)_z \hat{\theta} \right]. \quad (2.22)$$

Note that θ and ϕ represent the spherical polar and azimuthal angles, respectively. As before, let $\mu = \cos \theta$. Then, the angular gradient is given by

$$\nabla_{\Omega} = \frac{1}{\sqrt{1 - \mu^2}} \frac{\partial}{\partial \phi} \hat{\phi} + \frac{\partial}{\partial \theta} \hat{\theta}. \quad (2.23)$$

For ease of implementation, it is often useful to assume that the magnetic field is in the z -direction only without loss of generality as any problem can be reduced to this orientation through a coordinate transformation [23]. This simplifies the magnetic field term greatly, as the $\left(\vec{\Omega} \times \vec{B} \right)$ term in $\vec{\tau}$ will be orthogonal to the z -direction, hence $\left(\vec{\Omega} \times \vec{B} \right)_z = 0$, and the angular advection term reduces to a partial derivative in ϕ , as opposed to the full angular gradient.

Vacuum boundary conditions are used such that no particles cross the boundary into the domain:

$$\psi = 0, \quad \vec{\Omega} \cdot \vec{n} < 0, \quad (2.24)$$

where \vec{n} is an outward unit normal perpendicular to the boundary of the domain.

2.3 Discretization of the Variables of the LBTE

As with many PDE's, the analytical solution of the LBTE with magnetic fields is not known, hence a solution must be achieved via numerical methods. The existing work of Yang et al. [40] will be discussed here with an alternative angular discretization method derived and discussed in Chapters 3 and 4. In the existing scheme, energy discretization is handled using the multigroup method [6], and both space and angle are discretized using a Discontinuous Galerkin Finite Element Method (DGFEM) [23, 40].

2.3.1 Energy Discretization

While space and angle will be discretized via the finite element method, or FEM, discussed in the next section, energy is handled via the multigroup method. This method involves dividing the energy domain into discrete energy groups, with

$$E_{\min} = E_G < \dots < E_g < E_{g-1} < \dots < E_0 = E_{\max},$$

shown graphically in Figure 2.2 [26, 40].

The LBTE is then solved for each energy group, one at a time, from the highest energy to the lowest energy. This order is chosen due to the downscat-

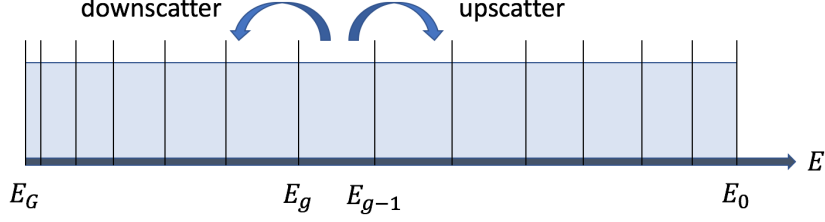


Figure 2.2: A graphical depiction of the energy domain discretization via the multigroup method.

ter of electrons to lower energy groups. For example, we are assuming electrons will not gain energy from scattering interactions, hence electron generation can only occur from higher energy groups to lower energy groups. Assuming functions vary slowly in energy over each bin, energy-dependent parameters can be computed as:

$$\sigma_g(\vec{r}) = \int_{E_{g+1}}^{E_g} dE \frac{\sigma(\vec{r}, E)}{\Delta E_g}, \quad (2.25)$$

$$\sigma_{gg'}(\vec{r}) = \int_{E_{g+1}}^{E_g} dE \frac{\sigma_s(\vec{r}, E' \rightarrow E)}{\Delta E_g}, \quad (2.26)$$

$$S_g(\vec{r}, \vec{\Omega}) = \int_{E_{g+1}}^{E_g} dE S(\vec{r}, \vec{\Omega}, E), \quad (2.27)$$

where ΔE_g is the width of the specific energy group. Additionally, a multi-group magnetic field parameter is defined as [23]

$$\kappa_g = \frac{qc}{E_g - E_{g+1}} \ln \left(\frac{E_g + m_0c^2 + \sqrt{(E_g + m_0c^2)^2 - (m_0c^2)^2}}{E_{g+1} + m_0c^2 + \sqrt{(E_{g+1} + m_0c^2)^2 - (m_0c^2)^2}} \right), \quad (2.28)$$

where c is the speed of light, q is the particle charge, and m_0 is the rest mass of the particle. Then the energy dependence can be eliminated, and replaced

by a discrete index “ g ”:

$$\begin{aligned} \vec{\Omega} \cdot \nabla \psi_g(\vec{r}, \vec{\Omega}) + \sigma_g(\vec{r}) \psi_g(\vec{r}, \vec{\Omega}) + \kappa_g \vec{r}(\vec{B}, \vec{\Omega}) \cdot \nabla_{\Omega} \psi_g(\vec{r}, \vec{\Omega}) \\ = Q_g^{ee}(\vec{r}, \vec{\Omega}) + Q_g^{pe}(\vec{r}, \vec{\Omega}) + S_g(\vec{r}, \vec{\Omega}). \end{aligned} \quad (2.29)$$

Recall that while the electron subscripts have been dropped, Equation 2.29 models electron transport. Additionally, the CSDA term is omitted here as it has been incorporated into the Q^{ee} term via a diamond difference approximation [43]. Similarly, the group indices will be dropped going forward, however it is assumed that the equation represents one energy group. With the multi-group implementation, the scatter source of Equation 2.8 becomes a summation over energy groups, as opposed to a continuous integral:

$$Q_g^{xy} = \int_{\Omega} d\vec{\Omega}' \sum_{g'=1}^g \sigma_s^{xy}(\vec{r}, g' \rightarrow g, \Omega \cdot \vec{\Omega}') \psi_x^{g'}(\vec{r}, \Omega'). \quad (2.30)$$

Note however, that while scattered fluence is generated by higher energy groups in the form of down-scatter, scatter fluence is also generated within a given energy group, i.e., $g \rightarrow g$, in the form of in-scatter. As this term then depends on the angular fluence that is being calculated, the problem must be solved via iteration over ψ_g until convergence is achieved. This will be discussed in Section 2.4.

2.3.2 Spatial and Angular Discretization

In employing the finite element method, or FEM, the PDE can be considered in operator form for ease of notation:

$$\mathcal{L}\psi = g. \quad (2.31)$$

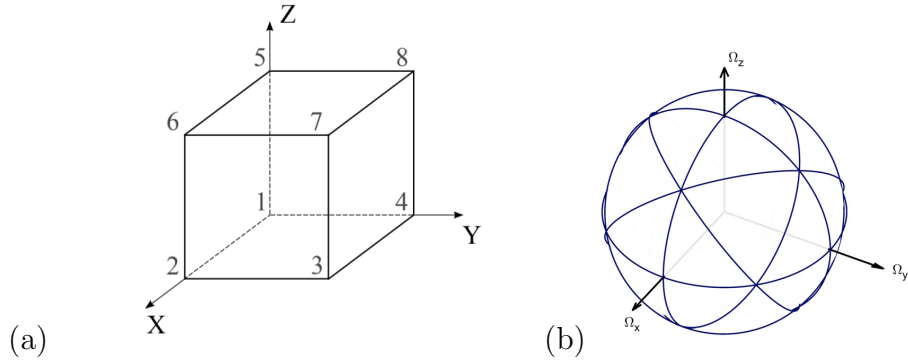


Figure 2.3: (a) A sample spatial element [26], and (b) a sample angular discretization [40].

In comparing this to the modified LBTE given in Equation 2.21

$$\mathcal{L} = \vec{\Omega} \cdot \nabla + \kappa \vec{\tau}(\vec{B}, \vec{\Omega}) \cdot \nabla_{\Omega} + \sigma_T(\vec{r}) \quad (2.32)$$

and

$$g = Q(\vec{r}, \vec{\Omega}) + S(\vec{r}, \vec{\Omega}). \quad (2.33)$$

The idea then is to discretize the system so that an approximation of the unknown function can be found via solution of a linear system. This is done by first discretizing both space and angle into a series of finite elements, each containing a fixed number of “nodes”, or points. For example, space is discretized into cubic voxels, with each voxel containing six faces and eight nodes. An example of such an element is shown on the left of Figure 2.3, and is taken from [26]. The angular elements are chosen to be triangles conformal to the unit sphere, with each element having three, six or ten nodes depending on the basis functions used. A sample discretization of the unit sphere is shown on the right in Figure 2.3, modified from [40].

The next step is to define basis functions on each element, which will control how the solution is interpolated within the elements. In this case, the spatial

basis functions are defined for each node, to be equal to 1 at the node itself, and 0 at every other node. Interpolation between nodes is given by linear functions. Similarly, the angular basis functions are defined as 1 at the node itself, and 0 at every other node. In this case, however, the interpolation is done using higher-order polynomials, such as quadratic or cubic functions.

The unknown function (angular fluence in this case) is then expanded in the set of basis functions defined on the discrete nodes

$$\psi \approx \tilde{\psi} = \sum_{i=1}^I \sum_{p=1}^P \psi_{ip} \lambda_i(\vec{r}) \gamma_p(\vec{\Omega}), \quad (2.34)$$

where $\lambda_i(\vec{r})$ and $\gamma_p(\vec{\Omega})$ are the spatial and angular basis functions. In this case, $I = 8$, and $P = 6$ for quadratic basis functions and $P = 10$ for cubic basis functions, for the number of spatial nodes per element, and angular nodes per element, respectively. It is key to note here then, that the equation will be solved on an element-by-element basis, with the flow between elements controlled via the boundary terms. The values at each spatial node, however, will be discontinuous, thus the value at a given node could differ depending on which element is being solved if it is common to more than one element. This ends up being advantageous as a discontinuous FEM allows for better resolution of the fluence over sharp spatial interfaces in radiation transport problems [40].

The expansion coefficients ψ_{ip} then represent the unknowns in the problem, and as the basis functions are pre-defined, the approximate solution requires solving for these coefficients. This is done by minimizing what is referred to as the residual, given by [44]

$$\tilde{r} = g - \mathcal{L}\tilde{\psi}. \quad (2.35)$$

To solve this, the residual is first multiplied by a weighting function w_i and

integrated over the domain. The result is then set to 0, i.e., [44]

$$\int_V \tilde{r} w_i(x) = 0. \quad (2.36)$$

Such methods in general are referred to as “weighted residual”. The type of weighting function that is used determines the specific numerical method used. In this case, a Galerkin method is chosen, whereby the weighting function is chosen from the same set of basis functions used to expand the unknown function [44]. Then, for the LBTE

$$\int_{V,\Omega} (\mathcal{L}\tilde{\psi} - g) \lambda_j(\vec{r}) \gamma_q(\vec{\Omega}) = 0, \quad (2.37)$$

which can also be written in inner product form as

$$\langle \mathcal{L}\tilde{\psi}, \Upsilon \rangle = \langle g, \Upsilon \rangle, \quad (2.38)$$

with $\Upsilon(\vec{r}, \vec{\Omega}) = \lambda_j(\vec{r}) \gamma_q(\vec{\Omega})$.

The expansion of Equation 2.34 is then substituted into Equation 2.38:

$$\begin{aligned} \langle \mathcal{L}\tilde{\psi}, \Upsilon \rangle = \sum_{i=1}^I \sum_{p=1}^P \psi_{ip} \int_{V,\Omega} d\vec{\Omega} dV \left[\gamma_p \vec{\Omega} \cdot \nabla (\lambda_i) + \lambda_i \kappa \vec{r} \cdot \nabla_{\Omega} (\gamma_p) \right. \\ \left. + \sigma_T (\lambda_i \gamma_p) \right] (\lambda_j(\vec{r}) \gamma_q(\vec{\Omega})), \end{aligned} \quad (2.39)$$

and

$$\langle g, \Upsilon \rangle = \sum_{i=1}^I \sum_{p=1}^P \psi_{ip} \int_{V,\Omega} d\vec{\Omega} dV \left[Q(\vec{r}, \vec{\Omega}, E) + S(\vec{r}, \vec{\Omega}, E) \right] (\lambda_j(\vec{r}) \gamma_q(\vec{\Omega})). \quad (2.40)$$

If i, p are grouped into a hybrid index, as well as j, q , then ψ_{ip} can be interpreted as a vector with the integral terms generating a matrix. Upon solving the known terms of the right hand side, a linear system is generated, and vector ψ_{ip}

can be determined. As this is a discontinuous Galerkin method, the equations are solved on each pair of spatial and angular elements, one at a time, as opposed to the system as a whole. Thus elemental boundary conditions are required. These boundary conditions are defined in space:

$$\Psi_{ipk} = \begin{cases} \psi_{ip}^{\text{inc}}, & \vec{\Omega} \cdot \hat{n}_k < 0 \text{ (down-wind)} \\ \psi_{ip}, & \vec{\Omega} \cdot \hat{n}_k > 0 \text{ (up-wind)}, \end{cases} \quad (2.41)$$

where n_k is the unit normal to boundary surface k of the spatial element. Angular boundary conditions are given by:

$$\Psi_{ipk} = \begin{cases} \psi_{ip}^{\text{inc}}, & \vec{\tau}(\vec{B}, \vec{\Omega}) \cdot \hat{n}_{k'} < 0 \text{ (down-wind)} \\ \psi_{ip}, & \vec{\tau}(\vec{B}, \vec{\Omega}) \cdot \hat{n}_{k'} > 0 \text{ (up-wind)}, \end{cases} \quad (2.42)$$

with

$$\hat{n}_{k'}(\vec{\Omega}) = \frac{\vec{dl} \times \vec{r}}{|\vec{dl} \times \vec{r}|}, \quad (2.43)$$

or the unit normal to boundary edge k' of the angular element. The incoming fluence is given by the adjacent upwind elements based on the respective advective velocities. The outgoing fluence is calculated based on the function defined in the element itself. For elements at the boundary of the domain, the vacuum boundary conditions are used. It should be noted that while for the existing scheme elemental boundary conditions are defined in both space and angle, this will not be the case for the new system derived in Chapter 3. A continuous method will be used to stabilize the angular advection term and thus elemental boundary conditions will only be defined in space.

2.4 Stationary Iterative Schemes

Many mathematical systems, such as the discretized LBTE, can be expressed as linear systems in the form of

$$A\vec{x} = \vec{b}, \quad (2.44)$$

where A is the coefficient matrix, \vec{x} is the unknown vector, and \vec{b} is the known source vector. The unknown vector \vec{x} can then be written in terms of the inverse of the coefficient matrix:

$$\vec{x} = A^{-1}\vec{b}. \quad (2.45)$$

For some forms of A , the system may be solved directly, however for full matrices or very large systems, computer memory capabilities or computational time requirements limit the possibility of direct solutions. Additionally, round-off errors can become significant for large systems [6, 45]. For cases where direct methods are infeasible, iterative solution methods are the preferred approach.

Iterative methods are those which begin with an initial guess x_0 and proceed through a sequence of approximate guesses $x_1, x_2, \dots, x_n, \dots$ which should converge to the exact solution as $n \rightarrow \infty$ [45]. Of course in practice, such sequences must be terminated after some finite number of iterations, thus the rate at which the method converges is of great importance computationally. Any numerical method used to solve the modified LBTE must have a reasonable convergence rate, or the efficiency will be (sometimes drastically) reduced. In the next section, we discuss a method for quantifying the convergence rate.

Spectral Radius

Beginning with

$$A\vec{x} = \vec{b}, \quad (2.46)$$

assume that A is a non-singular matrix, i.e., that $\det(A) \neq 0$. A standard family of iterative solution methods referred to as splitting methods involve “splitting” matrix A by expressing it as the difference of two matrices M and N :

$$A = M - N. \quad (2.47)$$

Note that M and N must be of the same order as the coefficient matrix, and that $\det(M) \neq 0$. Equation 2.46 can then be rewritten as

$$M\vec{x} = N\vec{x} + b. \quad (2.48)$$

The sequence of approximate solution vectors $\{\vec{x}_n\}$, beginning with initial guess \vec{x}_0 , is then generated by the recursive relation

$$M\vec{x}_n = N\vec{x}_{n-1} + b, \quad n = 1, 2, \dots \quad (2.49)$$

As there are infinitely many ways to choose M and N , there are several important considerations in how these matrices are chosen. In a practical sense, splitting methods only make sense if the resulting system is easier to solve than the original linear system, hence matrix M should generate a linear system that is easy to solve. For example, the standard Jacobi method uses a diagonal matrix for M , while the Gauss-Seidel method uses a lower triangular matrix for M [46]. Additionally, not every combination of M and N will generate a convergent scheme, and for those schemes that do converge, their rates of convergence can vary. To investigate the convergence properties, we introduce

the “iteration matrix” T defined as

$$T = M^{-1}N. \quad (2.50)$$

Then, as per Isaacson and Keller [45], the iteration will converge provided the magnitude of all eigenvalues of T are less than one. Equivalently, we may say that the iteration will converge whenever $\rho(T) < 1$, where [42]

$$\rho(T) \equiv \max\{|\lambda| : \lambda \in \sigma(T)\}, \quad (2.51)$$

and $\sigma(T)$ is the eigenvalue spectrum of T , or the set of all eigenvalues of T . $\rho(T)$ is referred to as the *spectral radius* of iteration matrix T . A quick error analysis shows why this condition works. Define the error vector

$$e^{(n)} = x_n - x, \quad n = 0, 1, 2, \dots, \quad (2.52)$$

and subtract Equation 2.48 from Equation 2.49 to get

$$M(x_n - x) = N(x_{n-1} - x), \quad (2.53)$$

$$\implies Me^{(n)} = Ne^{(n-1)}. \quad (2.54)$$

Applying the inverse of M to both sides gives

$$e^{(n)} = \underbrace{M^{-1}N}_T e^{(n-1)} \quad (2.55)$$

$$= Te^{(n-1)} \quad (2.56)$$

$$= T^2 e^{(n-2)} \quad (2.57)$$

$$\vdots \quad (2.58)$$

$$= T^n e^{(0)}, \quad n = 1, 2, \dots \quad (2.59)$$

Now let λ_i and η_i be the set of eigenvalues and eigenvectors for the iteration matrix T , respectively. The set of eigenvectors is linearly independent, hence the error associated with the initial guess x_0 can be expanded as

$$e^{(0)} = \sum_{i=1}^J \alpha_i \eta_i, \quad (2.60)$$

with coefficients α_i . Then consider the error associated with x_1 :

$$e^{(1)} = T e^{(0)} \quad (2.61)$$

$$= T \sum_{i=1}^J \alpha_i \eta_i \quad (2.62)$$

$$= \sum_{i=1}^J \alpha_i \lambda_i \eta_i, \quad (2.63)$$

then using the result from above that $e^{(n)} = T^n e^{(0)}$, by induction,

$$e^{(n)} = T^n e^{(0)} \quad (2.64)$$

$$= \sum_{i=1}^J \alpha_i \lambda_i^n \eta_i, \quad n = 1, 2, \dots \quad (2.65)$$

Therefore in order for $e^{(n)} \rightarrow 0$ as $n \rightarrow \infty$, we require

$$|\lambda_i| < 1, \quad i = 1, 2, \dots, J. \quad (2.66)$$

The spectral radius gives an indication about the rate of convergence as well, as schemes with ρ far less than 1 will converge rapidly. As the spectral radius approaches 1 (while remaining less than 1), the convergence rate of the scheme will be reduced. A scheme having a spectral radius value greater than 1 will not converge, and is referred to as unstable [47].

Source Iteration

With respect to the LBTE with magnetic fields described above, multiple terms depend on the unknown angular fluence which is to be computed. In particular, the left hand side terms of Equation 2.21 clearly depend on the unknown fluence for the energy group under consideration, however, the right-hand side scattering integral also depends on the fluence for the current energy group. While energy groups are solved from highest energy to lowest energy to easily compute down-scatter between energy groups, there will also be in-scatter whereby particles in the current energy group scatter, but do not lose sufficient energy to become part of a lower energy group. Thus, the right hand scatter source term will also depend on the unknown fluence.

Zelyak et al. [26, 42] performed a detailed analysis regarding which terms should be calculated iteratively, and which should be treated as a known source term based on the behaviour of the spectral radius, and thus the convergence properties of the iteration. It was determined that optimal convergence is achieved when the left-hand terms are computed iteratively, while the right-hand scatter term is considered to be a known source. As such, Equation 2.21 is reframed in the form

$$\begin{aligned} \vec{\Omega} \cdot \nabla \psi^{(t+1)}(\vec{r}, \vec{\Omega}, E) + \frac{q}{|\vec{p}|} \vec{\tau}(\vec{B}, \vec{\Omega}) \cdot \nabla_{\Omega} \psi^{(t+1)}(\vec{r}, \vec{\Omega}, E) + \sigma_T(\vec{r}, E) \psi^{(t+1)}(\vec{r}, \vec{\Omega}, E) \\ - \frac{\partial}{\partial E} \left(\beta_r(\vec{r}, E) \psi^{(t+1)}(\vec{r}, \vec{\Omega}, E) \right) \\ = \sum_{\ell=0}^{\ell_{\max}} \sum_{m=-\ell}^{\ell} \int dE' \sigma_{\ell}(\vec{r}, E' \rightarrow E) \phi_{\ell m}^{(t)}(\vec{r}, E') Y_{\ell m}(\vec{\Omega}) + S(\vec{r}, E, \vec{\Omega}), \quad (2.67) \end{aligned}$$

where $\psi^{(t+1)}$ is the unknown angular fluence, and $\phi_{\ell m}^{(t)}$ is the known angular fluence moment from the previous iteration. Typically $\phi_{\ell m}^{(0)}$ is chosen to be 0. The iteration is then carried out until the relative error goes below a specified

threshold value ϵ , defined as

$$\epsilon = \frac{\|\phi^{(t+1)} - \phi^{(t)}\|}{\|\phi^{(t+1)}\|}. \quad (2.68)$$

2.4.1 Calculating the Spectral Radius

The spectral radius of a given scheme can be approximated discretely from the simulation code, or it can be evaluated using the Fourier analysis method. Both methods are briefly outlined here, and will be employed in Chapter 3 for the evaluation of the spectral radius of the proposed stabilization scheme.

Approximation of the Spectral Radius

While one may be tempted to calculate the spectrum of the constructed iteration matrix in order to determine the spectral radius, sometimes these systems are prohibitively large such that direct calculation is not computationally feasible. In such cases, the spectral radius can be estimated through the use of the iterative error $e^{(n)}$ as defined by Equation 2.52 above. Assuming linear convergence, the spectral radius can then be computed via [26, 47]

$$\rho = \lim_{t \rightarrow \infty} \frac{\|\psi - \psi^{(t)}\|}{\|\psi - \psi^{(t-1)}\|}. \quad (2.69)$$

This formula requires that the solution ψ be known, which is not typically the case. As $t \rightarrow \infty$, an alternative formula for the spectral radius is given by

$$\rho = \lim_{t \rightarrow \infty} \frac{\|\psi^{(t)} - \psi^{(t-1)}\|}{\|\psi^{(t-1)} - \psi^{(t-2)}\|}. \quad (2.70)$$

In practice, the iteration can be truncated after sufficient time steps such that the spectral radius value has stabilized.

Fourier Analysis Method

While in this case the Fourier Analysis (FA) method will be applied to the continuous case, it is equally applicable to both discrete and continuous systems [26]. The method provides a manner for predicting the spectral radius before performing simulations, and thus also allows for isolation of any sources of instability within an iterative scheme. FA can also be used to determine the dependence of the convergence rate on certain parameters in the problem under consideration. While a brief outline of the method is given here, an application where the steps are followed through for a complete analysis of the newly proposed stabilization scheme in angle will be shown in Chapter 3. For more details of the method, see Zelyak [42], or Larsen and Morel [47].

The FA method begins with the iterative error on the unknown function ψ , given by

$$\delta\psi^{(t)} = \psi(\vec{r}, \vec{\Omega}) - \psi^{(t)}(\vec{r}, \vec{\Omega}), \quad (2.71)$$

where $\psi(\vec{r}, \vec{\Omega})$ is the exact solution, and $\psi^{(t)}(\vec{r}, \vec{\Omega})$ is the value of ψ after the t^{th} iteration. The iterative error is then expanded as a Fourier integral:

$$\delta\psi^{(t)}(\vec{r}) = \int_{-\infty}^{\infty} a^{(t)}(\vec{\lambda}) e^{i\vec{\lambda}\vec{r}} d\vec{\lambda}. \quad (2.72)$$

When the Fourier expansion for the iterative error is substituted into the system under consideration, an expression for the iteration matrix is derived. Eigenvalues of the iteration matrix are then analyzed with respect to the Fourier wave numbers, and the spectral radius behaviour can be determined. This method allows for determination of the dependence of the spectral radius on various parameters in the problem formulation.

2.5 Stabilized Upwind Method

As mentioned in Chapter 1, the SUPG angular stabilization scheme developed and evaluated in this work will be compared to an existing method that has been validated against Monte Carlo simulations. The existing method will be referred to as the upwind method, or DGFEM. The resulting linear system for the DGFEM is based on Equation 2.38, with the left and right hand sides given by Equations 2.39 and 2.40, respectively. The DGFEM method of St-Aubin et al. [23] and Yang et al. [40] is a discontinuous method, and is solved on an element-wise basis versus the entire system as a whole. For each pair of spatial and angular elements, an individual linear system is computed and solved to determine the values of ψ_{ip} on each set of spatial and angular nodes. This means that a given node can have multiple different values depending upon which element in the system is being solved. The DGFEM method is employed in both space and angle, and allows for the fluence across material interfaces to be more effectively resolved versus a continuous method.

If the system is expanded, and each term written out, then as per Yang et

al. [40], the elemental equation is given by

$$\begin{aligned}
& \sum_{i=1}^I \sum_{p=1}^P \sum_{k=1}^K \psi_{ipk} \int_{\Omega_\alpha} d\vec{\Omega} \gamma_p(\vec{\Omega}) \gamma_q(\vec{\Omega}) \vec{\Omega} \cdot \hat{n}_k \int_{S_k^e} dS \lambda_i(\vec{r}) \lambda_j(\vec{r}) \\
& \quad - \sum_{i=1}^I \sum_{p=1}^P \psi_{ip} \int_{\Omega_\alpha} d\vec{\Omega} \gamma_p(\vec{\Omega}) \gamma_q(\vec{\Omega}) \vec{\Omega} \int_{V^e} dV \lambda_i(\vec{r}) \nabla \lambda_j(\vec{r}) \\
& + \kappa \sum_{i=1}^I \sum_{p=1}^P \sum_{k'=1}^{K'} \psi_{ipk'} \int_{\Gamma_{k'}} d\Gamma \gamma_p(\vec{\Omega}) \gamma_q(\vec{\Omega}) \vec{\tau}(\vec{B}, \vec{\Omega}) \cdot \hat{n}_{k'}(\vec{\Omega}) \int_{V^e} dV \lambda_i(\vec{r}) \lambda_j(\vec{r}) \\
& \quad - \kappa \sum_{i=1}^I \sum_{p=1}^P \psi_{ip} \int_{\Omega_\alpha} d\vec{\Omega} \gamma_p(\vec{\Omega}) \vec{\tau}(\vec{B}, \vec{\Omega}) \cdot \nabla_{\Omega} \gamma_q(\vec{\Omega}) \int_{V^e} dV \lambda_i(\vec{r}) \lambda_j(\vec{r}) \\
& \quad + \sum_{i=1}^I \sum_{p=1}^P \psi_{ip} \sigma(\vec{r}) \int_{\Omega_\alpha} d\vec{\Omega} \gamma_p(\vec{\Omega}) \gamma_q(\vec{\Omega}) \int_{V^e} dV \lambda_i(\vec{r}) \lambda_j(\vec{r}) \\
& = \int_{\Omega_\alpha} d\vec{\Omega} \int_{V^e} dV Q(\vec{r}, \vec{\Omega}) \gamma_q(\vec{\Omega}) \lambda_j(\vec{r}) + \int_{\Omega_\alpha} d\vec{\Omega} \int_{V^e} dV S(\vec{r}, \vec{\Omega}) \gamma_q(\vec{\Omega}) \lambda_j(\vec{r}).
\end{aligned} \tag{2.73}$$

The summation over k indicates summation over each face of the spatial voxel, while the summation over k' gives summation over each edge of the angular element. Integration over the spatial element is indicated by V^e for the volume integral, and by S_k^e for the surface integral. Similarly, integration over the angular element is represented by Ω_α for the surface integral, and by $\Gamma_{k'}$ for the edge integrals. The outward unit normal to side k of the spatial voxel being considered is given by n_k , whereas $\hat{n}_{k'}$ represents the unit normal tangential to the unit sphere along edge k' of the angular element of consideration. The first two terms correspond to the spatial streaming term, the second two terms to the angular advection term, and the last term on the left hand side represents the removal term. The calculation of such terms will be considered in more detail in Chapter 3 in the context of the SUPG method derivation, however it is key to note here that the divergence theorem has been applied to both spatial and angular advection terms, resulting in the introduction of boundary

terms in each case. These boundary terms allow for elements to be coupled together and for the fluence to “flow” through the domain. It is also through these boundary terms that the elemental boundary conditions are defined as in Equations 2.41 and 2.42.

The stabilization for this scheme is provided by a careful treatment of these boundary conditions, coupled with the proper ordering of solution for both spatial and angular elements. As specified in the boundary conditions above, calculated fluence is carried across downwind faces to the upwind faces of the adjacent element, as indicated by the *inc* superscript in the elemental boundary conditions, short for “incoming”. Upwind and downwind directions are determined by the advective velocities in both space and angle. Elements are then solved in an order as determined by the transport direction, beginning at the domain boundary and propagating through the elements sequentially. For more details of how this process is carried out, see Yang et al. [40].

Applying the upwind stabilization method in a DGFEM framework in both space and angle resulted in a scheme that was both stable and very accurate. When simulation results were compared to Monte Carlo simulations for an assortment of slab phantom configurations, a three dimensional gamma analysis resulted in more than 99% of points passing a 2%/2 mm criterion. As this method has been validated for accuracy, our SUPG results will be compared to the upwinding simulation results to evaluate accuracy.

2.5.1 Spectral Radius Results

As described above, a key component of any iterative scheme is the convergence rate, and how it may change with the parameters of the problem. Zelyak et al. [26, 42] investigated the convergence properties of the upwinding DGFEM scheme based on a spectral radius analysis. Parameters such as magnetic field strength, total cross-section, and degree of anisotropy were investigated

to determine what effect, if any, the specified parameters had on convergence rate.

Zelyak et al. [26] first investigated the spectral radius of the iterative procedure described above in the absence of an external magnetic field, setting $\vec{B} = \vec{0}$. The result of this analysis revealed that the spectral radius in this case was always equal to the ratio of the isotropic scattering cross-section $\sigma_0(\vec{r})$ to the total cross section $\sigma(\vec{r})$, regardless of the anisotropy of the problem. Thus, in the case of $\vec{B} = \vec{0}$ [26, 42],

$$\rho = \frac{\sigma_0(\vec{r})}{\sigma(\vec{r})}. \quad (2.74)$$

Note that $\sigma_0(\vec{r})$ is the expansion coefficient of the first scattering moment from Equation 2.10.

The next component of the spectral radius analysis sought to determine the best way to split the matrix of the linear system. With the magnetic field term newly introduced, there are two possibilities for its placement within an iterative scheme. It could be placed:

- (1): As a known source term on the right-hand side of the equation, along with the scattering kernel term, or
- (2): as an operator on the unknown fluence ψ on the left-hand side of the equation.

A spectral radius analysis in this case is useful for determining the stability of the iteration in each case, and thus, the optimal placement of the magnetic field term from a convergence perspective. This effectively determines the matrix splitting discussed above.

Zelyak et al. first considered placement (1) of the magnetic field term as a known source. After performing a Fourier analysis, the key result was that as the magnetic field strength was increased, the spectral radius would increase linearly, exceeding 1 for all values of the magnetic field strength greater than

a threshold value. This result indicates that when the magnetic field term is considered as an iterative source, the iterative scheme is unstable.

As placement **(1)** of the magnetic field term resulted in an unstable scheme, placement **(2)** was then considered. The result of the Fourier analysis was that the magnetic field had no effect on the spectral radius, and thus the spectral radius was given by Equation 2.74 as in the zero magnetic field case. While this result is very encouraging, it does not hold in the discrete case where the upwinding DGFEM scheme described above is implemented.

The first investigation showed that when the magnetic field term is applied as an iterative source, increasing magnetic field strength degrades the convergence rate of the system. The stability of the upwinding DGFEM scheme depends on a coupling between the elements that effectively partitions the magnetic field term, with part of it acting like a left hand side operator and the other part behaving as an iterative source. The iterative source part comes from the elemental boundary conditions whereby some of the solution flux is pulled across the boundary into the adjacent elements, where it becomes a right-hand side source term. While the effect is not so detrimental as when the entire magnetic field term is treated as a source, there is an unfavourable effect on the spectral radius nonetheless. Numerical investigation revealed that for small values of the total cross-section (0.001 cm^{-1}), the spectral radius rapidly approached one as the magnetic field strength was increased and thus while the scheme is still convergent, the convergence rate would be extremely slow. For intermediate values of the cross-section value ($0.1\text{-}1.0 \text{ cm}^{-1}$), the spectral radius increased towards 1 more slowly, resulting in a convergent scheme. For large values of the cross section (1000 cm^{-1}), the spectral radius was not strongly affected by an increase in magnetic field strength. These results of Zelyak et al. are plotted in Figure 2.4 for varying values of the cross-section, and for a fixed ratio of $c = \frac{\sigma_0}{\sigma} = 0.2$. Note that κ and B are taken as one

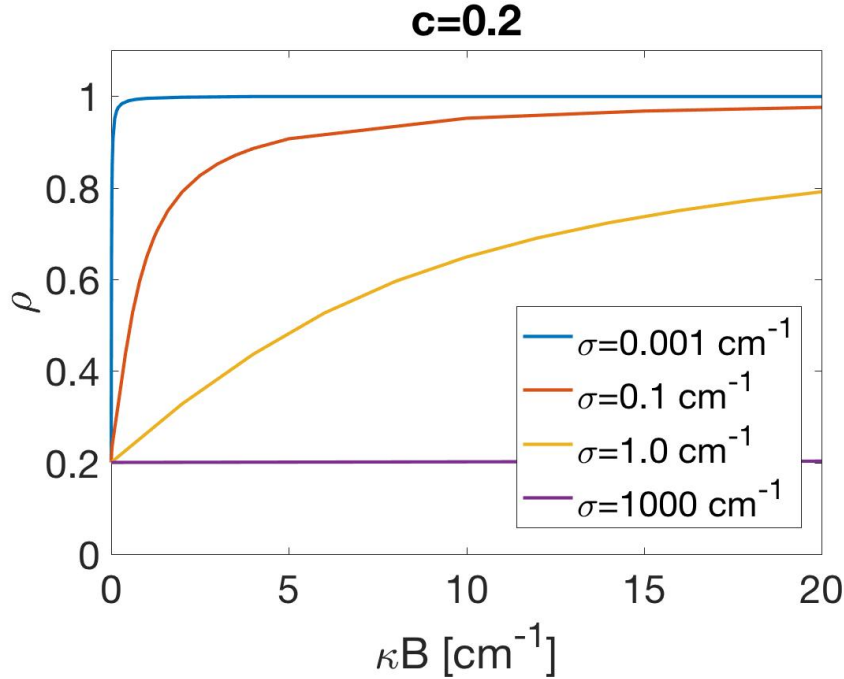


Figure 2.4: The dependence of the spectral radius of the discrete upwinding DGFEM scheme as a function of magnetic field parameter. A constant value of $c = \frac{\sigma_0}{\sigma} = 0.2$ is used, along with cross-section values of $\sigma = 0.001 \text{ cm}^{-1}$ (blue), $\sigma = 0.1 \text{ cm}^{-1}$ (red), $\sigma = 1.0 \text{ cm}^{-1}$ (yellow) and $\sigma = 1000 \text{ cm}^{-1}$ (purple).

parameter, as this is how it appears in the original equation. Together, they are referred to as the “magnetic field parameter”.

The takeaway from these results is that the LBTE with magnetic fields could benefit from an alternative stabilization scheme so that the convergence rate will not be degraded for higher magnetic field strength cases. Such a scheme would require the magnetic field term to remain as a left-hand side operator in the modified LBTE. This idea is the motivation behind the SUPG angular stabilization scheme that will be derived in the next Chapter.

Chapter 3

Streamline Upwind Petrov Galerkin Method

3.1 Background

Yang et al. [40] achieved excellent results in terms of accuracy using their DGFEM technique for solving the modified LBTE with magnetic fields. The results were shown to be very accurate, however there are improvements that could be made in computational speed. In this chapter, we propose and derive a method that attempts to improve the computational speed in two different ways. The Streamline Upwind Petrov-Galerkin, or SUPG, method introduces a small amount of artificial diffusion in the streamline, or advection, direction in order to stabilize the advection term of an advection-diffusion equation. As discussed in Chapter 2, a DGFEM technique will still be used in space to capture discontinuities in material interfaces, but the SUPG method will be applied in angle.

In outlining Yang et al.'s method, the coupling between both spatial and angular elements was a key component of the stabilization scheme, coupled with a selective solution direction. Unfortunately, this limited the potential

for parallelization. Implementing an SUPG scheme in angle will allow all angular elements to be solved simultaneously, as there will be no inter-elemental angular dependence, thus creating much greater potential for parallelization. While parallelization is possible for the Upwinding method, as per Zelyak et al. [26, 42], the spectral radius and thus the convergence rate will be adversely impacted. Additionally, as will be seen later in this chapter, the convergence properties as determined by the spectral radius are more favourable for the SUPG method, and thus it should see faster convergence of the source iteration scheme than is seen in the angular DGFEM method, particularly for stronger magnetic fields.

The SUPG method is applied to the Galerkin FEM via alteration of the weak form. The addition of artificial diffusion is implemented via a modification of the weighting function as defined in Equation 2.36 to include the transport operator. Consider a general transport PDE [48]:

$$\mathcal{L}u = \mathcal{T}u + ku + S_\sigma u = f, \quad (3.1)$$

where S_σ is the scattering operator, and \mathcal{T} is the transport operator in space, defined as [48]

$$\mathcal{T} = \vec{v} \cdot \nabla u(x, \vec{v}). \quad (3.2)$$

Any remaining terms in the equation are contained in the operator k or the function f . Then the weak form using the streamline diffusion method is given by the variational form

$$\langle \mathcal{L}u, w + \delta \mathcal{T}w \rangle = \langle f, w + \delta \mathcal{T}w \rangle, \quad (3.3)$$

where $\langle \rangle$ indicates an inner product, and w a generic weighting function.

3.1.1 Derivation from Artificial Diffusion

To demonstrate this, the general one-dimensional advection-diffusion equation shown above in Equation 2.2 is used, though the result may be applied in general and is not affected by the equation to which it is applied. The derivation shown here is as done in Fries and Matthies [39]. Consider then, the weak form of Equation 2.2, with weighting function $w_j \in V$, and approximate solution \tilde{u} :

$$\int_V dV w_j \left(c \frac{\partial \tilde{u}}{\partial x} - D \frac{\partial^2 \tilde{u}}{\partial x^2} \right) = 0. \quad (3.4)$$

Now artificial diffusion is introduced by directly adding a term $\tilde{D} \frac{\partial^2 \tilde{u}}{\partial x^2}$. The weak form thus becomes

$$\int_V dV w_j \left(c \frac{\partial \tilde{u}}{\partial x} - (D + \tilde{D}) \frac{\partial^2 \tilde{u}}{\partial x^2} \right) = 0. \quad (3.5)$$

Applying the finite element expansion $\tilde{u} = \sum_{i=1}^I w_i u_i$, gives

$$\sum_{i=1}^I u_i \int_V dV c w_j \frac{\partial w_i}{\partial x} - \tilde{D} w_j \frac{\partial^2 w_i}{\partial x^2} - D w_j \frac{\partial^2 w_i}{\partial x^2} = 0. \quad (3.6)$$

Applying integration by parts to both second derivative terms

$$\begin{aligned} \sum_{i=1}^I u_i \left[c \int_V dV w_j \frac{\partial w_i}{\partial x} + \tilde{D} \int_V dV \frac{\partial w_j}{\partial x} \frac{\partial w_i}{\partial x} \right. \\ \left. + D \int_V dV \frac{\partial w_j}{\partial x} \frac{\partial w_i}{\partial x} - D \int_S dS w_j \frac{\partial w_i}{\partial x} \right] = 0, \quad (3.7) \end{aligned}$$

where S denotes the boundary of V . Note that there is no boundary term for the artificial diffusion term defined by \tilde{D} , justified by considering the scheme

only over element interiors [39]. The above can be rearranged in the form

$$\sum_{i=1}^I u_i \left[c \int_V dV \left(w_j + \frac{\tilde{D}}{c} \frac{\partial w_j}{\partial x} \right) \frac{\partial w_i}{\partial x} + D \int_V dV \frac{\partial w_j}{\partial x} \frac{\partial w_i}{\partial x} - D \int_S dS w_j \frac{\partial w_i}{\partial x} \right] = 0. \quad (3.8)$$

From this form, it can be seen that the artificial diffusion can be treated as an additional component to the weighting function on the advection term. However, these methods must be mathematically consistent, thus a different weighting function cannot be applied to the advection and diffusion terms. The modified weighting function taken from the advection term must then be applied to all terms, giving

$$\sum_{i=1}^I u_i \left[c \int_V dV \left(w_j + \frac{\tilde{D}}{c} \frac{\partial w_j}{\partial x} \right) \frac{\partial w_i}{\partial x} + D \int_V dV \frac{\partial}{\partial x} \left(w_j + \frac{\tilde{D}}{c} \frac{\partial w_j}{\partial x} \right) \frac{\partial w_i}{\partial x} \right] - \sum_{i=1}^I u_i \left[D \oint_S dS \left(w_j + \frac{\tilde{D}}{c} \frac{\partial w_j}{\partial x} \right) \frac{\partial w_i}{\partial x} \right] = 0 \quad (3.9)$$

Finally, the modified weak form is found via the reverse application of integration by parts, resulting in

$$\int_V \left(w_j + \frac{\tilde{D}}{c} \frac{\partial w_j}{\partial x} \right) \left(c \frac{\partial \tilde{u}}{\partial x} - D \frac{\partial^2 \tilde{u}}{\partial x^2} \right) dV = 0. \quad (3.10)$$

As can be seen then, the SUPG method can be obtained from the Galerkin FEM by using a modified weighting function that incorporates a perturbation determined by the transport operator.

The amount of artificial diffusion added in this example can be modified by changing \tilde{D} . Analogously, it is important to determine an appropriate value of δ from Equation 3.3, which controls the amount of artificial diffusion that will be added. Roughly speaking, an ideal value for δ is such that enough diffusion

is added to stabilize the system without adding so much that the accuracy is compromised. While the radiation transport equation does not contain diffusion explicitly, the scattering operator behaves in a diffusive manner. Thus, while the Peclet number cannot be calculated explicitly, it remains true that a system containing a high degree of advection without scatter to balance it will be unstable, while a system that has a high degree of scatter may require little to no stabilization. As a result, it is expected that the parameter δ should depend on the total cross-section, which in itself depends on material and energy. A higher cross-section value should require a smaller δ , and vice versa.

3.2 Derivation in Angle for LBTE with Magnetic Fields

Now that the need for stabilization as well as the proposed scheme have been established, it is necessary to determine how it may be applied to the LBTE with magnetic field term. The interesting and challenging thing about this particular integro-PDE is the fact that it contains both spatial and angular advection, both of which require stabilization. While all previous applications of streamline diffusion have been in the spatial variable, in this work, the same method is used for the angular advection term. This means that the transport term in the new weighting function will now have an angular derivative, as in Equation 3.3. The \mathcal{T} operator of this equation will now refer to the angular advection operator. It should be noted that the streamline diffusion method is a continuous Galerkin FEM. Spatially, as mentioned above, a discontinuous approach is more appropriate, as material interfaces can result in sharp changes in the solution that cannot be accurately represented with a continuous method. In angle however, there should not generally be

sharp discontinuities, hence a continuous method such as streamline diffusion is appropriate.

To simplify the derivation, it will be assumed without loss of generality that the magnetic field is in the z -direction, such that the form of the magnetic field operator is simplified. This way, only scalar integrals need be calculated, avoiding the complication of computing integrals of vectors. This is appropriate since any problem can be reduced to one where the magnetic field is oriented in the z direction through a coordinate transformation [23].

The modified LBTE is then given by [24]

$$\vec{\Omega} \cdot \nabla \psi(\vec{r}, \vec{\Omega}) + \kappa B_z \frac{\partial}{\partial \phi} \psi(\vec{r}, \vec{\Omega}) + \sigma_T(\vec{r}) \psi(\vec{r}, \vec{\Omega}) = Q(\vec{r}, \vec{\Omega}) + S(\vec{r}, \vec{\Omega}). \quad (3.11)$$

The magnetic field strength (assumed to be in the z -direction) is B_z . Then, using the notation above,

$$\mathcal{L} = \vec{\Omega} \cdot \nabla + \kappa B_z \frac{\partial}{\partial \phi} + \sigma_T(\vec{r}), \quad (3.12)$$

and

$$\mathcal{T} = \kappa B_z \frac{\partial}{\partial \phi}. \quad (3.13)$$

The weak formulation incorporating the standard streamline diffusion modification is given by

$$\left\langle \mathcal{L}\psi, \Upsilon + \delta \kappa B_z \frac{\partial \Upsilon}{\partial \phi} \right\rangle = \left\langle Q + S, \Upsilon + \delta \kappa B_z \frac{\partial \Upsilon}{\partial \phi} \right\rangle. \quad (3.14)$$

Note that δ is the parameter controlling the amount of artificial diffusion that is introduced. Then the modified weak form may be written as

$$\underbrace{\langle \mathcal{L}\psi, \Upsilon \rangle}_{(I)} + \underbrace{\left\langle \mathcal{L}\psi, \delta \kappa B_z \frac{\partial \Upsilon}{\partial \phi} \right\rangle}_{(II)} = \underbrace{\langle Q + S, \Upsilon \rangle}_{(III)} + \underbrace{\left\langle Q + S, \delta \kappa B_z \frac{\partial \Upsilon}{\partial \phi} \right\rangle}_{(IV)}. \quad (3.15)$$

Note that terms (I) and (III) are as would be found in the standard DGFEM expansion without streamline diffusion, with terms (II) and (IV) requiring novel derivation.

Term (I): The DGFEM expansion of Equation 2.34 is substituted in for $\psi(\vec{r}, \vec{\Omega})$ and each term is considered separately. Taking the first term:

$$\langle \mathcal{L}, \Upsilon \rangle \approx \left\langle \underbrace{\vec{\Omega} \cdot \nabla \left(\sum_{i=1}^I \sum_{p=1}^P \psi_{ip} \lambda_i(\vec{r}) \gamma_p(\vec{\Omega}) \right)}_{\text{(i)}} + \underbrace{\kappa B_z \frac{\partial}{\partial \phi} \left(\sum_{i=1}^I \sum_{p=1}^P \psi_{ip} \lambda_i(\vec{r}) \gamma_p(\vec{\Omega}) \right)}_{\text{(ii)}} \right. \\ \left. + \underbrace{\sigma_T(\vec{r}) \left(\sum_{i=1}^I \sum_{p=1}^P \psi_{ip} \lambda_i(\vec{r}) \gamma_p(\vec{\Omega}) \right)}_{\text{(iii)}}, \lambda_j(\vec{r}) \gamma_q(\vec{\Omega}) \right\rangle. \quad (3.16)$$

This can then be further separated by considering each of the three terms individually. Applying the inner product to term (i) gives

$$\text{(i)} = \sum_{i=1}^I \sum_{p=1}^P \psi_{ip} \int_{\Omega^e} d\vec{\Omega} \gamma_p(\vec{\Omega}) \gamma_q(\vec{\Omega}) \int_{V^e} dV \vec{\Omega} \cdot \nabla(\lambda_i(\vec{r})) \lambda_j(\vec{r}). \quad (3.17)$$

Applying the product rule to the integrand

$$\vec{\Omega} \cdot \nabla(\lambda_i(\vec{r})) \lambda_j(\vec{r}) = \nabla \cdot (\lambda_i(\vec{r}) \lambda_j(\vec{r}) \vec{\Omega}) - \lambda_i(\vec{r}) \vec{\Omega} \cdot \nabla(\lambda_j(\vec{r})). \quad (3.18)$$

Integrating and applying the divergence theorem then gives

$$\text{(i)} = \sum_{i=1}^I \sum_{p=1}^P \psi_{ip} \int_{\Omega^e} d\vec{\Omega} \gamma_p(\vec{\Omega}) \gamma_q(\vec{\Omega}) \left(\int_{S^e} dS \lambda_i(\vec{r}) \lambda_j(\vec{r}) \vec{\Omega} \cdot \hat{n} \right. \\ \left. - \int_{V^e} dV \lambda_i(\vec{r}) \vec{\Omega} \cdot \nabla(\lambda_j(\vec{r})) \right). \quad (3.19)$$

In applying the divergence theorem in space, a boundary term appears. This boundary term will then be split into “upwind” faces and “downwind” faces,

based on the advection direction. The upwind faces will be moved to the right hand side and treated as a known source, while the downwind faces remain on the left hand side as an unknown. The upwind faces then pull their values from the previously solved spatial elements, thus requiring the elements be solved in a specific order dictated by the advection velocity. This is the concept behind the Upwinding method of Yang et al. [40] where it is applied in both space and angle. Here it is applied only in space. It was determined however, that to ensure stability, the divergence theorem must also be applied in angle, however rather than treating the boundary term as in the Upwinding method, it is here assumed to be 0 due to continuity in angle. Thus, applying the divergence theorem to term (ii), and the inner product to both terms (ii) and (iii) gives

$$(ii) = -\kappa B_z \sum_{i=1}^I \sum_{p=1}^P \psi_{ip} \int_{\Omega^e} d\vec{\Omega} \frac{\partial \gamma_q}{\partial \phi}(\vec{\Omega}) \gamma_p(\vec{\Omega}) \int_{V^e} dV \lambda_i(\vec{r}) \lambda_j(\vec{r}), \quad (3.20)$$

and

$$(iii) = \sum_{i=1}^I \sum_{p=1}^P \psi_{ip} \int_{\Omega^e} \gamma_p(\vec{\Omega}) \gamma_q(\vec{\Omega}) d\vec{\Omega} \int_{V^e} \lambda_i(\vec{r}) \lambda_j(\vec{r}) \sigma_T(\vec{r}) dV. \quad (3.21)$$

Term (II): Taking the second term of the DGFEM scheme, which includes

streamline diffusion, gives

$$\begin{aligned}
\left\langle \mathcal{L}\psi, \delta\kappa B_z \frac{\partial \Upsilon}{\partial \phi} \right\rangle = & \left\langle \underbrace{\vec{\Omega} \cdot \nabla \left(\sum_{i=1}^I \sum_{p=1}^P \psi_{ip} \lambda_i(\vec{r}) \gamma_p(\vec{\Omega}) \right)}_{(i)} + \right. \\
& \left. \underbrace{\kappa B_z \frac{\partial}{\partial \phi} \left(\sum_{i=1}^I \sum_{p=1}^P \psi_{ip} \lambda_i(\vec{r}) \gamma_p(\vec{\Omega}) \right)}_{(ii)} \right. \\
& \left. + \underbrace{\sigma_T(\vec{r}) \left(\sum_{i=1}^I \sum_{p=1}^P \psi_{ip} \lambda_i(\vec{r}) \gamma_p(\vec{\Omega}) \right)}_{(iii)}, \delta\kappa B_z \lambda_j(\vec{r}) \frac{\partial \gamma_q(\vec{\Omega})}{\partial \phi} \right\rangle. \quad (3.22)
\end{aligned}$$

Again, the three terms are considered individually. Applying the inner product first to term (i) gives

$$(i) = \delta\kappa B_z \sum_{i=1}^I \sum_{p=1}^P \int_{\Omega^e} d\vec{\Omega} \frac{\partial \gamma_q(\vec{\Omega})}{\partial \phi} \gamma_p(\vec{\Omega}) \int_{V^e} dV \vec{\Omega} \cdot \nabla(\lambda_i(\vec{r})) \lambda_j(\vec{r}). \quad (3.23)$$

As before, the product rule can be applied to the spatial integral, resulting in

$$\vec{\Omega} \cdot \nabla(\lambda_i(\vec{r})) \lambda_j(\vec{r}) = \nabla \cdot (\lambda_i(\vec{r}) \lambda_j(\vec{r}) \vec{\Omega}) - \lambda_i(\vec{r}) \vec{\Omega} \cdot \nabla(\lambda_j(\vec{r})). \quad (3.24)$$

Then, integrating and applying the divergence theorem gives

$$\begin{aligned}
(i) = \delta\kappa B_z \sum_{i=1}^I \sum_{p=1}^P \psi_{ip} \int_{\Omega^e} d\vec{\Omega} \frac{\partial \gamma_q(\vec{\Omega})}{\partial \phi} \gamma_p(\vec{\Omega}) \left(\int_{S^e} dS \lambda_i(\vec{r}) \lambda_j(\vec{r}) \vec{\Omega} \cdot \hat{n} \right. \\
\left. - \int_{V^e} dV \lambda_i(\vec{r}) \vec{\Omega} \cdot \nabla(\lambda_j(\vec{r})) \right). \quad (3.25)
\end{aligned}$$

The product rule is not required for the remaining integrals. Applying the

inner product

$$(ii) = \delta\kappa^2 B_z^2 \sum_{i=1}^I \sum_{p=1}^P \psi_{ip} \int_{\Omega^e} d\vec{\Omega} \frac{\partial \gamma_p(\vec{\Omega})}{\partial \phi} \frac{\partial \gamma_q(\vec{\Omega})}{\partial \phi} \int_{V^e} dV \lambda_i(\vec{r}) \lambda_j(\vec{r}), \quad (3.26)$$

and

$$(iii) = \delta\kappa B_z \sum_{i=1}^I \sum_{p=1}^P \psi_{ip} \int_{\Omega^e} d\vec{\Omega} \frac{\partial \gamma_q(\vec{\Omega})}{\partial \phi} \gamma_p(\vec{\Omega}) \int_{V^e} \sigma_T(\vec{r}) \lambda_i(\vec{r}) \lambda_j(\vec{r}) dV. \quad (3.27)$$

Then the entire DGFEM-SUPG system can be represented as follows

$$\begin{aligned} & \sum_{i=1}^I \sum_{p=1}^P \sum_{k=1}^K \psi_{ipk} \int_{\Omega^e} d\vec{\Omega} \gamma_p(\vec{\Omega}) \gamma_q(\vec{\Omega}) \vec{\Omega} \cdot \hat{n}_k \int_{S_k^e} dS \lambda_i(\vec{r}) \lambda_j(\vec{r}) \\ & \quad - \sum_{i=1}^I \sum_{p=1}^P \psi_{ip} \int_{\Omega^e} d\vec{\Omega} \gamma_p(\vec{\Omega}) \gamma_q(\vec{\Omega}) \int_{V^e} dV \lambda_i(\vec{r}) \vec{\Omega} \cdot \nabla(\lambda_j(\vec{r})) \\ & + \delta\kappa B_z \sum_{i=1}^I \sum_{p=1}^P \sum_{k=1}^K \psi_{ipk} \int_{\Omega^e} d\vec{\Omega} \frac{\partial \gamma_q(\vec{\Omega})}{\partial \phi} \gamma_p(\vec{\Omega}) \vec{\Omega} \cdot \hat{n}_k \int_{S_k^e} dS \lambda_i(\vec{r}) \lambda_j(\vec{r}) \\ & \quad - \delta\kappa B_z \sum_{i=1}^I \sum_{p=1}^P \psi_{ip} \int_{\Omega^e} d\vec{\Omega} \frac{\partial \gamma_q(\vec{\Omega})}{\partial \phi} \gamma_p(\vec{\Omega}) \int_{V^e} dV \lambda_i(\vec{r}) \vec{\Omega} \cdot \nabla(\lambda_j(\vec{r})) \\ & \quad - \kappa B_z \sum_{i=1}^I \sum_{p=1}^P \psi_{ip} \int_{\Omega^e} d\vec{\Omega} \frac{\partial \gamma_q(\vec{\Omega})}{\partial \phi} \gamma_p(\vec{\Omega}) \int_{V^e} dV \lambda_i(\vec{r}) \lambda_j(\vec{r}) \\ & \quad + \delta\kappa^2 B_z^2 \sum_{i=1}^I \sum_{p=1}^P \psi_{ip} \int_{\Omega^e} d\vec{\Omega} \frac{\partial \gamma_p(\vec{\Omega})}{\partial \phi} \frac{\partial \gamma_q(\vec{\Omega})}{\partial \phi} \int_{V^e} dV \lambda_i(\vec{r}) \lambda_j(\vec{r}) \\ & \quad + \sum_{i=1}^I \sum_{p=1}^P \psi_{ip} \sigma_T(\vec{r}) \int_{\Omega^e} d\vec{\Omega} \gamma_p(\vec{\Omega}) \gamma_q(\vec{\Omega}) \int_{V^e} dV \lambda_i(\vec{r}) \lambda_j(\vec{r}) \\ & \quad + \delta\kappa B_z \sum_{i=1}^I \sum_{p=1}^P \psi_{ip} \sigma_T(\vec{r}) \int_{\Omega^e} d\vec{\Omega} \frac{\partial \gamma_q(\vec{\Omega})}{\partial \phi} \gamma_p(\vec{\Omega}) \int_{V^e} dV \lambda_i(\vec{r}) \lambda_j(\vec{r}) \\ & \hspace{15em} = \text{RHS terms.} \quad (3.28) \end{aligned}$$

The right hand side terms are derived subsequently. Notice in Equation 3.28

that all terms that are due to the streamline diffusion term can be distinguished by the presence of the δ parameter, and that setting $\delta = 0$ gives the original DGFEM formulation.

Now, considering the right hand side, terms (III) and (IV) from Equation 3.15 can be expanded. Applying the inner product to each of these terms, gives

$$\begin{aligned} \langle Q + S, \Upsilon \rangle = & \int_{\Omega^e} d\vec{\Omega} \gamma_q(\vec{\Omega}) \int_{V^e} dV Q(\vec{r}, \vec{\Omega}) \lambda_j(\vec{r}) \\ & + \int_{\Omega^e} d\vec{\Omega} \gamma_q(\vec{\Omega}) \int_{V^e} dV S(\vec{r}, \vec{\Omega}) \lambda_j(\vec{r}), \end{aligned} \quad (3.29)$$

and

$$\begin{aligned} \left\langle Q + S, \delta\kappa B_z \frac{\partial \Upsilon}{\partial \phi} \right\rangle = & \delta\kappa B_z \int_{\Omega^e} d\vec{\Omega} \frac{\partial \gamma_q(\vec{\Omega})}{\partial \phi} \int_{V^e} dV Q(\vec{r}, \vec{\Omega}) \lambda_j(\vec{r}) \\ & + \delta\kappa B_z \int_{\Omega^e} d\vec{\Omega} \frac{\partial \gamma_q(\vec{\Omega})}{\partial \phi} \int_{V^e} dV S(\vec{r}, \vec{\Omega}) \lambda_j(\vec{r}). \end{aligned} \quad (3.30)$$

Finally, the boundary conditions are as in Equation 2.41. Note that these are elemental equations, meaning that the system is solved over each pair of spatial and angular elements separately, and thus the boundary condition above applies to the element boundaries. There are no elemental angular boundary conditions as we are now using a continuous method in angle. Vacuum boundary conditions are used at the boundary of the domain.

3.3 Spectral Radius

In Chapter 2, the development of the SUPG angular stabilization scheme was motivated by the spectral radius results from the existing Upwinding method. As was seen in the work of Zelyak et al. [26], the Upwinding stabilization had an impact on the convergence rate of the iterative scheme. It was deter-

mined through a spectral radius analysis that as the magnetic field strength increased, the spectral radius of the discrete Upwinding scheme increases and thus the convergence rate is reduced. Additionally, due to the coupling of the angular elements, parallelization in the solution of the angular elements becomes limited. While Zelyak et al. [26] provided a method for parallelization in angle for the Upwinding scheme, it was shown that once again, the spectral radius would be negatively effected.

The angular SUPG scheme developed above allows for all angular elements to be solved simultaneously thus allowing for easy parallelization. Additionally, since no part of the magnetic field operator appears on the right hand side of the equation as a source, it is expected that the magnetic field should not impact the spectral radius. This hypothesis is investigated both through a Fourier Analysis of the continuous formalism, and through iterative calculation of the spectral radius using the discrete code.

3.3.1 Continuous

The spectral radius for the continuous (non-discretized) form of the streamline diffusion method can be analyzed via the Fourier Analysis method. For details on this method, the reader should consult Zelyak [26], however it is outlined here along with the results. The weak form of the SUPG equation is, as above

$$\left\langle \mathcal{L}\psi - g, \Upsilon + \delta\kappa B \frac{\partial \Upsilon}{\partial \phi} \right\rangle = 0. \quad (3.31)$$

The adjoint operator is given by $A^\dagger = 1 - \delta\kappa B \frac{\partial}{\partial \phi}$, hence the spectral radius equation is

$$A^\dagger \mathcal{L}\Phi = A^\dagger g. \quad (3.32)$$

To get our equation into the proper form, the differential scattering cross-section is first expanded in Legendre polynomials as per the discussion in

Equations 2.10-2.12. For the purposes of this spectral radius analysis, the angular fluence is also expanded using spherical harmonics as it was in Chapter 2, giving

$$\psi(\vec{r}, \vec{\Omega}) = \sum_{\ell=0}^L \sum_{m=-\ell}^{\ell} \phi_{\ell m}(\vec{r}) Y_{\ell m}(\vec{\Omega}),$$

where the expansion coefficients are given by Equation 2.14. Note here the orthogonality condition for spherical harmonics, as it will be used to simplify the form of equations later on in this analysis:

$$\int d\vec{\Omega} Y_{\ell m}(\vec{\Omega}) Y_{\ell' m'}^*(\vec{\Omega}) = \delta_{\ell\ell'} \delta_{mm'}. \quad (3.33)$$

Then, as per Zelyak, [26], the form of the iterative equation considered in this analysis is the transport equation for a single energy group:

$$\left[\vec{\Omega} \cdot \nabla + \kappa B \frac{\partial}{\partial \phi} + \sigma \right] \psi_g^{(t+1)}(\vec{r}, \vec{\Omega}) = \sum_{\ell} \sum_{m=\ell}^{\infty} \sigma_{\ell, gg'} \phi_{\ell m, g}^{(t)}(\vec{r}) Y_{\ell m}(\vec{\Omega}) + s(\vec{r}, \vec{\Omega}). \quad (3.34)$$

As before, without loss of generality we have assumed \vec{B} to be in the positive z -direction to simplify calculations. Note that only the in-group scatter is considered to be an iterative source, with the scatter from all higher-energy groups included in the known source:

$$s_g(\vec{r}, \vec{\Omega}) = \sum_{g' \neq g}^{N_G} \sum_{\ell=0}^{\infty} \sum_{m=-\ell}^{\ell} \sigma_{\ell, gg'} \phi_{\ell m, g'}(\vec{r}) + S_g(\vec{r}, \vec{\Omega}), \quad (3.35)$$

where N_G is the total number of energy groups, and S_g is the external source as before. Because we are assuming no upscatter, only higher energy groups will contribute to the scattering source. The second iterative equation is given by

$$\phi_{\ell m, g}^{(t)}(\vec{r}) = \int d\vec{\Omega} \psi_g^{(t)}(\vec{r}, \vec{\Omega}) Y_{\ell m}^*(\vec{\Omega}). \quad (3.36)$$

While we will perform this analysis for a single energy group, the g subscripts are omitted going forward for ease of notation. Error functions are then formulated as

$$\delta\psi(\vec{r}, \vec{\Omega}) = \psi^{(t+1)}(\vec{r}, \vec{\Omega}) - \psi^{(t)}(\vec{r}, \vec{\Omega}), \quad (3.37)$$

$$\delta\phi_{lm}(\vec{r}) = \phi_{lm}^{(t+1)}(\vec{r}) - \phi_{lm}^{(t)}(\vec{r}). \quad (3.38)$$

Then, the iterative system of equations incorporating the error functions, is given by

$$\begin{aligned} \left(1 - \delta\kappa B \frac{\partial}{\partial\phi}\right) \left[\vec{\Omega} \cdot \nabla + \kappa B \frac{\partial}{\partial\phi} + \sigma\right] \delta\psi^{(t+1)}(\vec{r}, \vec{\Omega}) \\ = \left(1 - \delta\kappa B \frac{\partial}{\partial\phi}\right) \sum_{\ell m} \sigma_{\ell} \delta\phi_{lm}^{(t)}(\vec{r}) Y_{\ell m}(\vec{\Omega}), \end{aligned} \quad (3.39)$$

$$\delta\phi_{lm}^{(t)} = \int_{\Omega} d\vec{\Omega} \delta\psi^{(t)}(\vec{r}, \vec{\Omega}) Y_{lm}^*(\vec{\Omega}). \quad (3.40)$$

Note that the fixed source terms are eliminated as they remain constant between iterations, and are thus simply subtracted. The error functions can then be expanded using Fourier modes. Here the angular fluence is expanded in Fourier modes both in space and angle:

$$\delta\psi^{(t)}(\vec{r}, \vec{\Omega}) = \sum_p \int_{-\infty}^{\infty} d\vec{\lambda} a_p^{(t)}(\vec{\lambda}, \theta) e^{i\vec{\lambda}\vec{r}} e^{ip\varphi}, \quad (3.41)$$

$$\delta\phi_{\ell m}(\vec{r}) = \int_{-\infty}^{\infty} d\vec{\lambda} b_{\ell m}(\vec{\lambda}) e^{i\vec{\lambda}\vec{r}}. \quad (3.42)$$

Substituting the expansions of Equations 3.41 and 3.42 into Equations 3.39

and 3.40 gives

$$\begin{aligned} \sum_{p=-\infty}^{\infty} (1 - \delta\kappa Bp) [i\vec{\Omega} \cdot \vec{\lambda} + i\kappa Bp + \sigma] a_p^{(t+1)}(\vec{\lambda}, \theta) e^{ip\varphi} \\ = \left(1 - \delta\kappa B \frac{\partial}{\partial \phi}\right) \sum_{\ell m} \sigma_{\ell} Y_{\ell m}(\vec{\Omega}) b_{\ell m}^{(t)}(\vec{\lambda}), \end{aligned} \quad (3.43)$$

$$b_{\ell m}^{(t)}(\vec{\lambda}) = \int d\vec{\Omega} Y_{\ell m}^*(\vec{\Omega}) \sum_{m'=-\infty}^{\infty} a_{m'}^{(t)}(\vec{\lambda}, \theta) e^{im'\varphi}. \quad (3.44)$$

The θ and φ variables of $\vec{\Omega}$ can be separated using the expression

$$Y_{\ell m}(\vec{\Omega}) = Y_{\ell m}(\mu, \varphi) = \sqrt{\frac{(2\ell+1)(\ell-m)!}{(\ell+m)!}} P_{\ell m}(\mu) e^{i\varphi m}, \quad (3.45)$$

with $\mu = \cos\theta$. This relation is then substituted into Equation 3.43 and the equation is multiplied by a single Fourier mode $e^{im'\varphi}$ before being integrated over $\int_0^{2\pi} \frac{d\varphi}{2\pi}$. Replacing $\vec{\Omega} \cdot \vec{\lambda}$ by $\lambda\mu$ gives a simplified expression

$$\begin{aligned} (1 - \delta\kappa Bm') [i\lambda\mu + i\kappa Bm' + \sigma] a_{m'}^{(t+1)}(\vec{\lambda}, \theta) \\ = (1 - \delta\kappa Bm') \sum_{\ell' \geq |m'|} \sigma_{\ell'} b_{\ell' m'}^{(t)}(\vec{\lambda}) C_{\ell' m'} P_{\ell' m'}(\mu), \end{aligned} \quad (3.46)$$

where

$$C_{\ell m} = \sqrt{\frac{(2\ell+1)(\ell-m)!}{(\ell+m)!}}. \quad (3.47)$$

Equations 3.44 and 3.46 are used to derive an iterative equation for $b^{(t)}$:

$$\begin{aligned}
& b_{\ell m}^{(t)}(\vec{\lambda}) \\
&= \int_{-1}^1 \frac{d\mu}{2} \int_0^{2\pi} \frac{d\varphi}{2\pi} C_{\ell m} P_{\ell m}(\mu) e^{-im\varphi} \sum_{\ell' m'} \sigma_{\ell'} e^{im'\varphi} \\
&\quad \cdot \frac{(1 - \delta\kappa Bm') C_{\ell' m'} P_{\ell' m'}(\mu)}{(1 - \delta\kappa Bm)[i\lambda\mu + i\kappa Bm + \sigma]} B_{\ell' m'}^{(t-1)}(\vec{\lambda}) \\
&= \sum_{\ell'} \sigma_{\ell'} \int_{-1}^1 \frac{d\mu}{2} \frac{(1 - \delta\kappa Bm) C_{\ell m} P_{\ell m}(\mu) C_{\ell' m} P_{\ell' m}(\mu)}{(1 - \delta\kappa Bm)[i\lambda\mu + i\kappa Bm + \sigma]} b_{\ell' m}^{(t-1)}(\vec{\lambda}) \\
&= \sum_{\ell'} \sigma_{\ell'} \int_{-1}^1 \frac{d\mu}{2} \frac{C_{\ell m} P_{\ell m}(\mu) C_{\ell' m} P_{\ell' m}(\mu)}{i\lambda\mu + i\kappa Bm + \sigma} b_{\ell' m}^{(t-1)}(\vec{\lambda}).
\end{aligned} \tag{3.48}$$

This can be represented in matrix form:

$$b_{\ell m}^{(t)}(\vec{\lambda}) = T_{\ell\ell'} b_{\ell' m}^{(t-1)}(\vec{\lambda}), \tag{3.49}$$

with the matrix components given by

$$T_{\ell\ell'} = \sigma_{\ell'} C_{\ell\ell'}^m \int_{-1}^1 \frac{d\mu}{2} \frac{P_{\ell m}(\mu) P_{\ell' m}(\mu)}{i\lambda\mu + i\kappa Bm + \sigma}, \tag{3.50}$$

with

$$C_{\ell\ell'}^m = \sqrt{\frac{(2\ell + 1)(\ell - m)!}{(\ell + m)!}} \sqrt{\frac{(2\ell' + 1)(\ell' - m)!}{(\ell' + m)!}}. \tag{3.51}$$

The eigenvalues of the iterative matrix T determine the convergence behaviour of the original system. At this point, the key result here is that the SUPG operator, i.e., the term containing δ , completely cancels out, and thus does not have an effect on spectral radius compared to the standard Galerkin formulation. It is noteworthy that the final result of Equation 3.50 is identical to that of Zelyak et al. [26, 42] for the original Galerkin formulation, for which they determined the spectral radius was not affected by the magnetic field strength and that the system was unconditionally stable. Recall that there

was a dependence on the B -field when the DGFEM method was implemented, however, this will not be the case for the SUPG scheme due to the use of a continuous method in angle. This was determined via a numerical investigation which determined that the maximum eigenvalue, and thus the spectral radius value, occurred for $m = 0$, or the isotropic scattering case. Thus the spectral radius in the case of the SUPG angular stabilization scheme is equal to that of the 0 T magnetic field case, and is given by $\rho = \frac{\sigma_0}{\sigma}$. These analytical results will be validated via simulation in the following section.

3.3.2 Discretized

The results of the continuous derivation indicate that there is no dependence of the spectral radius on either the SUPG parameter δ , or the magnetic field strength B . As a result, the expected value of the spectral radius ρ should be as in the case of a 0 T magnetic field, or the ratio of the isotropic scattering moment σ_0 to the total cross-section σ : [26]

$$\rho = c = \frac{\sigma_0}{\sigma}. \quad (3.52)$$

This result is investigated for the discrete case of Equation 3.15 using the following formula

$$\rho = \lim_{t \rightarrow \infty} \frac{||\psi^{t+1} - \psi^t||}{||\psi^t - \psi^{t-1}||}. \quad (3.53)$$

The spectral radius was then investigated for a variety of values of c , B and δ , with the results summarized in Table 3.1. As can be seen, the spectral radius does not depend on the magnetic field strength or the value of δ , which represents the amount of added diffusion. This is an advantage over the Upwinding stabilization scheme, where the spectral radius increases with magnetic field strength [26], and thus slows the convergence. Recall that as per the work of Zelyak et al. [26], we consider κB as a single parameter, as this is how it

appears in the equation as a whole.

The advantage of this property of the spectral radius can be further highlighted by comparing to the results of the Upwinding method. While for the SUPG method, the spectral radius does not depend on the magnetic field strength, the total cross-section, or the SUPG parameter, the spectral radius analysis for the Upwinding method revealed a dependence on both the magnetic field strength and the total cross-section. This is illustrated in Figure 3.1, where the spectral radius is plotted versus magnetic field strength for both the SUPG technique and the Upwinding method, for four different values of σ_t : (i) $\sigma_t=0.001$, top left, (ii) $\sigma_t=0.1$, top right, (iii) $\sigma_t=1.0$, bottom left, and (iv) $\sigma_t=1000$, bottom right. Here it can clearly be seen that while the convergence rate of the Upwinding scheme will be reduced with increasing magnetic field strength, the convergence rate of the SUPG method is unaffected. Additionally, for very low values of the total cross-section, the spectral radius of the Upwinding scheme approaches 1, thus while still stable, the convergence rate may become arbitrarily slow in such cases.

3.4 Optimizing the SUPG parameter

The results of simulating the angular fluence are now presented as compared to the simulation results of the Upwinding scheme under the same conditions. The Upwinding scheme has been fully validated against Monte Carlo results and has shown a high degree of accuracy [40], hence it is used for comparison.

It is first necessary to determine an appropriate value of δ , which controls the amount of artificial diffusion that will be added. Roughly speaking, an ideal value for δ is such that enough diffusion is added to stabilize the system without adding so much that the accuracy is compromised. While the radiation transport equation does not contain diffusion explicitly, the scattering

$c = 0.05$			
	$\delta = 0.05$	$\delta = 0.5$	$\delta = 5$
$\kappa B = 1$	0.05	0.05	0.05
$\kappa B = 5$	0.05	0.05	0.05
$\kappa B = 10$	0.05	0.05	0.05
$\kappa B = 20$	0.05	0.05	0.05
$c = 0.1$			
	$\delta = 0.05$	$\delta = 0.5$	$\delta = 5$
$\kappa B = 1$	0.1	0.1	0.1
$\kappa B = 5$	0.1	0.1	0.1
$\kappa B = 10$	0.1	0.1	0.1
$\kappa B = 20$	0.1	0.1	0.1
$c = 0.2$			
	$\delta = 0.05$	$\delta = 0.5$	$\delta = 5$
$\kappa B = 1$	0.2	0.2	0.2
$\kappa B = 5$	0.2	0.2	0.2
$\kappa B = 10$	0.2	0.2	0.2
$\kappa B = 20$	0.2	0.2	0.2
$c = 0.4$			
	$\delta = 0.05$	$\delta = 0.5$	$\delta = 5$
$\kappa B = 1$	0.4	0.4	0.4
$\kappa B = 5$	0.4	0.4	0.4
$\kappa B = 10$	0.4	0.4	0.4
$\kappa B = 20$	0.4	0.4	0.4
$c = 0.99$			
	$\delta = 0.05$	$\delta = 0.5$	$\delta = 5$
$\kappa B = 1$	0.99	0.99	0.99
$\kappa B = 5$	0.99	0.99	0.99
$\kappa B = 10$	0.99	0.99	0.99
$\kappa B = 20$	0.99	0.99	0.99

Table 3.1: The spectral radius values as computed from the discrete linear SUPG code for a variety of values for c , κB and δ .

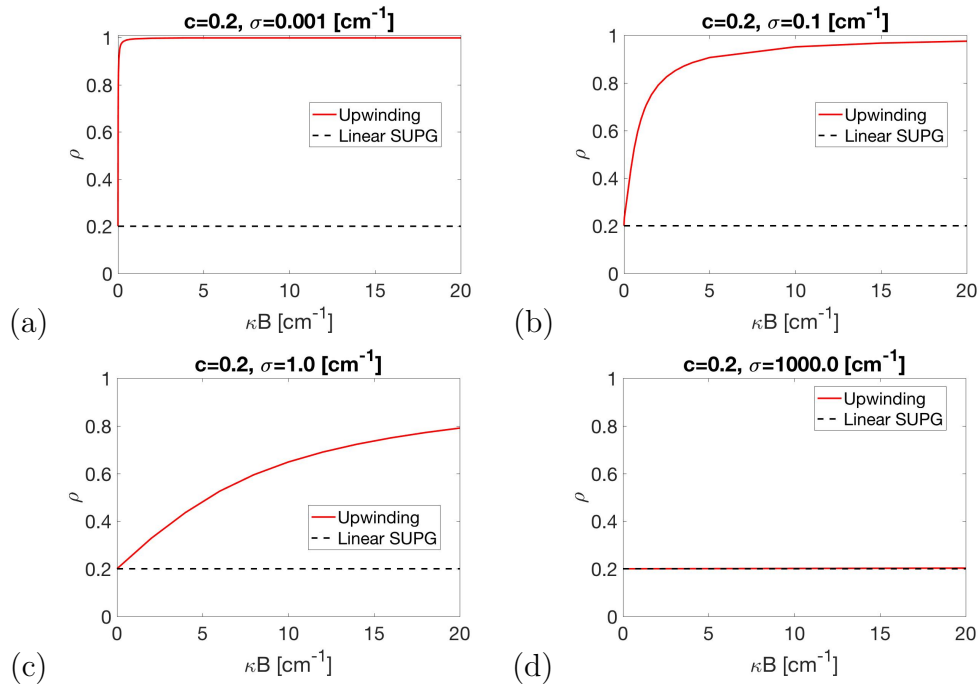


Figure 3.1: The spectral radius as a function of magnetic field parameter κB for the Upwinding scheme (solid line) and for the SUPG scheme (dotted line). Results are shown for (a) $\sigma = 0.001$, (b) $\sigma = 0.1$, (c) $\sigma = 1.0$, and (d) $\sigma = 1000.0$.

operator behaves in a diffusive manner. A system containing a high degree of advection without scatter to balance it will be unstable, while a system that has a high degree of scatter may require little to no stabilization. As a result, it is expected that the parameter δ should depend on the total cross-section, which in itself depends on material and energy. A higher cross-section value should require a smaller δ , and vice versa. Additionally, more finely resolved grids should require less stabilization, as was seen in the discussion of the Peclet number in Chapter 2.

3.4.1 Empirical Investigation

To determine appropriate values for δ , an empirical optimization was first performed in which the parameter was optimized over each energy group, one at a time, for homogeneous phantoms of lung and water. This allowed for the general shape and energy dependence to be determined. Optimal solutions were found by comparing the calculated fluence to the fluence that was calculated using the Upwind method. Optimization was performed such that the maximum percent difference over the whole phantom between the SUPG results and the Upwinding results was minimized. Each energy group was optimized and the value of δ fixed before proceeding to the next (lower) energy group sequentially.

During the initial investigation, three cases were considered:

- 1) 1.5 T parallel magnetic field, water,
- 2) 1.5 T perpendicular magnetic field, water,
- 3) 1.5 T parallel magnetic field, lung.

Some sample results of this investigation are plotted in Figure 3.2, showing the optimal δ value versus cross-section. The general take-away from this

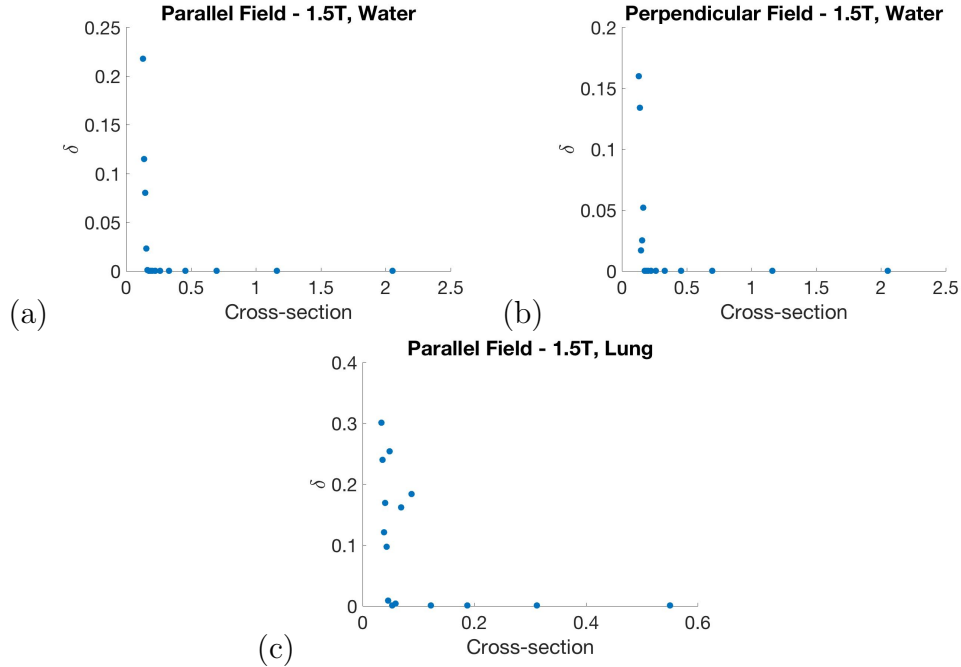


Figure 3.2: Some sample results of an empirical optimization for the SUPG parameter, δ . Optimization was performed over each energy group, and the parameter was chosen to maximize agreement with the Upwinding results. (a) 1.5 T parallel magnetic field, water, (b) 1.5 T perpendicular magnetic field, water, (c) 1.5 T parallel magnetic field, lung.

investigation is that the highest energies require the most stabilization, as the cross-sections here are small and thus advection dominates scatter, as was predicted. The SUPG parameter values drop fairly sharply as cross-section increases.

3.4.2 Hyperbolic Cotangent Formula

Fries and Matthies [39] and Brooks and Hughes [49] provide a hyperbolic cotangent form of the δ parameter that has been derived based on known solutions of the general advection-diffusion equation. The parameter is derived as a function of the diffusion coefficient and the advective velocity. In fact, the

formula given in the literature depends directly on the Peclet number: [39]

$$\delta \propto \frac{h}{2c} \left(\coth(Pe) - \frac{1}{Pe} \right), \quad (3.54)$$

where h is the spatial element size, c is the spatial advective velocity, and $Pe = \frac{ch}{2D}$, with D the spatial diffusion coefficient. As mentioned before, all previous applications of the SUPG method were in space, hence all parameters are with respect to spatial advection and diffusion. For our particular scenario, while there is no explicit diffusion and we cannot calculate a Peclet number, the scattering cross-section offers a very reasonable stand-in for the purposes of calculating δ . As such, we define a pseudo-Peclet number, denoted $\tilde{P}e$:

$$\tilde{P}e = \tilde{C} \frac{c\Delta\Omega}{2\sigma_T}, \quad (3.55)$$

where c is the angular advective velocity, given by the coefficient of the angular first derivative term. In the case of the z -magnetic field, $c = \kappa B_z$. $\Delta\Omega$ indicates the angular step size and has units of radians. Because the units on the scattering cross-section (d^2) are different from those of the diffusion coefficient (d^2/t), a constant \tilde{C} is included which has units of $\frac{td^2}{\text{rad}^2}$, in order to render the pseudo-Peclet number dimensionless. Then, Equation 3.54 can be used with the newly defined pseudo-Peclet number, and is given by

$$\delta = \alpha \frac{\Delta\Omega}{2c} \left(\coth \left(\frac{\tilde{C}c\Delta\Omega}{2\sigma_T} \right) - \frac{2\sigma_T}{\tilde{C}c\Delta\Omega} \right). \quad (3.56)$$

A constant of proportionality α , along with the constant \tilde{C} was varied in order to fit the formula for the different magnetic field strengths, configurations and materials. In our implementation, we took $\alpha = \tilde{C}$ and combined \tilde{C} and $\Delta\Omega$ into a single parameter C_δ for fitting. This reduces the problem to a one-dimensional optimization. C_δ was then determined for each material, evaluated

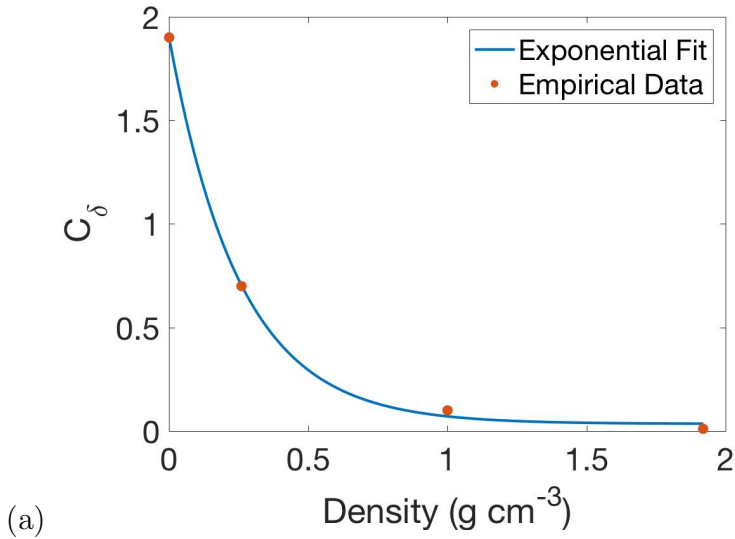


Figure 3.3: The relationship between C_δ and material density, determined empirically for bone, water, lung and air and fit exponentially.

based on the agreement of the calculated fluence to the reference distribution as calculated using the Upwinding technique. It was observed that the required value was inversely proportional to material density. As the data seemed to follow an exponential function, a curve was fit to the C_δ values for each of the four densities considered here (Bone, water, lung, air). The results are shown in Figure 3.3. The exponential equation used is given by

$$C_\delta = 0.034 + 1.87e^{-3.94\rho}. \quad (3.57)$$

Some sample plots of δ calculated based on Equation 3.56 and with constant C_δ determined from Equation 3.57 are shown in Figures 3.11-3.14 below. As before, the more diffusion or scattering that is present, the lower the value of δ . Additionally, high values of δ are required for low values of the scattering cross-section, with a sharp drop-off as scattering increases.

3.5 Simulation Results

We now present the results of simulating a beam in a phantom for a variety of material configurations and two different magnetic field strength/orientation combinations.

3.5.1 Calculation Geometry

Simulations are performed for a $2\text{ cm} \times 2\text{ cm}$ square field size using a $9.6 \times 9.6 \times 9.6\text{ cm}^3$ phantom. This field size was chosen as a small field with its associated charged particle disequilibrium makes for a challenging validation case. The beam used a 6 MV photon spectrum [24] originating from a point source with an SSD of 100 cm. In the beam and penumbra, 4 mm Cartesian voxels were used, with 8 mm voxels used in the surrounding volume, and 16 mm voxels at the edges of the phantom. In the angular domain, 32 triangular angular elements conformal to the unit sphere were used. In space, linear basis functions were selected while in angle, quadratic basis functions were used. The energy domain was discretized into 32 photon energies and 20 electron energies. Material cross-section values were determined using the CEPXS software [50] with Legendre expansion truncated at $L = 5$.

A series of homogeneous phantoms of lung ($\rho = 2.6 \times 10^{-1}\text{ g cm}^{-3}$), water ($\rho = 1.00\text{ g cm}^{-3}$) and bone ($\rho = 1.92\text{ g cm}^{-3}$) were used, as well as two different heterogeneous slab phantoms. The heterogeneous lung slab phantom had 4 cm of water, followed by 1.2 cm of bone, followed by 2.8 cm of lung, and 1.6 cm of water. The heterogeneous air slab phantom had 4 cm of water, followed by 1.2 cm of bone, followed by 2.8 cm of air ($\rho = 1.2 \times 10^{-3}\text{ g cm}^{-3}$), and 1.6 cm of water. Representations of these two phantoms are shown in Figure 3.4. The key difference is that the heterogeneous lung slab phantom used lung, while the heterogeneous air slab phantom used air. Two different

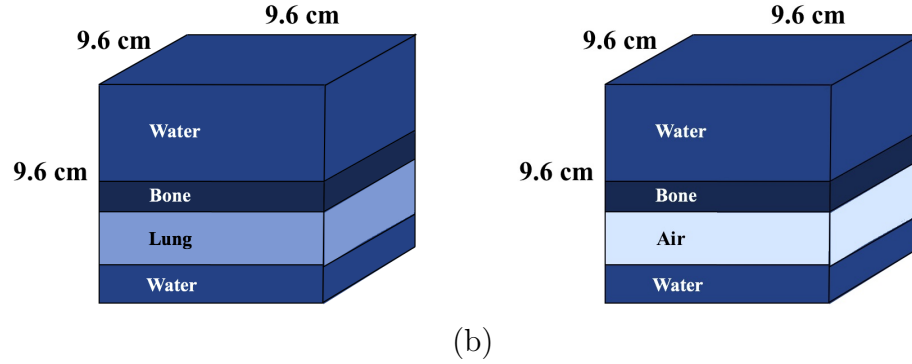


Figure 3.4: Schematic representations of the inhomogeneous phantoms used in the simulations for both the Upwinding method and the SUPG method. (a) The heterogeneous lung slab phantom is made up of 4 cm of water, followed by 1.2 cm of bone, followed by 2.8 cm of lung, and 1.6 cm of water. (b) The heterogeneous air slab phantom is made up of 4 cm of water, followed by 1.2 cm of bone, followed by 2.8 cm of air, and 1.6 cm of water

Linac-MR geometries are chosen, in particular, a 0.5 T parallel magnetic field configuration, and a 1.5 T perpendicular magnetic field configuration to coincide with the configurations found in existing Linac-MR systems. A beam was simulated for each geometry, for each phantom type.

3.5.2 Homogeneous Phantoms

In this section, the results of calculating the fluence in three different homogeneous phantoms are shown for both the case of a 0.5 T parallel magnetic field, and a 1.5 T perpendicular magnetic field. The results of simulations using $B_z = 0$ are also shown so that the effect of the magnetic field can be clearly seen.

0.5 T Parallel \vec{B} Field

Simulations for a 0.5 T parallel magnetic field are first shown for a lung phantom in Figure 3.5. In this case, it can be seen that the percentage depth doses, or PDD's for the linear SUPG method and the Upwinding method agree very

well, and that the overall maximum percent difference for depths greater than d_{\max} is 1.05%. Results for a water phantom are then shown in Figure 3.6, where it can be seen that the two methods show excellent agreement with a maximum percent difference for depths greater than d_{\max} of 0.033%. The results for the bone phantom in Figure 3.7 are better still, with a maximum percent difference for depths greater than d_{\max} of 0.0034%. A gamma analysis was performed using the criteria that only points having a dose greater than or equal to 10% of the maximum dose qualified for the calculation. This analysis had a passing rate of 100% (100%) at 2%/2 mm (3%/3 mm) for all three materials. These results are as expected, as for larger cross-sections the value of δ is smaller, thus introducing less artificial diffusion.

1.5 T Perpendicular \vec{B} Field

The simulation results for a 1.5 T perpendicular magnetic field are now shown. The results of applying both the SUPG scheme and Upwinding scheme in a lung phantom are shown in Figure 3.8. The 0 T magnetic field case is also shown for reference. It can be seen that the PDD's differ quite significantly, and the results appear noticeably over-diffusive. Low density media with a higher magnetic field strength provides the biggest challenge to any stabilization scheme. A maximum percent difference for depths greater than d_{\max} of 18.1% can be seen. The results for a water phantom are shown in Figure 3.9. As water is denser, we would expect to see improved results over the lung case. Better agreement can indeed be observed with a maximum percent difference for depths greater than d_{\max} of 1.9%. The results for a bone phantom are shown in Figure 3.10, where a maximum percent difference for depths greater than d_{\max} of 1.4% is observed, again at the phantom interface. A gamma analysis for each case showed a passing rate at 2%/2 mm (3%/3 mm) of 83.52% (92.39%) in lung, 100% (100%) in water and 100% (100%) in

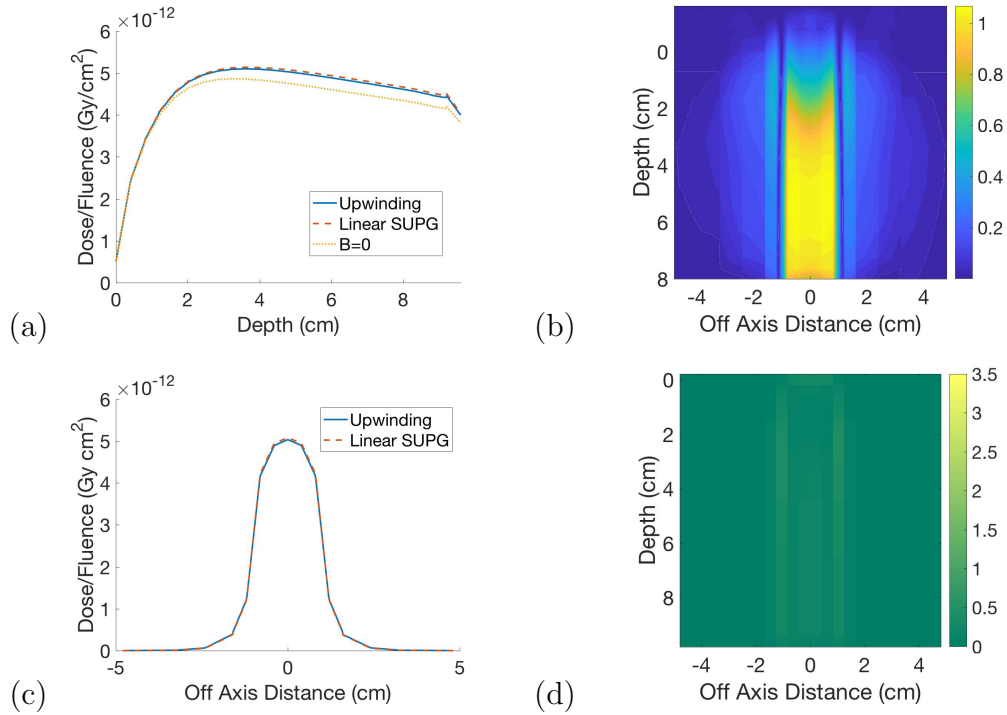


Figure 3.5: The results of simulating a $2 \times 2 \text{ cm}^2$ 6 MV photon beam using both the Upwinding scheme and the Linear SUPG method in a $9.6 \times 9.6 \times 9.6 \text{ cm}^3$ lung phantom in a 0.5 T parallel magnetic field. (a) PDD profiles down the center of the phantom for the Upwinding scheme (blue) and the Linear SUPG scheme (red). The 0 T magnetic field case is also shown (yellow). (b) A slice through the center of the phantom showing the % difference in dose as calculated by the two different methods. (c) Profiles across the center of the beam for the Upwinding scheme (blue) and the Linear SUPG scheme (red). (d) A gamma map at $2\%/2 \text{ mm}$.

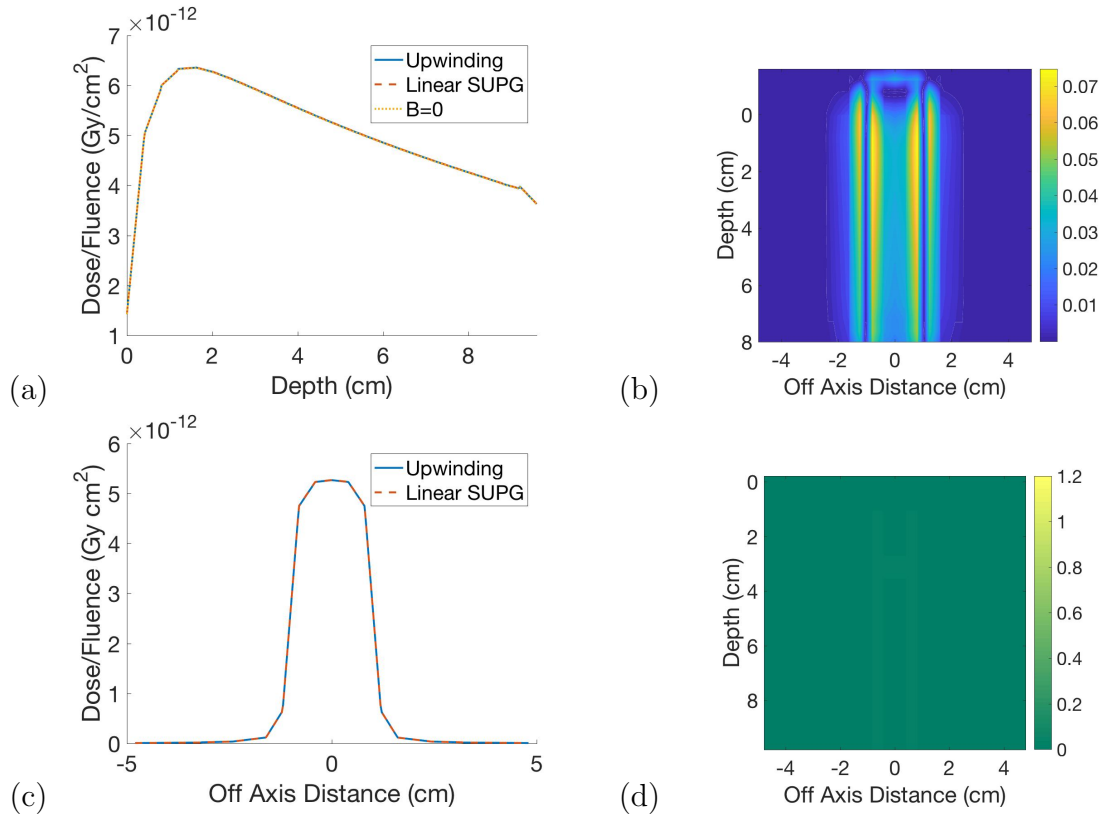


Figure 3.6: The results of simulating a $2 \times 2 \text{ cm}^2$ 6 MV photon beam using both the Upwinding scheme and the Linear SUPG method in a $9.6 \times 9.6 \times 9.6 \text{ cm}^3$ water phantom in a 0.5 T parallel magnetic field. (a) PDD profiles down the center of the phantom for the Upwinding scheme (blue) and the Linear SUPG scheme (red). The 0 T magnetic field case is also shown (yellow). (b) A slice through the center of the phantom showing the % difference in dose as calculated by the two different methods. (c) Profiles across the center of the beam for the Upwinding scheme (blue) and the Linear SUPG scheme (red). (d) A gamma map at 2%/2 mm.

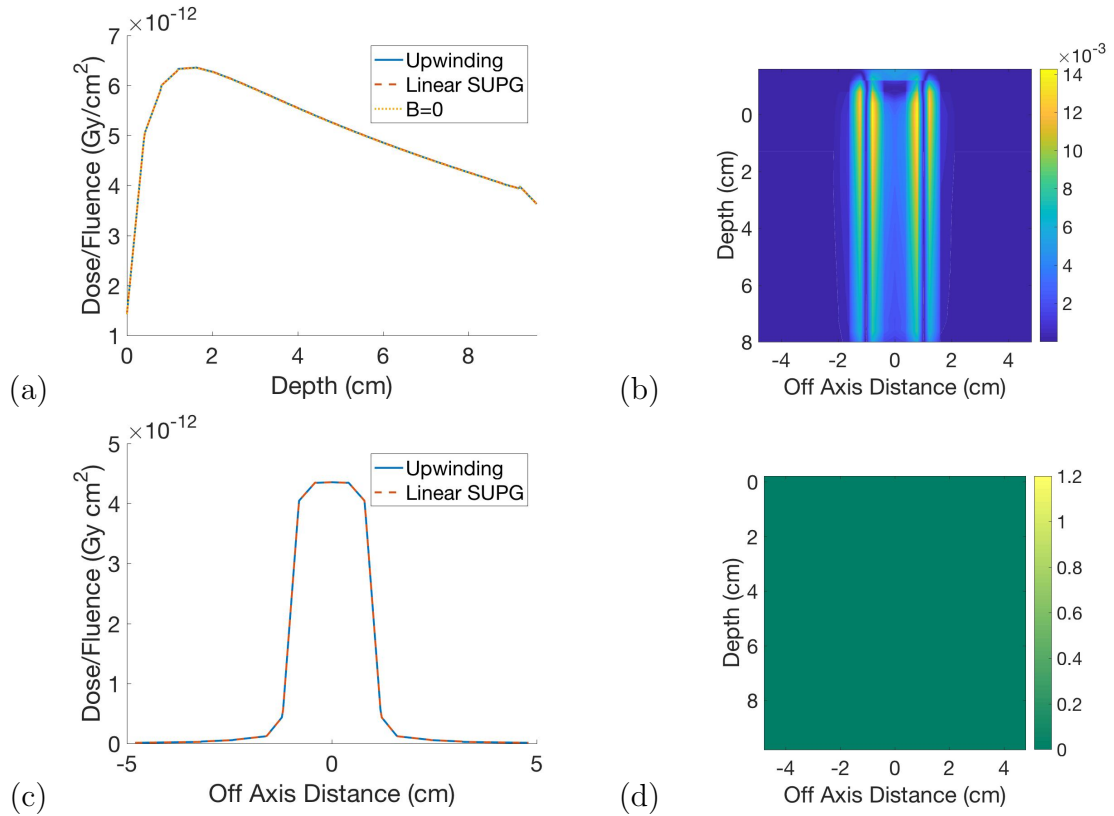


Figure 3.7: The results of simulating a $2 \times 2 \text{ cm}^2$ 6 MV photon beam using both the Upwinding scheme and the Linear SUPG method to $9.6 \times 9.6 \times 9.6 \text{ cm}^3$ bone phantom in a 0.5 T parallel magnetic field. (a) PDD profiles down the center of the phantom for the Upwinding scheme (blue) and the Linear SUPG scheme (red). The 0 T magnetic field case is also shown (yellow). (b) A slice through the center of the phantom showing the % difference in dose as calculated by the two different methods. (c) Profiles across the center of the beam for the Upwinding scheme (blue) and the Linear SUPG scheme (red). (d) A gamma map at 2%/2 mm.

bone. While 3%/3 mm gamma analysis is a reasonable metric to assess most clinical situations, it does not fully capture the agreement of the model in this case. Because the region of discrepancy is fairly small, a very good pass rate can be achieved while still seeing a difference of up to 18%.

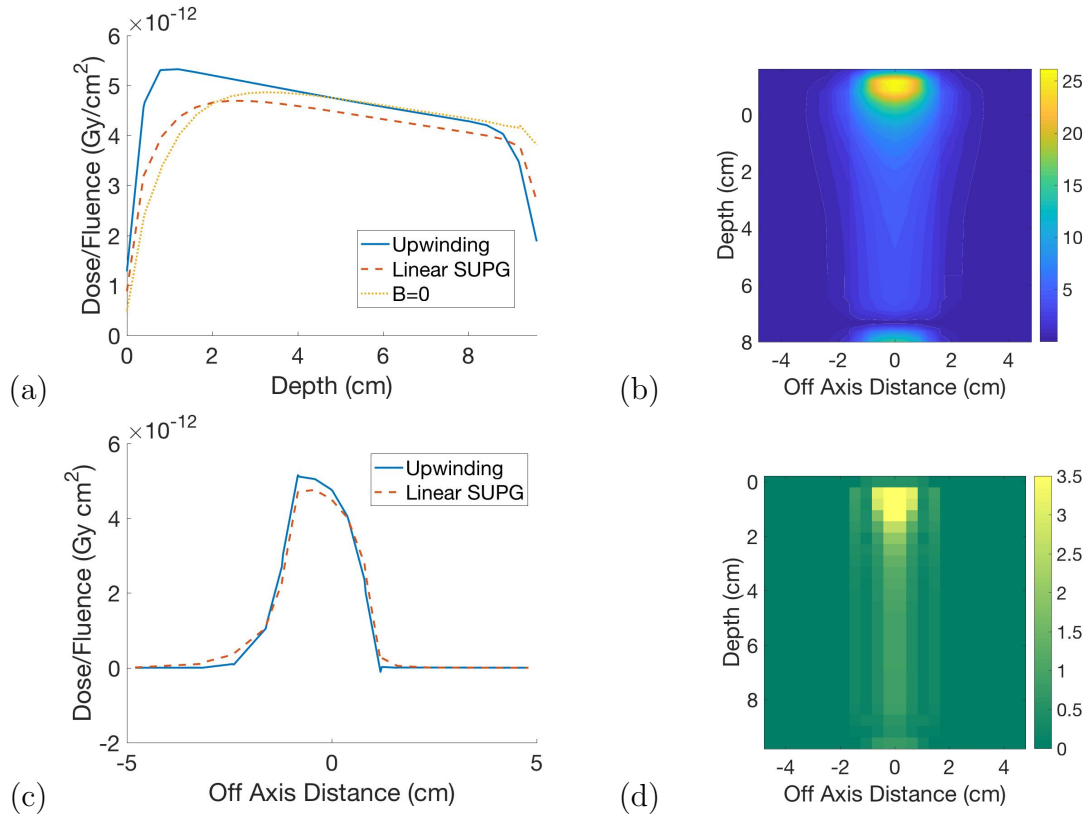


Figure 3.8: The results of simulating a $2 \times 2 \text{ cm}^2$ 6 MV photon beam using both the Upwinding scheme and the Linear SUPG method in a $9.6 \times 9.6 \times 9.6 \text{ cm}^3$ lung phantom in a 1.5 T perpendicular magnetic field. (a) PDD profiles down the center of the phantom for the Upwinding scheme (blue) and the Linear SUPG scheme (red). The 0 T magnetic field case is also shown (yellow). (b) A slice through the center of the phantom showing the % difference in dose as calculated by the two different methods. (c) Profiles across the center of the beam for the Upwinding scheme (blue) and the Linear SUPG scheme (red). (d) A gamma map at 2%/2 mm.

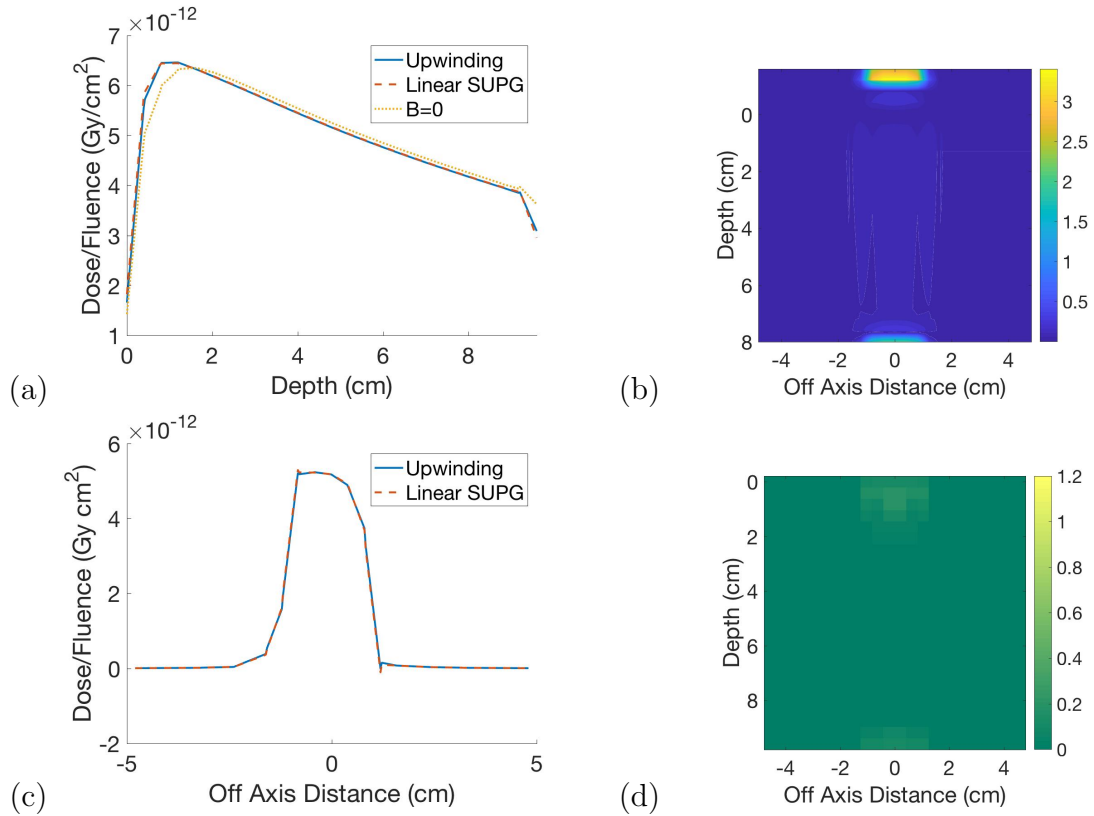


Figure 3.9: The results of simulating a $2 \times 2 \text{ cm}^2$ 6 MV photon beam using both the Upwinding scheme and the Linear SUPG method in a $9.6 \times 9.6 \times 9.6 \text{ cm}^3$ water phantom in a 1.5 T perpendicular magnetic field. (a) PDD profiles down the center of the phantom for the Upwinding scheme (blue) and the Linear SUPG scheme (red). The 0 T magnetic field case is also shown (yellow). (b) A slice through the center of the phantom showing the % difference in dose as calculated by the two different methods. (c) Profiles across the center of the beam for the Upwinding scheme (blue) and the Linear SUPG scheme (red). (d) A gamma map at $2\%/2 \text{ mm}$.

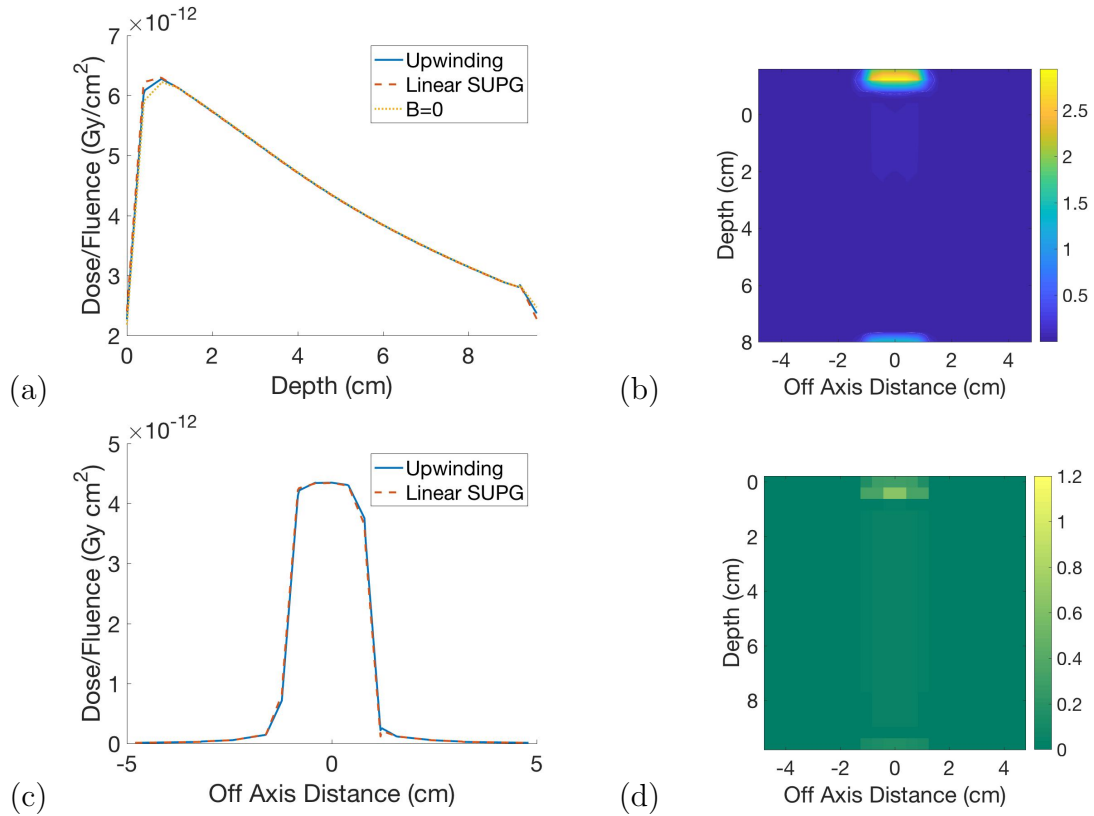


Figure 3.10: The results of simulating a $2 \times 2 \text{ cm}^2$ 6 MV photon beam using both the Upwinding scheme and the Linear SUPG method in a $9.6 \times 9.6 \times 9.6 \text{ cm}^3$ bone phantom in a 1.5 T perpendicular magnetic field. (a) PDD profiles down the center of the phantom for the Upwinding scheme (blue) and the Linear SUPG scheme (red). The 0 T magnetic field case is also shown (yellow). (b) A slice through the center of the phantom showing the % difference in dose as calculated by the two different methods. (c) Profiles across the center of the beam for the Upwinding scheme (blue) and the Linear SUPG scheme (red). (d) A gamma map at $2\%/2 \text{ mm}$.

3.5.3 Heterogeneous Phantoms

Results of simulating the LBTE with magnetic fields using the linear SUPG method for heterogeneous phantoms are now provided, as in clinical situations we often encounter heterogeneous situations. Additionally, heterogeneous geometries provide a much more challenging test of the method, as material interfaces create rapid changes in the fluence in the presence of a magnetic field. The results for the case of 0 T magnetic field are also shown in these plots so that the effect of the magnetic field can be clearly visualized.

0.5 T Parallel \vec{B} Field

The results of applying the Linear SUPG method to the heterogeneous lung slab phantom in a 0.5 T parallel magnetic field are shown in Figure 3.11. It can be seen that for this low magnetic field strength, the linear SUPG method shows very good agreement with the Upwinding results. In this case, a small amount of angular advection is present due to the low field strength, and thus the SUPG parameter can be kept quite small, (Figure 3.11 f). A gamma analysis had a passing rate of 99.14% (100%) at 2%/2 mm (3%/3 mm). Additionally, the maximum percent difference for depths greater than d_{\max} was 0.25%.

The results for the heterogeneous air slab phantom in a 0.5 T parallel magnetic field are shown in Figure 3.12. It can be seen that the linear SUPG method still shows excellent accuracy in the water and bone tissue, however, the accuracy is degraded in air. This is due to the advection dominating the small amount of scatter present as a result of the very low density medium. It can be seen that a much larger δ value is required for stabilization, negatively impacting the accuracy in this region. In this case, the gamma analysis had a passing rate of 73.11% (82.35%) at 2%/2 mm (3%/3 mm). the maximum percent difference for depths greater than d_{\max} was 31.1%. These results indicate

that dose in air is very challenging for the SUPG method to capture.

1.5 T Perpendicular \vec{B} Field

The results of applying the Linear SUPG method to the lung phantom in a 1.5 T perpendicular magnetic field are shown in Figure 3.13. The agreement is also degraded for this case, where the higher magnetic field creates more angular advection and thus more stabilization is required. The result is that the SUPG simulations are over-diffusive, which negatively affects the accuracy of the scheme. Additionally, the benefit of the improved convergence is more pronounced in the higher magnetic field. A gamma analysis had a passing rate of 89.38% (96.26%) at 2%/2 mm (3%/3 mm). The maximum percent difference for depths greater than d_{\max} was 25.0%.

The results of applying the method to the air phantom in a 1.5 T perpendicular magnetic field are shown in Figure 3.14. The agreement is still excellent in water and bone, however a very high δ value is required to stabilize the system in such sparse media for a higher magnetic field. This negatively impacts the accuracy in the low density region, causing the resulting fluence to be over-diffusive, and failing to capture the peak resulting from the material interface. However, in this case, the improved convergence rate can be clearly seen, with the linear SUPG method requiring less than half as many iterations to converge as the Upwinding method for some energy groups. For this case, the gamma analysis had a passing rate of 89.78% (94.75%) at 2%/2 mm (3%/3 mm). This may seem counterintuitive, but as some of the dose in this case is very low, fewer points qualified based on the minimum dose requirement allowing for a higher gamma pass rate to be attained. As such, the maximum percent difference for depths greater than d_{\max} was 52.0%, occurring in the air region. Likewise in this case, while the 3%/3 mm gamma analysis achieves a high pass rate, it is not completely indicative of the agreement of the model.

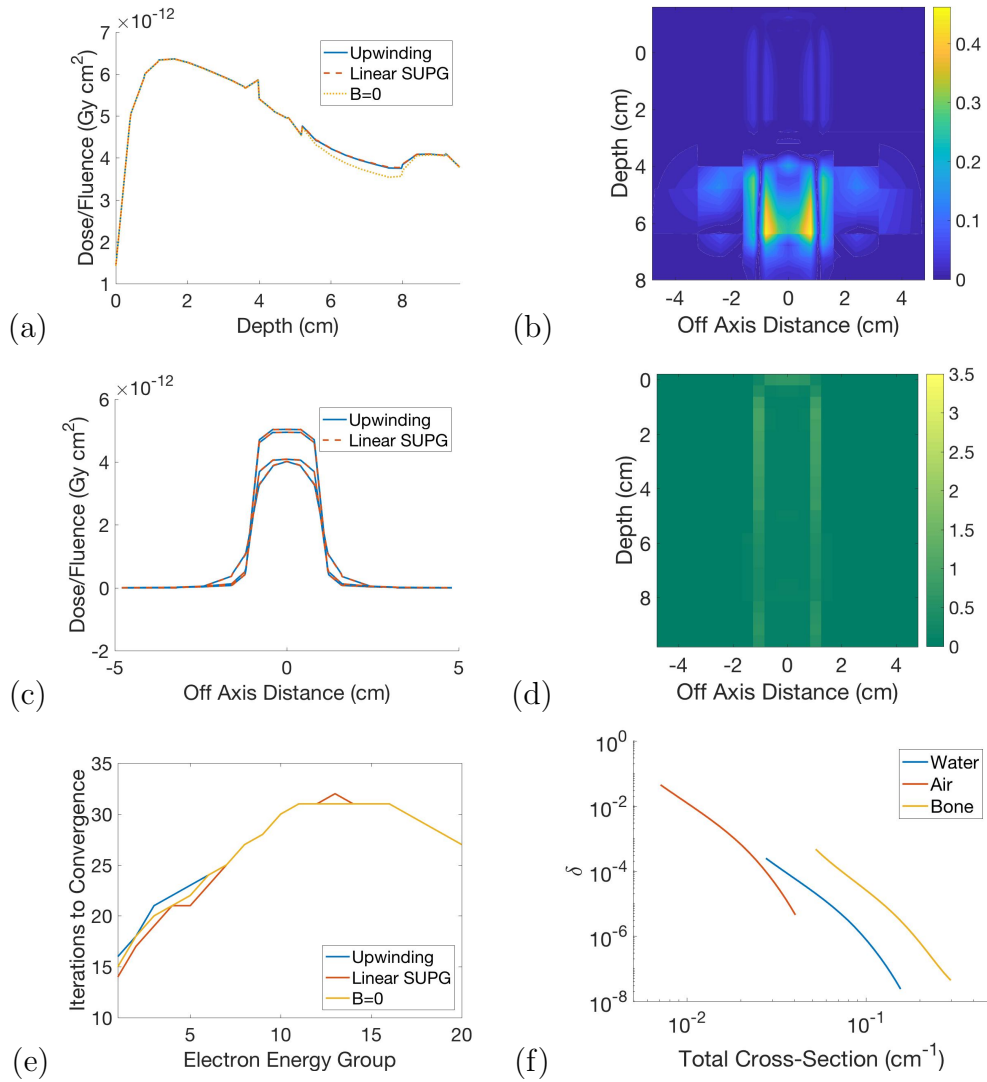


Figure 3.11: The results of simulating a $2 \times 2 \text{ cm}^2$ 6 MV photon beam using both the Upwinding scheme and the Linear SUPG method in a $9.6 \times 9.6 \times 9.6 \text{ cm}^3$ heterogeneous lung slab phantom in a 0.5 T parallel magnetic field. (a) PDD profiles down the center of the phantom for the Upwinding scheme (blue) and the Linear SUPG scheme (red). The 0 T magnetic field case is also shown (yellow). (b) A slice through the center of the phantom showing the % difference in dose as calculated by the two different methods. (c) Profiles across the center of each material section for the Upwinding scheme (blue) and the Linear SUPG scheme (red). (d) A gamma map at 2%/2 mm. (e): the number of iterations required to converge each energy group for the Upwinding scheme (blue) and the Linear SUPG method (red). (f): the value of δ for each material as a function of total cross-section.

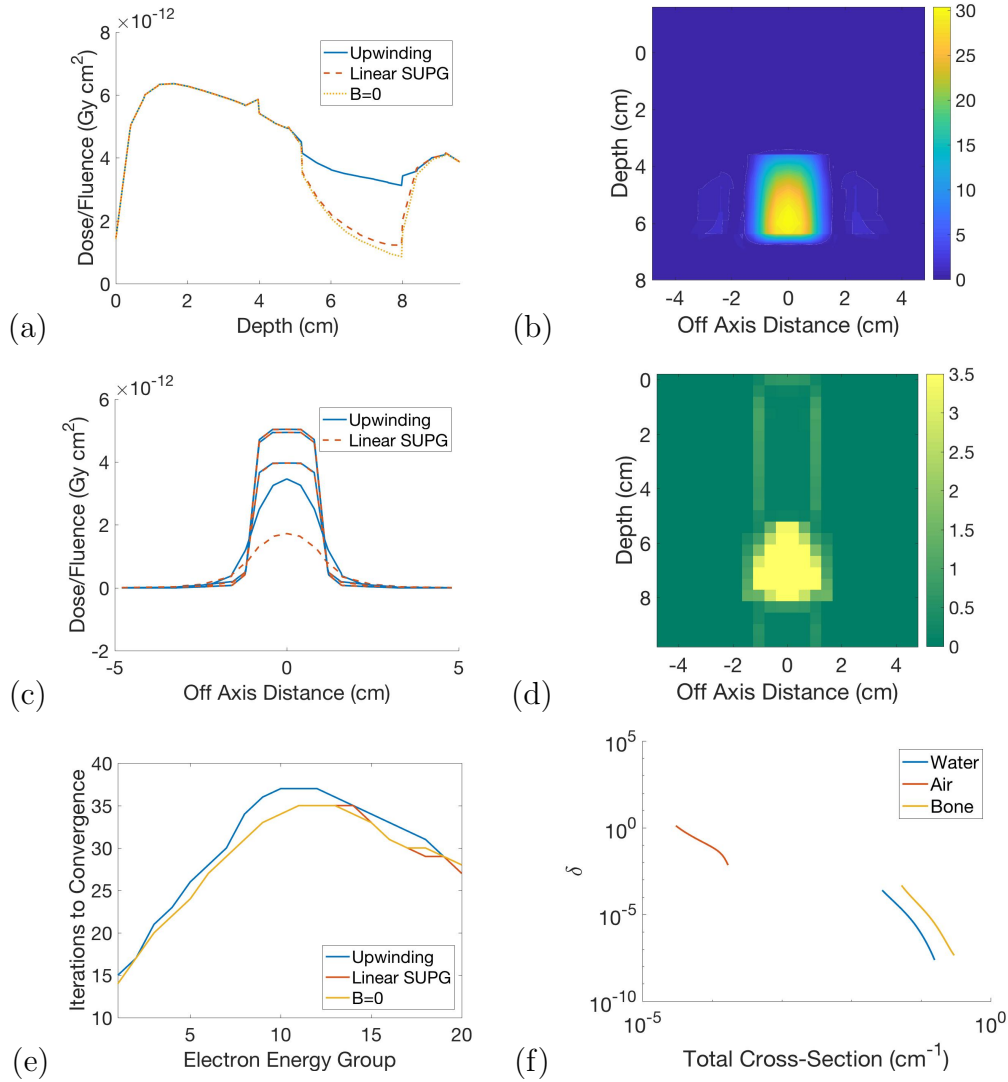


Figure 3.12: The results of simulating a $2 \times 2 \text{ cm}^2$ 6 MV photon beam using both the Upwinding scheme and the Linear SUPG method in a $9.6 \times 9.6 \times 9.6 \text{ cm}^3$ heterogeneous air slab phantom in a 0.5 T parallel magnetic field. (a) PDD profiles down the center of the phantom for the Upwinding scheme (blue) and the Linear SUPG scheme (red). The 0 T magnetic field case is also shown (yellow). (b) A slice through the center of the phantom showing the % difference in dose as calculated by the two different methods. (c) Profiles across the center of each material section for the Upwinding scheme (blue) and the Linear SUPG scheme (red). (d) A gamma map at 2%/2 mm. (e): the number of iterations required to converge each energy group for the Upwinding scheme (blue) and the Linear SUPG method (red). (f): the value of δ for each material as a function of total cross-section.

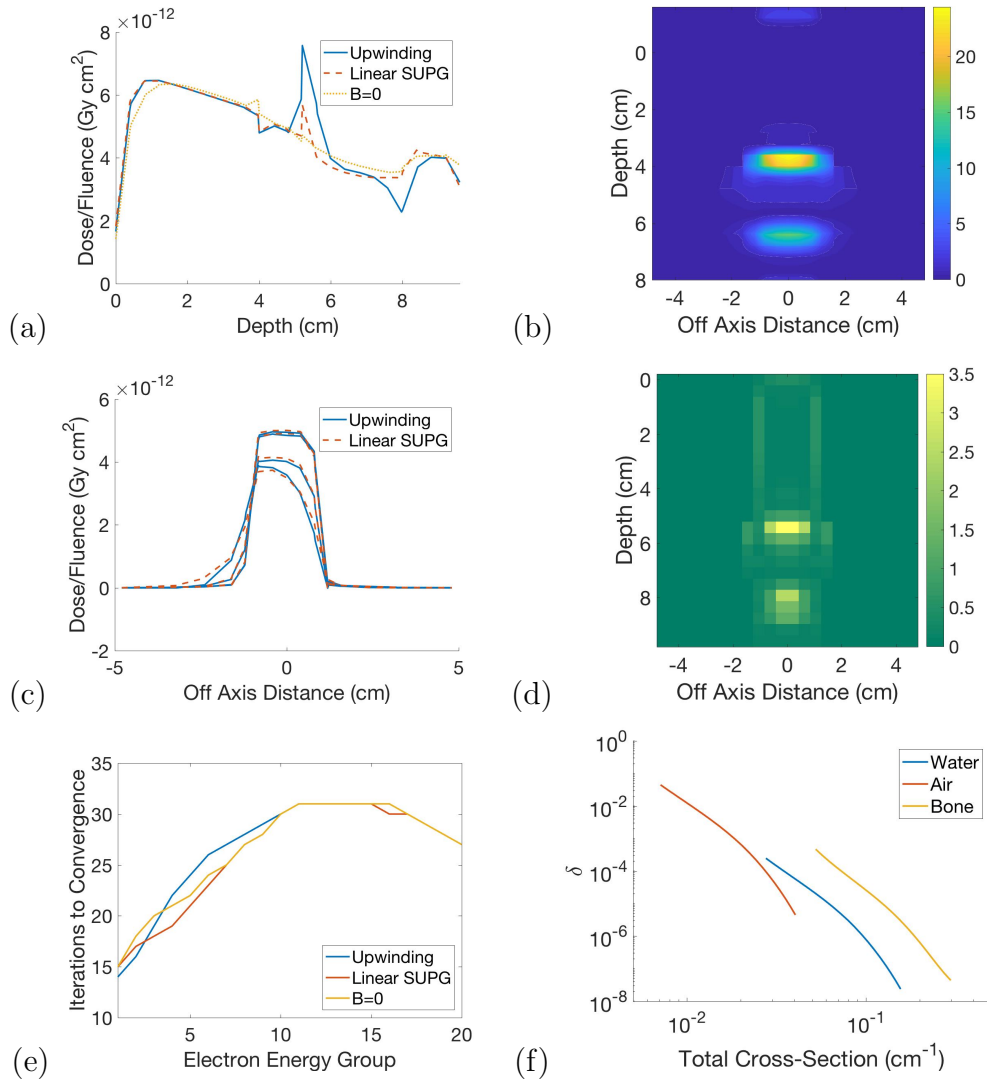


Figure 3.13: The results of simulating a $2 \times 2 \text{ cm}^2$ 6 MV photon beam using both the Upwinding scheme and the Linear SUPG method in a $9.6 \times 9.6 \times 9.6 \text{ cm}^3$ heterogeneous lung slab phantom in a 1.5 T perpendicular magnetic field. (a) PDD profiles down the center of the phantom for the Upwinding scheme (blue) and the Linear SUPG scheme (red). The 0 T magnetic field case is also shown (yellow). (b) A slice through the center of the phantom showing the % difference in dose as calculated by the two different methods. (c) Profiles across the center of each material section for the Upwinding scheme (blue) and the Linear SUPG scheme (red). (d) A gamma map at 2%/2 mm. (e): the number of iterations required to converge each energy group for the Upwinding scheme (blue) and the Linear SUPG method (red). (f): the value of δ for each material as a function of total cross-section.

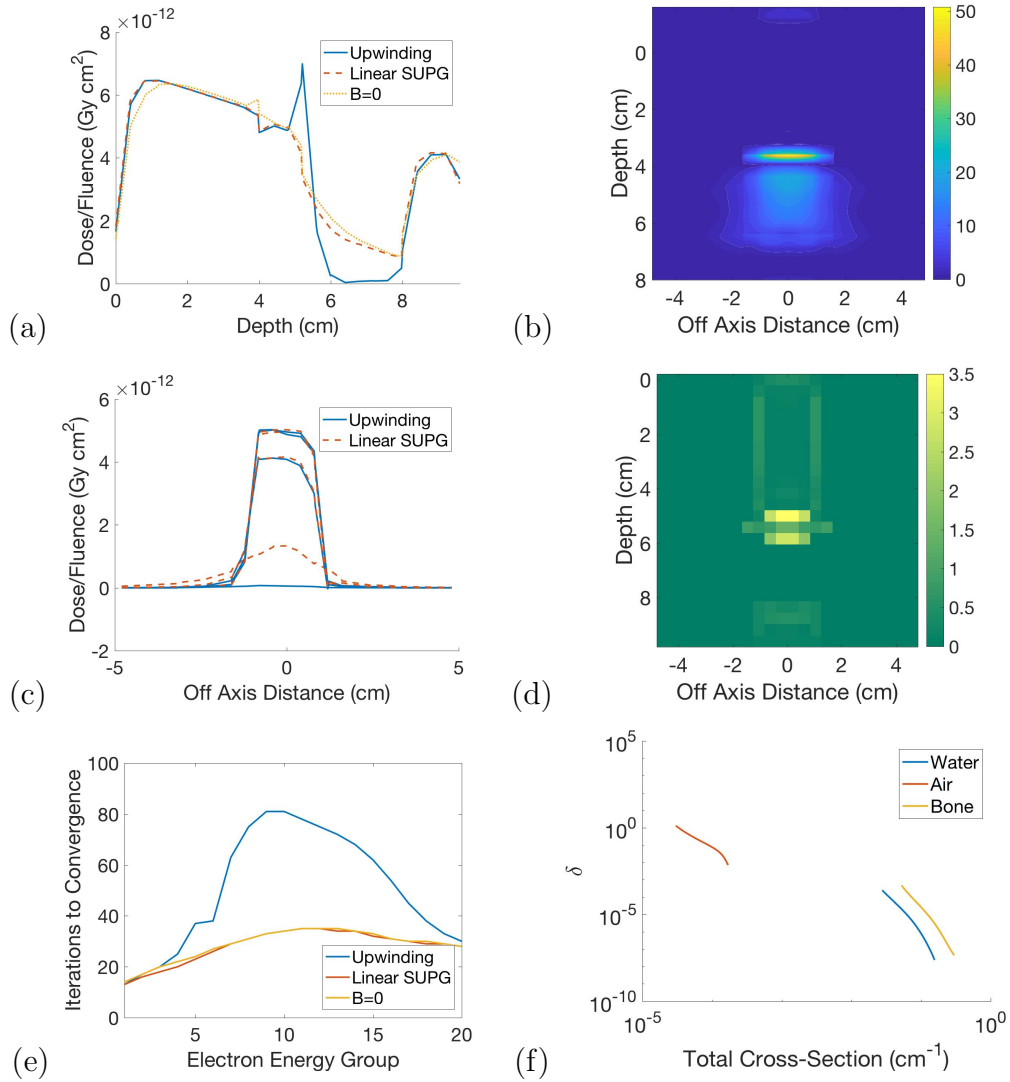


Figure 3.14: The results of simulating a $2 \times 2 \text{ cm}^2$ 6 MV photon beam using both the Upwinding scheme and the Linear SUPG method in a $9.6 \times 9.6 \times 9.6 \text{ cm}^3$ heterogeneous air slab phantom in a 1.5 T perpendicular magnetic field. (a) PDD profiles down the center of the phantom for the Upwinding scheme (blue) and the Linear SUPG scheme (red). The 0 T magnetic field case is also shown (yellow). (b) A slice through the center of the phantom showing the % difference in dose as calculated by the two different methods. (c) Profiles across the center of each material section for the Upwinding scheme (blue) and the Linear SUPG scheme (red). (d) A gamma map at 2%/2 mm. (e): the number of iterations required to converge each energy group for the Upwinding scheme (blue) and the Linear SUPG method (red). (f): the value of δ for each material as a function of total cross-section.

Chapter 4

Non-Linear SUPG Formulation

The linear SUPG formulation provides stabilization by introducing artificial diffusion in the streamline direction, the amount of which can be varied depending on the amount of scatter present. However, because the diffusion is added only in the streamline (advection) direction, at times too much artificial diffusion is required for stability thus reducing the accuracy. This effect is particularly pronounced in low density media where advection dominates. A proposed solution is to use a non-linear scheme in which the artificial diffusion now depends on the solution gradient, both in magnitude and direction. This effectively adds diffusion in the cross-wind direction, potentially dampening oscillations with less effect on the accuracy than in the linear SUPG case. Additionally, due to the dependence on the solution gradient, regions with a steeper gradient will introduce more diffusion. Prior work by Merton [51] as well as Pain et al. [52] has shown excellent accuracy results using a non-linear SUPG method for stabilization of the radiation transport spatial advection term, even in very low density media. This suggests we may see improvement in accuracy by using a non-linear SUPG scheme in angle in addition to the current linear SUPG scheme. As was the case for linear SUPG, this method has previously only been explored for spatial discretization, with the application

to angular advection being a novel advancement.

4.1 One-dimension in Space

In this section, the theory behind the development of this method is outlined. The application to the angular advection term of the LBTE with magnetic fields will then be derived. Following the works of Merton [51] and Hughes et al. [53], a one-dimensional, time-dependant, spatial case is first considered. An example in space is first given, followed by the analogous novel angular derivation. Begin with the simple equation

$$\vec{a} \cdot \nabla_{xt}\psi + \sigma\psi = 0, \quad (4.1)$$

where $\vec{a} = (a_t, a_x)^T$, and $\nabla_{xt} = \left(\frac{\partial\psi}{\partial t}, \frac{\partial\psi}{\partial x}\right)^T$. The modified weighting function will be based on the projection of \vec{a} onto ∇_{xt} . Taking θ_a to be the angle between these two vectors, then the cosine rule gives

$$\cos(\theta_a) = \frac{\vec{a} \cdot \nabla_{xt}\psi}{|\vec{a}||\nabla_{xt}\psi|}. \quad (4.2)$$

In this case, the norm used is simply the Euclidean, or L2-norm, i.e.

$$|\vec{a}| = \sqrt{a_t^2 + a_x^2}.$$

The projection of \vec{a} onto ∇_{xt} is given by

$$\vec{a}^* = |\vec{a}|\vec{n} \cos(\theta_a), \quad (4.3)$$

with $\vec{n} = \frac{\nabla_{xt}\psi}{|\nabla_{xt}\psi|}$. Substituting Equation 4.2 into Equation 4.3 and simplifying gives

$$\vec{a}^* = \frac{(\vec{a} \cdot \nabla_{xt}\psi)\nabla_{xt}\psi}{\|\nabla_{xt}\psi\|^2}. \quad (4.4)$$

Then, as per Merton [51], in this case, the non-linear Petrov-Galerkin method can be applied in a similar manner as for the linear Petrov-Galerkin, via a modification of the weighting function. For this simple example then, the method would take the form

$$(1 - \nabla_{xt} \cdot \vec{a}^* p^*)(\vec{a} \cdot \nabla_{xt}\psi + \sigma\psi - s) = 0. \quad (4.5)$$

The parameter p^* can then be chosen in several different ways. Some options given in [51] include:

$$p^* = \frac{1}{4} (|\vec{a}^* \cdot \nabla_{xt} N_{xti}|)^{-1}, \quad (4.6)$$

where N_{xti} is the i^{th} basis (weighting) function. An alternative form uses the space-time Jacobian matrix \vec{J}_{xt} :

$$p^* = \frac{1}{4} \left(\|\vec{J}_{xt}^{-1} \vec{a}^*\|_2 \right)^{-1}. \quad (4.7)$$

This method is also employed in Hughes et al. [53] with slightly different notation and a simpler form of p^* from above. In this case, and in our implementation, the non-linear term is simply added to the weighting function in the same manner as the linear SUPG term. Note that the linear SUPG term is also added, so that both streamline and crosswind diffusion are present. Then, the suggested modified weighting function is

$$\tilde{w} = w^h + \tau_1 \vec{a} \cdot \nabla w^h + \tau_2 \vec{a}^* \cdot \nabla w^h, \quad (4.8)$$

where the first term w^h gives the original FEM weighting function, the second term gives the streamline diffusion, or linear Petrov Galerkin term, and the final term corresponds to the non-linear Petrov-Galerkin term. In particular, τ_1 in this notation is equivalent to the δ of our earlier derivation. The derived form of the non-linear term from Merton [51] and Pain et al. [52] shown above is an extension of this early method, with a more sophisticated method of controlling the amount of diffusion added, i.e., various forms of p^* .

4.2 Application to Angular Advection

In order to apply this non-linear method to the LBTE with magnetic fields, \vec{a}^* must be defined. This term is based on the advection term in the full equation, and is given by Equation 4.4, where \vec{a} gives the angular advective velocity, i.e., the angular advection term can be written as $\vec{a} \cdot \nabla_\Omega \Psi$. As above, without loss of generality, the case of a z -magnetic field is considered, i.e. $\vec{B} = B_z \hat{z}$. In this case then,

$$\vec{a} = (\kappa B_z \sqrt{1 - \mu^2}, 0), \quad (4.9)$$

and

$$\nabla_\Omega = \left(\frac{1}{\sqrt{1 - \mu^2}} \frac{\partial}{\partial \phi}, \frac{\partial}{\partial \theta} \right). \quad (4.10)$$

Note that since $\mu = \cos \theta$, $\sqrt{1 - \mu^2} = \sin \theta$, as it will be written henceforth. Then the weak formulation incorporating both the standard streamline diffusion modification as well as the non-linear SUPG term is given by

$$\left\langle \mathcal{L}\psi, \Upsilon + \delta \kappa B_z \frac{\partial \Upsilon}{\partial \phi} + \tau_2 \vec{a}^* \cdot \nabla_\Omega \Upsilon \right\rangle = \left\langle Q, \Upsilon + \delta \kappa B_z \frac{\partial \Upsilon}{\partial \phi} + \tau_2 \vec{a}^* \cdot \nabla_\Omega \Upsilon \right\rangle. \quad (4.11)$$

The non-linear diffusion term has been introduced directly in an amount given by τ_2 , and the linear SUPG term is still controlled by the parameter δ . This

equation can then be split up as was done for the case of the linear SUPG derivation:

$$\begin{aligned}
& \underbrace{\langle \mathcal{L}\psi, \Upsilon \rangle}_{\text{(I)}} + \underbrace{\left\langle \mathcal{L}\psi, \delta\kappa B_z \frac{\partial \Upsilon}{\partial \phi} \right\rangle}_{\text{(II)}} + \underbrace{\langle \mathcal{L}\psi, \tau_2 \vec{a}^* \cdot \nabla_\Omega \Upsilon \rangle}_{\text{(III)}} \\
& = \underbrace{\langle Q, \Upsilon \rangle}_{\text{(IV)}} + \underbrace{\left\langle Q, \delta\kappa B_z \frac{\partial \Upsilon}{\partial \phi} \right\rangle}_{\text{(V)}} + \underbrace{\langle Q, \tau_2 \vec{a}^* \cdot \nabla_\Omega \Upsilon \rangle}_{\text{(VI)}}. \quad (4.12)
\end{aligned}$$

Terms (I), (II), (IV) and (V) have already been calculated previously in Chapter 3, thus only terms (III) and (VI) need now be considered.

Term (III): Before constructing terms (III) and (VI), the weighting function must be expanded to determine how all the components are incorporated. Beginning with the full non-linear weighting function:

$$\tau_2 \vec{a}^* \cdot \nabla_\Omega \Upsilon = \tau_2 \left(\frac{(\vec{a} \cdot \nabla_\Omega \psi)}{|\nabla_\Omega \psi|_2^2} \nabla_\Omega \psi \right) \cdot \left(\frac{1}{\sin \theta} \frac{\partial}{\partial \phi}, \frac{\partial}{\partial \theta} \right) \lambda_j(\vec{r}) \gamma_q(\vec{\Omega}). \quad (4.13)$$

First consider the piece $\vec{a} \cdot \nabla_\Omega \psi$, where the finite element expansion of ψ is used

$$\vec{a} \cdot \nabla_\Omega \psi = (\kappa B_z \sin \theta, 0) \cdot \left(\frac{1}{\sin \theta} \frac{\partial}{\partial \phi}, \frac{\partial}{\partial \theta} \right) \sum_{i=1}^I \sum_{p=1}^P \psi_{ip} \lambda_i(\vec{r}) \gamma_p(\vec{\Omega}) \quad (4.14)$$

$$= \sum_{i=1}^I \sum_{p=1}^P \kappa B_z \psi_{ip} \lambda_i(\vec{r}) \frac{\partial \gamma_p(\vec{\Omega})}{\partial \phi}. \quad (4.15)$$

Now looking at $|\nabla_{\Omega}\psi|_2^2$:

$$|\nabla_{\Omega}\psi|_2^2 = \left| \left(\frac{1}{\sin\theta} \frac{\partial}{\partial\phi}, \frac{\partial}{\partial\theta} \right) \sum_{i=1}^I \sum_{p=1}^P \psi_{ip} \lambda_i(\vec{r}) \gamma_p(\vec{\Omega}) \right|_2^2 \quad (4.16)$$

$$= \left(\sum_{i=1}^I \sum_{p=1}^P \psi_{ip} \frac{\lambda_i(\vec{r})}{\sin\theta} \frac{\partial\gamma_p(\vec{\Omega})}{\partial\phi}, \sum_{i=1}^I \sum_{p=1}^P \psi_{ip} \lambda_i(\vec{r}) \frac{\partial\gamma_p(\vec{\Omega})}{\partial\theta} \right) \cdot \left(\sum_{i=1}^I \sum_{p=1}^P \psi_{ip} \frac{\lambda_i(\vec{r})}{\sin\theta} \frac{\partial\gamma_p(\vec{\Omega})}{\partial\phi}, \sum_{i=1}^I \sum_{p=1}^P \psi_{ip} \lambda_i(\vec{r}) \frac{\partial\gamma_p(\vec{\Omega})}{\partial\theta} \right) \quad (4.17)$$

$$= \frac{1}{\sin^2\theta} \left(\sum_{i=1}^I \sum_{p=1}^P \psi_{ip} \lambda_i(\vec{r}) \frac{\partial\gamma_p(\vec{\Omega})}{\partial\phi} \right)^2 + \left(\sum_{i=1}^I \sum_{p=1}^P \psi_{ip} \lambda_i(\vec{r}) \frac{\partial\gamma_p(\vec{\Omega})}{\partial\theta} \right)^2. \quad (4.18)$$

Then the new non-linear modified weighting term is given by

$$\begin{aligned} \tau_2 \vec{a}^* \cdot \nabla_{\Omega} \Upsilon &= \frac{\tau_2 \kappa B_z \sin^2\theta \left(\sum_{i=1}^I \sum_{p=1}^P \psi_{ip} \lambda_i(\vec{r}) \frac{\partial\gamma_p(\vec{\Omega})}{\partial\phi} \right)}{\left(\sum_{i=1}^I \sum_{p=1}^P \psi_{ip} \lambda_i(\vec{r}) \frac{\partial\gamma_p(\vec{r})}{\partial\phi} \right)^2 + \sin^2\theta \left(\sum_{i=1}^I \sum_{p=1}^P \psi_{ip} \lambda_i(\vec{r}) \frac{\partial\gamma_p(\vec{r})}{\partial\theta} \right)^2} \\ &\cdot \left[\left(\frac{1}{\sin\theta} \sum_{i=1}^I \sum_{p=1}^P \psi_{ip} \lambda_i(\vec{r}) \frac{\partial\gamma_p(\vec{\Omega})}{\partial\phi}, \sum_{i=1}^I \sum_{p=1}^P \psi_{ip} \lambda_i(\vec{r}) \frac{\partial\gamma_p(\vec{\Omega})}{\partial\theta} \right) \right. \\ &\cdot \left. \left(\frac{1}{\sin\theta} \lambda_j(\vec{r}) \frac{\partial\gamma_q(\vec{\Omega})}{\partial\phi}, \lambda_j(\vec{r}) \frac{\partial\gamma_q(\vec{\Omega})}{\partial\theta} \right) \right] \end{aligned} \quad (4.19)$$

$$(4.20)$$

To simplify the above expressions, the following quantities are introduced:

$$\eta_1(\vec{r}, \vec{\Omega}) = \sum_{i=1}^I \sum_{p=1}^P \psi_{ip} \lambda_i(\vec{r}) \frac{\partial\gamma_p(\vec{\Omega})}{\partial\phi} \quad (4.21)$$

$$\eta_2(\vec{r}, \vec{\Omega}) = \sum_{i=1}^I \sum_{p=1}^P \psi_{ip} \lambda_i(\vec{r}) \frac{\partial\gamma_p(\vec{\Omega})}{\partial\theta} \quad (4.22)$$

$$\chi(\vec{r}, \vec{\Omega}) = \frac{\eta_1(\vec{r}, \vec{\Omega})}{\eta_1^2(\vec{r}, \vec{\Omega}) + \sin^2\theta \eta_2^2(\vec{r}, \vec{\Omega})}. \quad (4.23)$$

Using these simplifying expressions, the non-linear modified weighting function can be written as

$$\tau_2 \vec{a}^* \cdot \nabla_{\Omega} \Upsilon = \tau_2 \kappa B_z \chi(\vec{r}, \vec{\Omega}) \cdot \left(\lambda_j(\vec{r}) \frac{\partial \gamma_q(\vec{\Omega})}{\partial \phi} \eta_1(\vec{r}, \vec{\Omega}) + \sin^2 \theta \lambda_j(\vec{r}) \frac{\partial \gamma_q(\vec{\Omega})}{\partial \theta} \eta_2(\vec{r}, \vec{\Omega}) \right). \quad (4.24)$$

Then consider term (III) of Equation 4.12:

$$\begin{aligned} \langle \mathcal{L} \psi, \tau_2 \vec{a}^* \cdot \nabla_{\Omega} \Upsilon \rangle = & \left\langle \underbrace{\vec{\Omega} \cdot \nabla \left(\sum_{i=1}^I \sum_{p=1}^P \psi_{ip} \lambda_i(\vec{r}) \gamma_p(\vec{\Omega}) \right)}_{(i)} \right. \\ & + \underbrace{\kappa B_z \frac{\partial}{\partial \phi} \left(\sum_{i=1}^I \sum_{p=1}^P \psi_{ip} \lambda_i(\vec{r}) \gamma_p(\vec{\Omega}) \right)}_{(ii)} \\ & \left. + \underbrace{\sigma_T(\vec{r}) \left(\sum_{i=1}^I \sum_{p=1}^P \psi_{ip} \lambda_i(\vec{r}) \gamma_p(\vec{\Omega}) \right)}_{(iii)}, \tau_2 \vec{a}^* \cdot \nabla_{\Omega} \Upsilon \right\rangle. \quad (4.25) \end{aligned}$$

We first work with term (i), as this is the term to which the spatial divergence theorem is applied. Taking the inner product and expanding this term out gives

$$\begin{aligned} & \left\langle \vec{\Omega} \cdot \nabla \left(\sum_{i=1}^I \sum_{p=1}^P \psi_{ip} \lambda_i(\vec{r}) \gamma_p(\vec{\Omega}) \right), \tau_2 \vec{a}^* \cdot \nabla_{\Omega} \Upsilon \right\rangle \\ & = \tau_2 \kappa B_z \sum_{i=1}^I \sum_{p=1}^P \psi_{ip} \left[\int_{\Omega^e} d\vec{\Omega} \gamma_p(\vec{\Omega}) \frac{\partial \gamma_q(\vec{\Omega})}{\partial \phi} \int_{V^e} dV \vec{\Omega} \cdot \nabla(\lambda_i(\vec{r})) \lambda_j(\vec{r}) \eta_1(\vec{r}, \vec{\Omega}) \chi(\vec{r}, \vec{\Omega}) \right. \\ & \left. + \int_{\Omega^e} d\vec{\Omega} \gamma_p(\vec{\Omega}) \sin^2 \theta \frac{\partial \gamma_q(\vec{\Omega})}{\partial \theta} \int_{V^e} dV \vec{\Omega} \cdot \nabla(\lambda_i(\vec{r})) \lambda_j(\vec{r}) \eta_2(\vec{r}, \vec{\Omega}) \chi(\vec{r}, \vec{\Omega}) \right]. \quad (4.26) \end{aligned}$$

Before proceeding, we define

$$\rho(\vec{r}, \vec{\Omega}) = \lambda_j(\vec{r}) \eta_1(\vec{r}, \vec{\Omega}) \chi(\vec{r}, \vec{\Omega}), \quad (4.27)$$

and consider only the spatial integrals from Equation 4.26. Applying the divergence theorem to the first spatial integral and substituting in Equation 4.27 gives

$$\begin{aligned} & \int_{V^e} dV \vec{\Omega} \cdot \nabla(\lambda_i(\vec{r})) \lambda_j(\vec{r}) \eta_1(\vec{r}, \vec{\Omega}) \chi(\vec{r}, \vec{\Omega}) \\ &= \int_{S^e} dS \lambda_i(\vec{r}) \rho(\vec{r}, \vec{\Omega}) \vec{\Omega} \cdot \hat{n} - \int_{V^e} dV \lambda_i(\vec{r}) \vec{\Omega} \cdot \nabla(\rho(\vec{r}, \vec{\Omega})). \end{aligned} \quad (4.28)$$

Taking the gradient of $\rho(\vec{r}, \vec{\Omega})$

$$\nabla(\rho(\vec{r}, \vec{\Omega})) = \nabla(\lambda_j(\vec{r})) \eta_1(\vec{r}, \vec{\Omega}) \chi(\vec{r}, \vec{\Omega}) + \lambda_j(\vec{r}) \nabla(\eta_1(\vec{r}, \vec{\Omega}) \chi(\vec{r}, \vec{\Omega})) \quad (4.29)$$

$$= \nabla(\lambda_j(\vec{r})) \eta_1(\vec{r}, \vec{\Omega}) \chi(\vec{r}, \vec{\Omega}) + \lambda_j(\vec{r}) \nabla(\eta_1(\vec{r}, \vec{\Omega})) \chi(\vec{r}, \vec{\Omega}) \quad (4.30)$$

$$+ \lambda_j(\vec{r}) \eta_1(\vec{r}, \vec{\Omega}) \nabla(\chi(\vec{r}, \vec{\Omega})), \quad (4.31)$$

where

$$\nabla(\eta_1(\vec{r}, \vec{\Omega})) = \sum_{i=1}^I \sum_{p=1}^P \psi_{ip} \nabla(\lambda_j(\vec{r})) \frac{\partial \gamma_p(\vec{\Omega})}{\partial \phi}, \quad (4.32)$$

and

$$\nabla(\chi(\vec{r}, \vec{\Omega})) = \frac{\eta_1^2(\vec{r}, \vec{\Omega}) + \eta_2^2(\vec{r}, \vec{\Omega}) \nabla(\eta_1(\vec{r}, \vec{\Omega})) - \nabla(\eta_1^2(\vec{r}, \vec{\Omega}) + \eta_2^2(\vec{r}, \vec{\Omega}) \eta_1(\vec{r}, \vec{\Omega}))}{(\eta_1^2(\vec{r}, \vec{\Omega}) + \eta_2^2(\vec{r}, \vec{\Omega}))^2}, \quad (4.33)$$

with

$$\nabla(\eta_1^2(\vec{r}, \vec{\Omega}) + \eta_2^2(\vec{r}, \vec{\Omega})) = 2\eta_1(\vec{r}, \vec{\Omega}) \nabla\eta_1(\vec{r}, \vec{\Omega}) + 2\eta_2(\vec{r}, \vec{\Omega}) \nabla\eta_2(\vec{r}, \vec{\Omega}). \quad (4.34)$$

The second spatial integral of Equation 4.26 can be solved similarly, giving a total of four terms; two surface integrals, and two volume. This allows for Upwinding to still be applied in space. Terms (ii) and (iii) can be expanded in a simpler manner, as the divergence theorem is not applied in these cases.

Beginning with term (ii):

$$\begin{aligned}
& \left\langle \kappa B_z \frac{\partial}{\partial \phi} \left(\sum_{i=1}^I \sum_{p=1}^P \psi_{ip} \lambda_i(\vec{r}) \gamma_p(\vec{\Omega}) \right), \tau_2 \vec{a}^* \cdot \nabla_{\Omega} \Upsilon \right\rangle \\
&= \tau_2 \kappa^2 B_z^2 \sum_{i=1}^I \sum_{p=1}^P \psi_{ip} \left[\int_{\Omega^e} d\vec{\Omega} \frac{\partial \gamma_p(\vec{\Omega})}{\partial \phi} \frac{\partial \gamma_q(\vec{\Omega})}{\partial \phi} \int_{V^e} dV \lambda_i(\vec{r}) \lambda_j(\vec{r}) \eta_1(\vec{r}, \vec{\Omega}) \chi(\vec{r}, \vec{\Omega}) \right. \\
&\quad \left. \int_{\Omega^e} d\vec{\Omega} \sin^2 \theta \frac{\partial \gamma_p(\vec{\Omega})}{\partial \theta} \frac{\partial \gamma_q(\vec{\Omega})}{\partial \theta} \int_{V^e} dV \lambda_i(\vec{r}) \lambda_j(\vec{r}) \eta_2(\vec{r}, \vec{\Omega}) \chi(\vec{r}, \vec{\Omega}) \right]. \quad (4.35)
\end{aligned}$$

Term (iii) is then given by

$$\begin{aligned}
& \left\langle \sigma_T(\vec{r}) \left(\sum_{i=1}^I \sum_{p=1}^P \psi_{ip} \lambda_i(\vec{r}) \gamma_p(\vec{\Omega}) \right), \tau_2 \vec{a}^* \cdot \nabla_{\Omega} \Upsilon \right\rangle \\
&= \tau_2 \kappa B_z \sum_{i=1}^I \sum_{p=1}^P \psi_{ip} \sigma_T(\vec{r}) \left[\int_{\Omega^e} d\vec{\Omega} \gamma_p(\vec{\Omega}) \frac{\partial \gamma_q(\vec{\Omega})}{\partial \phi} \int_{V^e} dV \lambda_i(\vec{r}) \lambda_j(\vec{r}) \eta_1(\vec{r}, \vec{\Omega}) \chi(\vec{r}, \vec{\Omega}) \right. \\
&\quad \left. \int_{\Omega^e} d\vec{\Omega} \sin^2 \theta \gamma_p(\vec{\Omega}) \frac{\partial \gamma_q(\vec{\Omega})}{\partial \theta} \int_{V^e} dV \lambda_i(\vec{r}) \lambda_j(\vec{r}) \eta_2(\vec{r}, \vec{\Omega}) \chi(\vec{r}, \vec{\Omega}) \right]. \quad (4.36)
\end{aligned}$$

Finally, to complete the derivation of the non-linear SUPG system, we consider term (VI) from equation 4.12 to give the right hand side term

$$\begin{aligned}
\langle Q, \tau_2 \vec{a}^* \cdot \nabla_{\Omega} \Upsilon \rangle &= \\
& \tau_2 \kappa B_z \left[\int_{\Omega^e} d\vec{\Omega} \frac{\partial q(\vec{\Omega})}{\partial \phi} \int_{V^e} dV Q(\vec{r}, \vec{\Omega}) \lambda_j(\vec{r}) \eta_1(\vec{r}, \vec{\Omega}) \right. \\
& \quad \left. + \int_{\Omega^e} d\vec{\Omega} \sin^2 \theta \frac{\partial q(\vec{\Omega})}{\partial \theta} \int_{V^e} dV Q(\vec{r}, \vec{\Omega}) \lambda_j(\vec{r}) \eta_2(\vec{r}, \vec{\Omega}) \right]. \quad (4.37)
\end{aligned}$$

4.3 Solving the Non-Linear System

Applying a non-linear SUPG method leads to a non-linear system of equations. For the linear SUPG method, as well as the standard DGFEM method, the

resulting system of the equations could be represented as a linear system, i.e.

$$A\vec{x} = \vec{b}, \quad (4.38)$$

where A is an $N \times N$ matrix, \vec{x} is a vector of unknowns of length N , and \vec{b} is a vector of known values of length N . The key to this type of system is that both A and \vec{b} are independent of the unknown \vec{x} , hence many solution methods are available, as linear systems have been studied extensively. When the weighting function is modified to include a term involving the solution gradient, the system can no longer be represented in the simple linear system given in Equation 4.38. The equation now takes the form

$$\vec{F}(\vec{x}) = \vec{b}, \quad (4.39)$$

where \vec{F} represents a vector of length N and each component depends on \vec{x} in a non-linear manner. Thus in this section we have derived an angular implementation of the non-linear SUPG method which effectively adds crosswind diffusion to the existing streamline diffusion term. It is expected that this additional term may improve the accuracy of the simulations, in particular for cases of low density media such as lung or air. As was seen in Chapter 3, the accuracy in low density media is negatively impacted by the amount of artificial diffusion required for stability. If the amount of streamline diffusion could be reduced with the introduction of cross-wind diffusion, the accuracy may improve.

Chapter 5

Conclusions and Future Work

A dose calculation method that is both accurate and fast is a crucial part of any radiation treatment system. Various approaches starting from the 1950's have been developed, using ever more sophisticated schemes, as both the underlying physics knowledge and computational capabilities progressed. For standard linac systems, existing dose calculation software has advanced to the point of being both accurate and fast enough for near real-time treatment planning. However, the development of new MR-guided linac systems has required that existing methods be modified to incorporate the effect of the magnetic field. As dose deposition occurs via secondary electrons, particles are affected by the Lorentz force that causes angular deflection. These effects can be modelled using Monte Carlo simulations, but St-Aubin et. al also derived a new angular advection term of the charged particle LBTE which accurately incorporates the magnetic field effects [24, 23].

Solving the modified LBTE numerically is challenging, as it contains both a spatial and an angular advection term. An existing method developed by St-Aubin et. al [24, 23], and Yang et. al [40] is capable of accurate solutions to the integro-PDE, however, the method features some potential inefficiencies. Firstly, because the stabilization method is predicated on a sequential solving

of both spatial and angular elements, the potential for parallelization is limited. Additionally, the work of Zelyak et. al [26] has shown that the convergence properties of the fixed-point iteration for the existing method are dependant on the magnetic field strength. This suggests that for certain configurations, the existing method could show very slow convergence, limiting the computational speed that can possibly be attained.

This thesis focuses on the development of an alternative angular stabilization scheme that has advantages both in terms of parallelization, and in terms of its convergence properties. The original method of Yang et. al [40] employs a DGFEM method in both space and angle. Using this method, elements are coupled together so that the solution in one element depends on the solution of the previous element, based on the advective direction. This requires a specific ordering for solution of the elements based on the respective spatial and angular advective velocities to ensure stability. In order to capture discontinuities in space due to the presence of tissue interfaces, the new method developed here still uses this DGFEM method in space. However, in angle, a continuous method is used where a small amount of angular diffusion is introduced in the streamline (advective) direction in order to stabilize the angular advection term, and allowing all angular elements to be solved simultaneously, as they are no longer coupled together. This introduces the potential for parallelization which could greatly improve computational speed.

The method developed here is called a Streamline Upwind Petrov-Galerkin, or SUPG method, and it is applied in angle only. The angular weighting function of the original FEM formulation is modified to include an additional term that serves to introduce artificial diffusion in an amount controlled by the parameter δ . An analysis of the convergence behaviour was first performed based on both the continuous and discrete formalisms. Fourier analysis of the discrete formalism suggested that neither the magnetic field strength nor

the SUPG parameter δ value should have any effect on the convergence rate of the source iteration scheme. This suggests that convergence should occur as quickly using the SUPG method as it would for the 0-magnetic field case. Inputting a variety of magnetic field strengths and values of δ into the discrete code confirmed these findings.

We hypothesized that the amount of artificial diffusion required for stability would depend on the energy, the magnetic field strength, and the material. These components impact the amount of advection present, and it was expected that increased advection would necessitate a larger value of δ . Existing code was modified to include the SUPG method so that dose could be calculated. Empirical investigation was consistent with this hypothesis, and it was found that in general, the δ value should be larger in higher energy groups and low density materials. Homogeneous phantoms were first used to determine the energy dependence. Typically, the SUPG method is applied for advection-diffusion systems, however in this case, no explicit diffusion is present, hence the scatter term serves to act as a diffusion term and thus we suspected that the total cross-section could be used as a surrogate for the diffusion coefficient. This idea was tested using a literature-defined form for δ , and it gave good agreement with the empirical behaviour that was observed.

Both homogeneous and heterogeneous slab phantoms were then used to evaluate the accuracy of the SUPG-method both in homogeneous material, and in the presence of inhomogeneities. Phantoms of pure lung, pure water, and pure bone were used, as well as both a water-bone-lung-water, and a water-bone-air-water phantom. The dose in each was calculated in both a 1.5 T perpendicular magnetic field and a 0.5 T parallel magnetic field, meant to simulate the main designs in use for linac-MR systems. For a 0.5 T parallel magnetic field, accuracy results were very good, with a 2%/2 mm gamma analysis achieving 100% agreement in all three homogeneous phantoms, as well as

the first heterogenous phantom. Results were not as good in the heterogenous phantom containing air, however for all other materials, the SUPG method was effective in the 0.5 T parallel magnetic field.

In the 1.5 T perpendicular magnetic field, high levels of accuracy were obtained in materials such as water and bone. However, lower density media such as lung and air suffered from a loss of accuracy, as compared to the existing validated DGFEM method. It was noted, however, that the SUPG method was indeed capable of capturing the effect of the magnetic field. We hypothesize that the problem in low-density media comes from the fact that advection dominates so strongly in these regions, requiring a large amount of artificial diffusion for stability, thus negatively impacting the accuracy. In terms of convergence, the SUPG method did perform consistently with the 0-magnetic field case, as expected. For certain configurations, such as the water-bone-air-water phantom in a 1.5 T perpendicular magnetic field, the number of iterations required for convergence was reduced by nearly half when compared to the existing DGFEM method.

With the eventual goal of improving accuracy in low density media, a non-linear SUPG method was derived in angle. The idea behind this technique is to introduce artificial diffusion in the cross-wind direction. While the implemented linear SUPG technique introduced diffusion to the streamline direction, i.e., in line with the magnetic field deflection, it is possible that instabilities were also present in the cross-wind direction perpendicular to the magnetic field deflection. Thus, the δ parameter was made large in order to stabilize the scheme. If diffusion could be explicitly controlled in the cross-wind direction, a reduction in δ may be possible, thus restoring some of the lost accuracy. This non-linear SUPG scheme was derived here for the LBTE with magnetic field term with the goal of implementing and testing the method.

In the future, we would like to implement the non-linear SUPG method and

observe if any improvement in accuracy can be obtained. To solve a system of equations of this type, typically an iterative technique is required. As such, implementing the non-linear scheme is not a simple extension of the existing linear scheme implementation, but rather requires a reworking of the problem architecture. For the linear scheme, many components of the iteration matrix could be pre-computed, as these did not change with the value of unknown angular fluence. In the case of the non-linear scheme, these same matrices must be recomputed for every iteration. This introduces challenges computationally that must be carefully considered in the implementation. Following implementation, a new stability study would be required as well as further accuracy testing. A nested iteration method such as that employed by Merton [51] is suggested for solution of the non-linear scheme, where an “outer” iteration is employed to converge the non-linear terms and an “inner” iteration such as Source Iteration used to converge the right-hand-side source terms. It is expected that this method should show improved accuracy over the existing linear scheme, in particular for low density media.

Bibliography

- [1] M. Karlsson, A. Ahnesjö, D. Georg, T. Nyholm, and J. Olofsson. *Independent Dose Calculations Concepts and Models*. ESTRO, 2010.
- [2] J.P. Gibbons, J.A. Antolak, D.S. Followill, M. Saiful Huq, E.E. Klein, K.L. Lam, J.R. Palta, D.M. Roback, M. Reid, and F.M. Khan. Monitor unit calculations for external photon and electron beams: Report of the AAPM Therapy Physics Committee Task Group No. 71. *Medical Physics*, pages 031501–1–34, 41(3) 2014.
- [3] F.M. Khan and J.P. Gibbons. *The Physics of Radiation Therapy*. Lippincott Williams and Wilkins, 2014.
- [4] A. Ahnesjö. Dose calculations for external photon beams in radiotherapy. *Phys. Med. Biol.*, pages R99–R155, 44 1999.
- [5] F.H. Attix. *Introduction to Radiological Physics and Radiation Dosimetry*. John Wiley and Sons, Inc., 1986.
- [6] W.F. Miller and E.E. Lewis. *Computational Methods of Neutron Transport*. The Johns Hopkins University Press, 1996.
- [7] L. Lu. Dose calculation algorithms in external beam photon radiation therapy. *Int. J. Cancer Ther. Oncol.*, 1 2013.

- [8] H.E. Johns and J.R. Cunningham. *The Physics of Radiology: Fourth Edition*. Charles C. Thomas, 1983.
- [9] O.N. Vassiliev, T.A. Wareing, J. McGhee, G. Failla, M.R. Salehpour, and F. Mourtada. Validation of a new grid-based Boltzmann equation solver for dose calculation in radiotherapy with photon beams. *Phys. Med. Biol.*, pages 581–98, 55 2010.
- [10] J.R. Cunningham. Scatter-air ratios. *Phys. Med. Biol.*, pages 42–51, 17 1972.
- [11] R.L. Stern, R. Heaton, M.W. Fraser, S.M. Goddu, T.H. Kirby, K.L. Lam, A. Molineu, and T.C. Zhu. Verification of monitor unit calculations for non-IMRT clinical radiotherapy: Report of AAPM Task Group 114. *Medical Physics*, pages 504–30, 38(1) 2011.
- [12] N. Papanikolaou, J.J. Battista, A.L. Boyer, C. Kappas, E. Klein, T.R. Mackie, M. Sharpe, and J. Van Dyk. Tissue inhomogeneity correction for megavoltage photon beams: Report of Task Group No. 65 of the Radiation Therapy Committee of the American Association of Physicists in Medicine. 2004.
- [13] H. F. Batho. Lung corrections in cobalt 60 beam therapy. *J. Can. Assoc. Radiol.*, pages 79–83, 15 1964.
- [14] M. E. Young and J. D. Gaylord. Experimental tests of corrections for tissue inhomogeneities in radiotherapy. *Br. J. Radiol.*, pages 349–55, 43(509) 1970.
- [15] M. R. Sontag and J. R. Cunningham. Clinical application of a CT based treatment planning system. *Comput. Tomogr.*, pages 117–30, 2 1978a.

- [16] M. R. Sontag and J. R. Cunningham. The equivalent tissue-air ratio method for making absorbed dose calculations in a heterogeneous medium. *Radiology*, pages 787–94, 129 1978.
- [17] T.R. Mackie, J.W. Scrimger, and J.J. Battista. A convolution method of calculating dose for 15-MV x rays. *Medical Physics*, pages 188–96, 12(2) 1984.
- [18] A. Ahnesjö, P. Andreo, and A. Brahme. Calculation and application of point spread functions for treatment planning with high energy photon beams. *Acta Oncol.*, pages 49–56, 26 1987.
- [19] J. Sievinen, W. Ulmer, and W. Kaissl. *AAA photon dose calculation model in Eclipse*. Varian Medical Systems, RAD #7170B, 2005.
- [20] C.M. Ma, J.S. Li, T. Pawlicki, S.B. Jiang, J. Deng, M.C. Lee, T. Koumrian, M. Luxton, and S. Brain. A Monte Carlo dose calculation tool for radiotherapy treatment planning. *Phys. Med. Biol.*, pages 1671–89, 47 2002.
- [21] M. Fippel. *Monte Carlo Techniques in Radiation Therapy*. Boca Raton, FL: CRC Press, pages 17–28, 2013.
- [22] K.A. Gifford, J.L. Horton, T.A. Wareing, G. Failla, and F. Mourtada. Comparison of a finite-element multigroup discrete-ordinates code with Monte Carlo for radiotherapy calculations. *Phys. Med. Biol.*, pages 2253–65, 51 2006.
- [23] J.St-Aubin, A. Keyvanloo, and B.G. Fallone. Discontinuous finite element space-angle treatment of the first order linear Boltzmann transport equation with magnetic fields: Application to MRI-guided radiotherapy. *Medical Physics*, pages 195–204, 43(1) 2016.

- [24] J.St-Aubin, A. Keyvanloo, O. Vassiliev, and B.G. Fallone. A deterministic solution of the first order linear Boltzmann transport equation in the presence of external magnetic fields. *Medical Physics*, pages 780–93, 42(2) 2015.
- [25] O.N. Vassiliev, T.A. Wareing, I.M. Davis, J. McGhee, D. Barnett, J.L. Horton, K. Gifford, G. Failla, U. Titt, and F. Mourtada. Feasibility of a Multigroup Deterministic Solution Method for 3D Radiotherapy Dose Calculations. *Int. J. Radiat. Oncol. Biol. Phys.*, pages 220–7, 72(1) 2008.
- [26] O. Zelyak, B.G. Fallone, and J. St-Aubin. Stability analysis of a deterministic dose calculation for MRI-guided radiotherapy. *Phys. Med. Biol.*, 63:015011, 2018.
- [27] T.A. Wareing, J.M. McGhee, J.E. Morel, and S.D. Pautz. Discontinuous finite element SN method on three-dimensional unstructured grids. *Nucl. Sci. Eng.*, pages 256–268, 138 2001.
- [28] G. Failla, T.A. Wareing, Y. Archambault, and S. Thompson. *Acuros XB Advanced Dose Calculations for the Eclipse Treatment Planning System*. Varian Medical Systems, Palo Alto, CA., 2010.
- [29] J. St-Aubin, S. Steciw, and B.G. Fallone. Effect of transverse magnetic field on a simulated in-line 6 MV linac. *Phys. Med. Biol.*, pages 4861–69, 55 2010.
- [30] J. St-Aubin, D. M. Santos, S. Steciw, and B.G. Fallone. Effect of longitudinal magnetic fields on a simulated in-line 6 MV linac. *Medical Physics*, pages 4916–23, 37(9) 2010.
- [31] B.G. Fallone, B. Murrar, S. Rathee, T. Stanescu, S. Vidakovic S. Steciw, E. Blosser, and D. Tymofichuk. First MR images obtained during mega-

- voltage photon irradiation from a prototype integrated linac-MR system. *Med. Phys.*, pages 2084–8, 36 2009.
- [32] P. Keall, M. Barton, and S. Crozier. The Australian Magnetic Resonance Imaging-Linac Program. *Seminars in Radiation Oncology*, 24(3):203–6, 2014.
- [33] J.F. Dempsey, D. Benoit, J.R. Fitzsimmons, A. Haghghat, J.G. Li, D.A. Low, S. Mutic, J.R. Palta, H.E. Romeijn, and G.E. Sjoden. A device for realtime 3D image-guided IMRT. *Int. J. Radiat. Biol.*, page S202, 63 2005.
- [34] D. Low, S. Mutic, S. Shvartsman, T. Chimielewski, G. Fought, A. Sharma, and J. Dempsey. TU-H-BRA-02: the physics of magnetic field isolation in a novel compact linear accelerator based MRI-guided radiation therapy system. *Med. Phys.*, page 3768, 43 2016.
- [35] B.W. Raaymakers, J.J. Lagendijk, J. Overweg, J.G. Kok, A.J. Raaijmakers, E.M. Kerkhof, R.W. van der Put, I. Meijnsing, S.P. Crijs, F. Benedosso, M. van Vulpen, C.H. de Graaff, J. Allen, and K.J. Brown. Integrating a 1.5 T MRI scanner with a 6 MV accelerator: proof of concept. *Phys. Med. Biol.*, pages N229–37, 54 2009.
- [36] A. Keyvanloo, B. Burke, B. Warkentin, T. Tadic, S. Rathee, C. Kirkby, D.M. Santos, and B.G. Fallone. Skin dose in longitudinal and transverse linac-MRIs using Monte Carlo and realistic 3D MRI field models. *Med. Phys.*, pages 6509–21, 39(10) 2012.
- [37] C. Kirkby, B. Murray, S. Rathee, and B.G. Fallone. Lung dosimetry in a Linac-MRI radiotherapy unit with a longitudinal magnetic field. *Med. Phys.*, pages 4722–32, 37 2010.

- [38] C. Kirkby, T. Stanescu, S. Rathee, and B.G. Fallone. Patient dosimetry for hybrid MRI-radiotherapy systems. *Med. Phys.*, pages 1019–27, 35 2008.
- [39] T.P. Fries and H.G. Matthies. *A Review of Petrov-Galerkin Stabilization Approaches and an Extension to Meshfree Methods*. Braunschweig, Institut für Wissenschaftliches Rechnen, 2004.
- [40] R. Yang, O. Zelyak, B.G. Fallone, and J.St-Aubin. A novel upwind stabilized discontinuous finite element angular framework for deterministic dose calculations in magnetic fields. *Phys. Med. Biol.*, 63 2018.
- [41] K. Bush, I.M. Gagne, S. Zavgorodni, W. Ansbacher, and W. Beckham. Dosimetric validation of Acuros XB with Monte Carlo methods for photon dose calculations. *Med. Phys.*, pages 2208–21, 38 2011.
- [42] O. Zelyak. *Stability Analysis of a Deterministic Dose Calculation for MRI-Guided Radiotherapy*. Master’s thesis, University of Alberta, Edmonton, Alberta, 2017.
- [43] J.E. Morel. Multigroup Legendre coefficients for the diamond difference continuous slowing down operator. *Nuc Sci Eng*, 91:324–31, 1985.
- [44] J.M. Jin. *The Finite Element Method in Electromagnetics*. Wiley-EEE, 3rd edition., 2014.
- [45] E. Isaacson and H.B. Keller. *Analysis of Numerical Methods*. John Wiley and Sons, Inc., 1966.
- [46] G.H. Golub and C.F. Van Loan. *Matrix Computations - Third Edition*. American Nuclear Society, Inc., 1993.
- [47] E.W. Larsen and J.E. Morel. *Advances in discrete-ordinates methodology, Nuclear Computational Science*. Berlin:Springer, 2010.

- [48] G. Kanschat. A Robust Finite Element Discretization for Radiative Transfer Problems with Scattering. *East-West J. Numer. Math*, 6:265–272, 1998.
- [49] A.N. Brooks and T.J.R. Hughes. Streamline Upwind/ Petrov-Galerkin Formulations for Convection Dominated Flows with Particular Emphasis on the incompressible Navier-Stokes Equations. *Comp. Methods in Appl. Mech. and Engineering*, pages 199–259, 32 1982.
- [50] L.J. Jr. Lorence, J.E. Morel, G.D. Valdez, NM Los Alamos National Lab., and Albuquerque NM Applied Methods, Inc. Physics guide to CEPXS: A multigroup coupled electron-photon cross-section generating code. 1989.
- [51] S.R. Merton. *Discontinuous Galerkin Methods for Computational Radiation Transport*. PhD thesis, Imperial College London, 2012.
- [52] C.C. Pain, M.D. Eaton, R.P. Smedley-Stevenson, A.J.H. Goddard, M.D. Piggot, and C.R.E. de Oliveira. Streamline upwind Petrov-Galerkin methods for the steady-state Boltzmann transport equation. *Comp. Methods in Appl. Mech. and Engineering*, pages 4448–72, 195 2006.
- [53] T.J.R. Hughes, M. Mallet, and A. Mizukami. A new finite element formulation for computational fluid dynamics: II. beyond SUPG. *Comp. Methods in Appl. Mech. and Engineering*, pages 341–355, 54 1986.